



**POLITECNICO DI MILANO**  
DEPARTMENT OF MECHANICS  
DOCTORAL PROGRAM IN MECHANICAL ENGINEERING

---

**DESIGN AND CHARACTERIZATION OF A NEW QUICK-STOP  
DEVICE FOR MICROMACHINING**

Doctoral Dissertation of:  
**Lara Rebaioli**  
**738817**

Supervisor:  
**Prof. Quirico Semeraro**

Tutor:  
**Prof. Roberto Viganò**

The Chair of the Doctoral Program:  
**Prof. Gianpiero Mastinu**

2011 – XXIV Cycle



## Abstract

Mechanical micromachining is one of the most flexible and widely exploited processes in the microscale but it still needs a knowledge improvement in its fundamentals: the cutting process, in fact, cannot be described by means of the same models used for the macroscale since several typical phenomena take place when performing chip removal with small uncut chip thickness. The so-called quick-stop experiments are a very useful instrument to study the tool-material interaction because they allow to freeze the chip formation in its steady condition by abruptly stop the cutting action. A new quick-stop device (QSD) has been designed in the present study to be successfully used within the typical microscale cutting requirements. The proposed device has been fully characterized in terms of performance by means of *ad hoc* sensors in order to know conditions defining each quick-stop experiment.

**Keywords:** quick-stop device, micromachining, chip formation, orthogonal cutting



# Table of contents

<b>Introduction</b>	1
<b>1 Literature review</b>	3
1.1 Micromachining typical phenomena	3
1.1.1 Size effect	5
1.1.2 Minimum chip thickness effect	6
1.1.3 Consequence of material defects presence	8
1.1.4 Influence of material microstructure	8
1.1.5 Stable built-up edge	10
1.1.6 Cutting forces variability	11
1.2 Quick Stop Devices	11
1.2.1 QSDs classification	12
1.2.2 QSDs performance	15
1.2.3 QSDs details	18
1.3 Objectives	55
<b>2 Equipment</b>	57
2.1 Machining centre	57
2.2 Force measurement system	60
2.2.1 Triaxial load cell	60
2.2.2 Data acquisition device	61
2.3 Data acquisition device used in the QSD controlling and synchronizing system	63
2.4 Oscilloscope	63
<b>3 Micro QSD design</b>	65
3.1 Micro QSD requirements	65
3.2 Micro QSD layout	68
3.2.1 Tool holder block	70
3.2.2 Percussion system	73
3.2.3 Controlling and synchronizing system	78
<b>4 Micro QSD performance characterization</b>	81
4.1 Performance characterization	83
4.2 First performance characterization method	83

4.2.1	Results .....	85
4.3	Second performance characterization method .....	86
4.3.1	Impact speed sensor .....	86
4.3.2	Results .....	88
4.4	Third performance characterization method .....	90
4.4.1	Angular position sensor .....	90
4.4.2	Data analysis .....	97
4.4.3	Results .....	100
<b>5</b>	<b>Preliminary tests .....</b>	<b>105</b>
5.1	C10 steel .....	105
5.2	Tool .....	106
5.3	Test results .....	108
	<b>Conclusions and future developments .....</b>	<b>115</b>
<b>A</b>	<b>Program for evaluating the expected striker speed at the impact</b> <b><math>V_{imp}</math> basing on the air pressure inside the cylinder <math>P_{air}</math> .....</b>	<b>117</b>
<b>B</b>	<b>Program for acquiring cutting forces .....</b>	<b>123</b>
<b>C</b>	<b>Program for managing quick stop experiments .....</b>	<b>125</b>
<b>D</b>	<b>Electronic circuit schematics of the angular position sensors .....</b>	<b>131</b>
<b>E</b>	<b>Program for analyzing signals acquired by angular position</b> <b>sensors .....</b>	<b>133</b>
<b>F</b>	<b>Results of performance measurement campaigns .....</b>	<b>139</b>
	<b>References .....</b>	<b>167</b>

## List of figures

1.1	Comparison of machining processes [2] .....	3
1.2	Micromachining capability over time [2]. .....	4
1.3	Difference between a) macro and b) micro machining [6] .....	5
1.4	Equivalent chip sliding plane and rake angle [9] .....	6
1.5	Variation of specific cutting energy with undeformed chip thickness [3] .....	6
1.6	Theoretical surface profile, assuming that the minimum cutting thickness determines the achievable surface roughness [5] .....	7
1.7	Ratio of measured chip volume to nominal chip volume [15] .....	7
1.8	Bending of the tool during the multiple non-cutting tool passes preceding the formation of a chip [15] .....	8
1.9	Endmilling of multiphase ductile iron [18] .....	9
1.10	Experimental forces and corresponding spectra for tests on a) single-phase ferrite and b) multiphase ductile iron [18] .....	9
1.11	Experimental and predicted roughness for tests on a) single-phase pearlite and b) multiphase ductile iron [19] .....	10
1.12	Material flow near a rounded cutting edge [3], b) from [23] .....	11
1.13	Classification of existing QSDs (in red the solutions chosen for the micro QSD developed in the present study) .....	14
1.14	Scheme of a quick-stop experiment with the micro QSD developed in this study (adapted from [30]) .....	15
1.15	Scheme of the QSD developed by Kececioglu [25] .....	18
1.16	QSD developed by Chern [45] a) before and b) after triggering .....	19
1.17	Exploded model of the QSD developed by Chern [45] .....	19
1.18	Chip micrographs 200 x ; a) $V_c = 24.3$ m/min, $f = 0.101$ mm/rev, $\gamma = 20^\circ$ ; b) $V_c = 45.6$ m/min, $f = 0.101$ mm/rev, $\gamma = 10^\circ$ ; c) $V_c = 45.6$ m/min, $f = 0.191$ mm/rev, $\gamma = 5^\circ$ [45] .....	20
1.19	a) Scheme and b) picture of the QSD developed by Zeb et al. [50] .....	21
1.20	Scheme and picture of the QSD developed by Ponkshe [28] and used by Joshi et al. [44], Subbiah et al. [47-48] .....	22
1.21	Scheme of the "Aachen 1" QSD described in [29] .....	22
1.22	Scheme of the "Berlino" QSD described in [29] (in brackets standard symbols) .....	23
1.23	Scheme of the QSD developed by Black et al. a) face plate and b) tool pivoting device [39] .....	25

1.24	Scheme of the QSD developed by Yeo et al. [42]	26
1.25	QSD developed by Hastings [27]	27
1.26	Scheme of the QSD developed by Hastings [27]	27
1.27	QSD developed by Stevenson et al. [32]	28
1.28	Scheme of the QSD developed by Philip [33]	28
1.29	QSD developed by Philip [33]	29
1.30	Exploded view of the QSD developed by Brown et al. [35]	30
1.31	Construction for $t_s$ [35]	31
1.32	Scheme of the “Delft 3” QSD described in [29]	32
1.33	Scheme of the “Göteborg” QSD described in [29]	32
1.34	QSD developed by Ellis et al. [30]	33
1.35	Scheme of the tool-workpiece separation process [30]	34
1.36	Construction for $t_s$ and $d_s$ [30]	34
1.37	Scheme of the QSD developed by Williams et al. [31]	35
1.38	Scheme of the QSD developed by Brown [38]	36
1.39	Scheme of the QSD developed by Lin et al. [43]	37
1.40	Scheme of the “Aachen 2” QSD described in [29]	38
1.41	Scheme of the “Aachen 3” QSD described in [29]	38
1.42	a) Scheme and b) picture of the QSD developed by Giusti [41]	39
1.43	Scheme of the “Delft 1” QSD described in [29]	40
1.44	Scheme of the “Pisa 1” QSD described in [29]	41
1.45	Scheme of the “Pisa 2” QSD described in [29]	41
1.46	Working principle of the QSD developed by Wu et al. [46]	42
1.47	Scheme of the QSD developed by Wu et al. [46]	43
1.48	Scheme of the QSD developed by Hsu [26]	44
1.49	Oscillogram of cutting force acquired during a quick-stop test [26]	45
1.50	Scheme of the QSD developed by Vorm [37]	45
1.51	Separation time for different shear pin notch diameters [37]	46
1.52	Separation time for different cutting speeds [37]	47
2.1	Overview of KERN Evo machining centre	58
2.2	Laser presetting system during the measurement of a mill	59
2.3	Touch probe system during the measurement of the upper surface of a workpiece	60
2.4	Triaxial load cell	61
2.5	Load cell control unit	61
2.6	PC embedded data acquisition device	62
2.7	I/O connector block	62
2.8	USB data acquisition device	63
2.9	Digital oscilloscope	64



3.1	Orthogonal cutting .....	65
3.2	Tube orthogonal cutting [47] .....	66
3.3	Orthogonal cutting operation on the machining centre .....	66
3.4	Disc orthogonal cutting .....	67
3.5	Glass shear pins .....	68
3.6	Scheme of the micro QSD layout .....	69
3.7	Overview of the micro QSD placed in the Kern EVO machining centre [A = tool holder block, B = percussion system] .....	69
3.8	a) First and b) second version of the tool holder block [C = rotating part, D = stationary part] .....	70
3.9	Exploded model of the tool holder block .....	71
3.10	Separation angle for different positions of the tool cutting edge .....	72
3.11	Kinematics of the tool holder rotating part .....	72
3.12	Percussion system [E = striker, F = trigger, G = solenoid, H = cylinder] .....	73
3.13	Model of the percussion system .....	74
3.14	Section of percussion system with the piston in its a) initial and b) final position .....	75
3.15	Piston stroke discretization .....	75
3.16	Expected piston speed for different values of cylinder diameter ( $P_{\text{air}} = 1 \text{ MPa}$ , $V_0 = 19.6 \cdot 10^{-5} \text{ m}^3$ ) .....	76
3.17	Expected piston speed for different values of cylinder back chamber volume ( $P_{\text{air}} = 1 \text{ MPa}$ , $\phi = 50 \text{ mm}$ ) .....	76
3.18	Back chamber section .....	77
3.19	Expected piston speed for variable and constant $P_{\text{air}}$ ( $P_{\text{air}} = 0.5 \text{ MPa}$ , $\phi = 50 \text{ mm}$ , $V_0 = 19.6 \cdot 10^{-5} \text{ m}^3$ ) .....	77
3.20	QSD controlling and synchronizing system .....	79
3.21	Electronic circuit .....	79
4.1	Scheme of a quick-stop experiment (adapted from [30]) and layout of the micro QSD .....	82
4.2	Scheme of the first performance characterization method .....	83
4.3	Scheme of the tool holder rotating part (front view) .....	83
4.4	Scheme of the impact model .....	84
4.5	Expected striker speed at the impact $V_{\text{imp}}$ (dashed blue = design $P_{\text{air}}$ value) .....	85
4.6	Scheme of the second performance characterization method .....	86
4.7	$V_{\text{imp}}$ measuring sensor for the a) first and b) second version of the tool holder block .....	87
4.8	Scheme of the $V_{\text{imp}}$ measuring sensor .....	87

4.9	Results of $V_{imp}$ measured (blue) and expected striker speed at the impact $V_{imp}$ .....	88
4.10	Results of the $V_{imp}$ measurements .....	89
4.11	Scheme of the third performance characterization method .....	90
4.12	Sequence acquired by means of the high speed camera .....	91
4.13	Laser triangulation sensor [A = reflecting surface, B = emitting diode, C = receiving diodes] .....	91
4.14	Scheme of the laser triangulation sensor .....	92
4.15	Angular position sensor based on polarizing filters [D = diodes holder, E = polarizing filter disc] during calibration .....	92
4.16	Scheme of the angular position sensor based on polarizing filters .....	93
4.17	Signals acquired during a calibration test of the laser triangulation sensor .....	94
4.18	Result of dividing the difference of the Fig. 4.17 signals by their sum (laser triangulation sensor) .....	94
4.19	Result of linear regression on the selected points (laser triangulation sensor) .....	95
4.20	Signals acquired during a calibration test of the angular position sensor based on polarizing filters .....	96
4.21	Result of linear regression on the selected points (polarized filter sensor) .....	97
4.22	Original data (red) and moving average result (black) [tool holder motion law acquired by means of the laser triangulation sensor in a non-cutting test at $P_{air} = 0.1$ MPa] .....	98
4.23	Horizontal tool speed (black), cutting speed (dashed red), tool-workpiece separation beginning (dotted green) and end (dot-dashed green), tool exit from the uncut chip thickness (solid green), expected horizontal tool speed (long-dashed blue) .....	99
4.24	Horizontal tool speed (black), cutting speed (dashed red), tool-workpiece separation beginning (dotted green) and end (dot-dashed green), tool exit from the uncut chip thickness (solid green), distance covered by the tool (orange) .....	99
4.25	a) First and b) second type of tool holder behaviour [horizontal tool speed (black), cutting speed (dashed red), tool-workpiece separation beginning (dotted green) and end (dot-dashed green)] ..	100
4.26	Micro QSD performance in campaigns with $P_{air} = 0.2$ MPa .....	102
4.27	Micro QSD performance in campaigns with $P_{air} = 0.3$ MPa .....	103
5.1	C10 microstructure: a) longitudinal and b) cross section .....	105
5.2	Turning tool model .....	106

---

5.3	Quick stop tests results with $V_c = 50$ m/min .....	109
5.4	Quick stop tests results with $V_c = 75$ m/min .....	110
5.5	Quick stop tests results with $V_c = 100$ m/min .....	110
5.6	Example of cutting force measurements during a quick stop tests with $V_c = 50$ m/min .....	111
5.7	Example of cutting force measurements during a quick stop tests with $V_c = 75$ m/min .....	112
5.8	Example of cutting force measurements during a quick stop tests with $V_c = 100$ m/min .....	112
A.1	Piston stroke discretization .....	117
A.2	Results of $V_{imp}$ measurement (blue) and expected striker speed at the impact $V_{imp}$ .....	121
C.1	Program graphical interface .....	125
C.2	Electronic circuit schematics .....	130
D.1	Schematics of the amplifier circuit of the laser triangulation sensor .....	131
D.2	Schematics of the amplifier circuit of the polarizing filters sensor .....	132
E.1	Original data (red) and moving average result (black) .....	134
E.2	Horizontal tool speed (black), cutting speed (dashed red), tool-workpiece separation beginning (dotted green) and end (dot-dashed green), tool exit from the uncut chip thickness (solid green), expected horizontal tool speed (long-dashed blue) .....	136



## List of tables

1.1	Use of parameters for QSDs performance evaluation .....	17
1.2	Performance of the QSD developed by Philip with a non-preloaded shear pin [33] .....	29
1.3	Performance of the QSD developed by Philip with a preloaded shear pin [33] .....	30
1.4	Summary of QSDs performance evaluation .....	48
2.1	KERN Evo specifications, relating to X, Y and Z axes .....	58
2.2	KERN Evo specifications, relating to B and C axes .....	59
3.1	Percussion system specifications .....	78
4.1	Micro QSD performance in campaigns with $P_{\text{air}} = 0.2$ MPa .....	102
4.2	Micro QSD performance in campaigns with $P_{\text{air}} = 0.3$ MPa .....	103
5.1	Tool specifications .....	106
5.2	Analyzed tools (for 1-3 see [74-75]) .....	107
5.3	Angle measurement results .....	108
F.1	Acquisitions made by the laser triangulation sensor during the campaign with $P_{\text{air}} = 0.2$ MPa and their analysis .....	140
F.2	Acquisitions made by the laser triangulation sensor during the campaign with $P_{\text{air}} = 0.3$ MPa and their analysis .....	148
F.3	Acquisitions made by the sensor based on polarizing filters during the campaign with $P_{\text{air}} = 0.2$ MPa and their analysis .....	153
F.4	Acquisitions made by the sensor based on polarizing filters during the campaign with $P_{\text{air}} = 0.3$ MPa and their analysis .....	161



## List of symbols

$d$	Horizontal distance of the tool cutting edge from the tool holder hinge
$d_s$	Separation distance
$D$	Distance between the couples of facing photodiodes
$f$	Feed
$F_c$	Cutting force
$I_2$	Moment of inertia of the tool holder comprising the tool
$L$	Vertical distance of the tool cutting edge from the tool holder hinge
$m_1$	Concentrated mass of the striker
$P$	Positioning tolerance
$P_{\text{air}}$	Air pressure into the cylinder
$P_s$	Positioning scatter
$r$	Radial distance of the impact area from the tool holder hinge
$R$	Radial distance of the tool cutting edge from the tool holder hinge
$t_c$	Uncut chip thickness
$t_s$	Separation time
$V_0$	Back chamber initial volume
$V_c$	Cutting speed
$V_{\text{imp}}$	Striker speed at the impact with the tool holder
$V_t$	Tangential tool speed
$V_{t,0}$	Horizontal component of the tool speed if the tool cutting edge is vertically aligned with the tool holder hinge
$V_{t,x}$	Horizontal component of the tool speed
$V_w$	Workpiece speed
$X_0$	Back chamber initial length
$\alpha$	Angular offset between the tool cutting edge and the vertical line passing from the tool holder hinge
$\theta$	Angular position
$\phi$	Cylinder diameter
$\omega$	Angular speed
$\dot{\omega}$	Angular acceleration





## Introduction

Among the available micromachining processes, chip removal is well appreciated for its versatility in terms of workpiece material and geometry, which has led it to be widely used to produce parts for several industrial fields (mechanics, fluidics, electronics, optics, biotechnology, etc...).

However, basic research is still needed to investigate the tool-material interaction and the chip formation at the microscale since several typical phenomena (e.g. the “minimum chip thickness effect”, the “size effect”, etc...) take place when performing chip removal with small uncut chip thickness and the process cannot be effectively described simply downscaling macroscale models.

The best way to carry out this kind of study is to exploit the so-called “frozen cut” experiments, which allow to “freeze” the chip formation in its steady condition by abruptly stop the cutting action. Hence, the main aim of the present work is to design a new quick-stop device (QSD) to carry out those experiments within the typical microscale cutting requirements (i.e. cutting speed lower than 200 m/min and chip thickness between less than 1  $\mu\text{m}$  and 100  $\mu\text{m}$ ).

The developed device has to be characterized in terms of performance in order to validate each quick-stop test by means of proper indexes; therefore, *ad hoc* sensors have been designed in the present study to be used for online performance measurements.

In addition, some preliminary quick-stop tests have been performed to prove the micro QSD effectiveness and repeatability.

Chapter **1** presents the literature survey which has allowed to define the thesis objective. In Section 1.1, the typical phenomena taking place when machining in the microscale are analyzed. In Section 1.2, all the existing QSDs are classified and critically discussed in terms of working principle and performance characterization; this leads to define the best layout for the new QSD to design and to identify the performance indexes to consider. Finally, in Section 1.3 the study aim is outlined.

Chapter **2** describes all the equipment used in the present study.

Chapter **3** deals with the micro QSD layout, showing in detail its main components and discussing their design.

Chapter **4** deeply analyzes different procedures for the performance characterization of the quick-stop device; here the developed sensors are presented and the characterization results are shown and discussed.

Chapter **5** shows the results of the preliminary quick-stop experiments which proved the micro QSD to be effective in studying the chip formation in the microscale. This tests also point out how the device is very promising for investigating the effect of several cutting parameters on the cutting process output.

# Chapter 1

## Literature survey

Mechanical micromachining is by now a widespread process but several typical phenomena take place when performing chip removal with small uncut chip thickness, hence in this field the cutting process cannot be described by means of the same models used for the macroscale. It is then necessary to study again the chip formation and for this reason a quick-stop device, suitable for micromachining, should be developed. The new device should be fully characterized in terms of performance in order to know conditions under which every quick-stop experiment has been carried out.

### 1.1 Micromachining typical phenomena

The continuous size reduction of components in different industrial fields (such as mechanics, fluidics, electronics, optics, biotechnology, etc...) has driven the development of several machining techniques (summarized in Fig. 1.1) able to produce workpieces and/or features in the microscale [1-2].

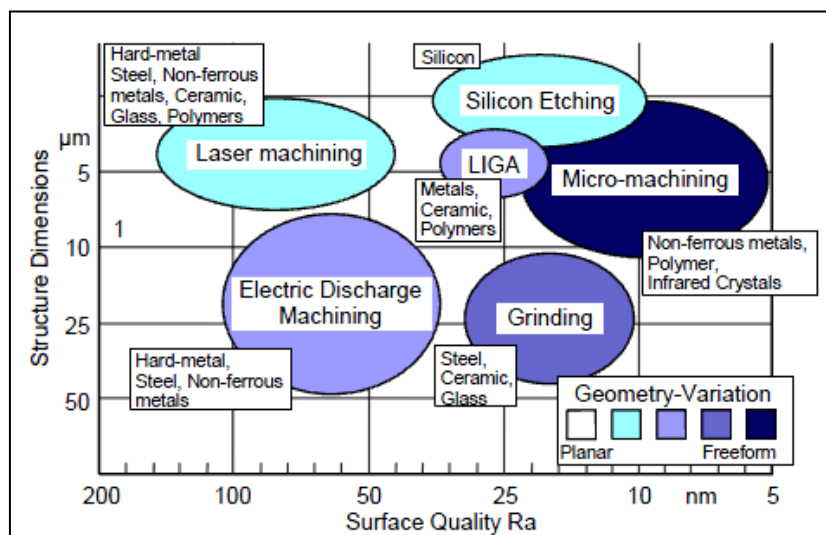


Fig. 1.1: Comparison of machining processes [2].

Among the different processes, chip removal (whose evolution is represented in Fig. 1.2) is widely used thanks to its flexibility in terms of workpiece material and geometry but it is still not completely understood and controlled; in fact the cutting process cannot be effectively described simply downscaling models already developed for the macroscale since several preventing phenomena take place during chip formation [3-4].

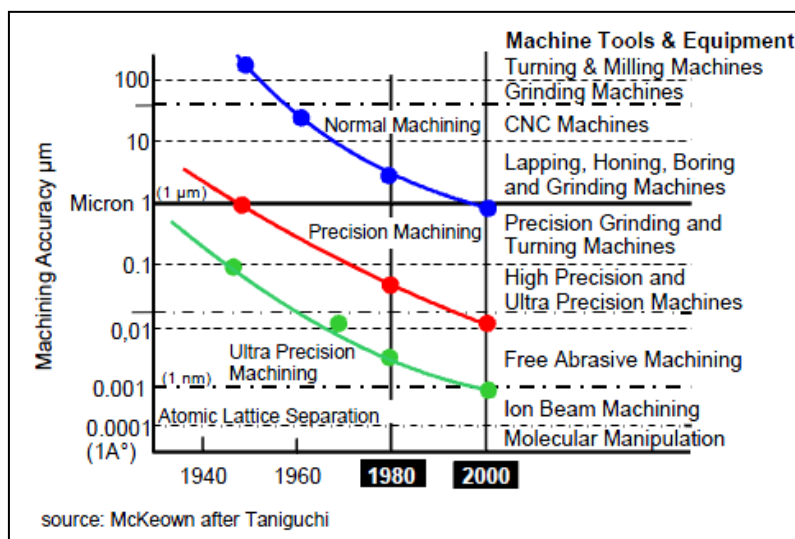


Fig. 1.2: Micromachining capability over time [2].

The typical phenomena taking place during mechanical micromachining are:

- the so-called “size effect”: if critical tool geometrical features, as the edge radius, tend to be comparable in size to the uncut thickness [5], the tool “effective rake angle” becomes highly negative; this makes ploughing the major cutting mechanism (instead of shearing) [6-8] and therefore the specific cutting energy becomes higher [9-12];
- the so-called “minimum chip thickness effect”: due to elastic recovery of the material, only uncut chip thickness higher than a minimum limit can be removed from the workpiece; this phenomenon often makes the cutting operation intermittent and affects the surface roughness [5, 11-16];
- the smaller the uncut chip thickness is, the higher the material resistance because the probability to have stress-reducing microstructural defects inside the chip thickness decreases [17];
- when machining in the microscale, materials cannot be considered homogeneous since the tool geometrical features and the uncut chip thickness have the same magnitude order of the material grains and this makes the cutting forces variable with grain orientation [3, 18-20];

- a stable built-up edge, called “dead metal cap”, is claimed to be present when machining in the microscale [3-4, 21-23];
- a wide variability of cutting forces is due to current tool tolerances, which are not sufficient to work in the microscale with the required performance stability [24].

Basic research is still needed to investigate the tool-material interaction and the chip formation at the microscale. The so-called quick-stop experiments allow to carry out this kind of studies since they are able to freeze the chip formation in a steady condition by abruptly interrupting the cutting action; the aim of the present study is to discuss a quick-stop device (QSD) designed for the orthogonal microcutting condition.

### 1.1.1 Size effect

As highlighted, for example, by Weule et al. [5], roundness of the tool cutting edge is more significant in micromachining because, as the tool size decreases, its sharpness cannot be improved more than a certain limit not to excessively affect the tool strength and because of limitations in the tool fabrication processes.

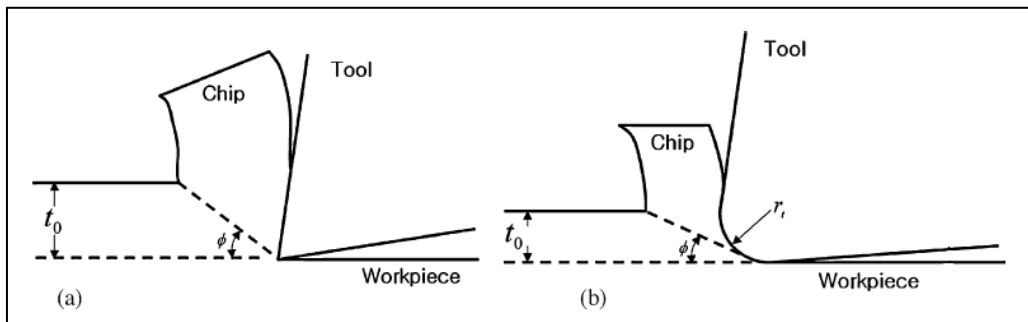


Fig. 1.3: Difference between a) macro and b) micro machining [6].

When the edge radius is comparable in size to the uncut chip thickness, the tool effective rake angle ( $\alpha_t$  in Fig. 1.4) becomes highly negative and this fact determines an increasing of the tool ploughing action, to which an elastic-plastic deformation of the workpiece is associated [9-10].

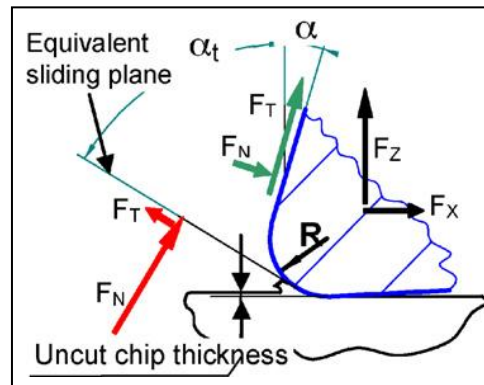


Fig. 1.4: Equivalent chip sliding plane and rake angle [9].

As shown by [3-4], several experimental works [7-8] have determined that the shearing process could not account for all of the required specific cutting energy (Fig. 1.5) when machining at values of uncut chip thickness of the same magnitude order of the tool cutting edge radius; they also showed that ploughing and elastic recovery of the workpiece along the flank face of the tool play a significant role.

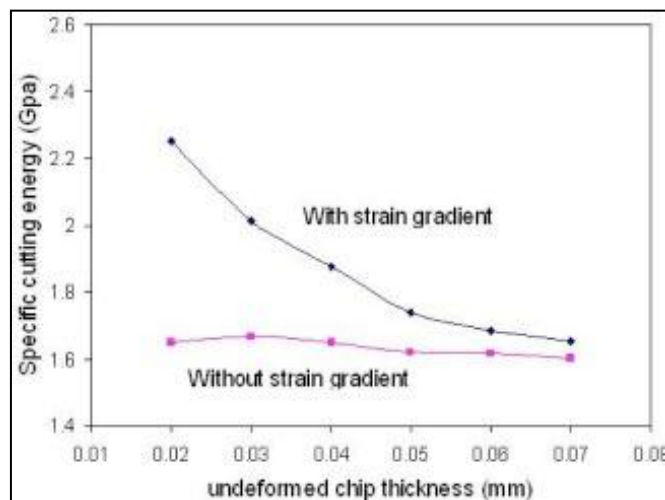


Fig. 1.5: Variation of specific cutting energy with undeformed chip thickness [3].

### 1.1.2 “Minimum chip thickness” effect

Ikawa et al. [13-14] defined the minimum chip thickness as “the minimum undeformed thickness of the chip removed from a work surface at a cutting edge under perfect performance of the metal-cutting system”.

Weule et al. [5] have been the first to point out the existence of the minimum chip thickness; they also stated that minimum chip thickness influences the achievable surface roughness in microendmilling, since they hypothesized that it is responsible for the observed sawtoothlike surface profile.

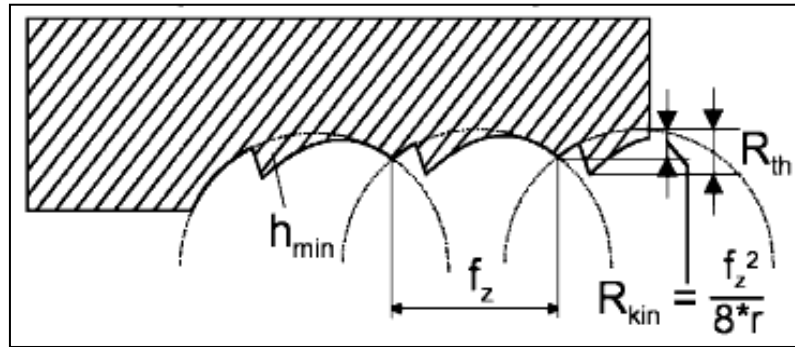


Fig. 1.6: Theoretical surface profile, assuming that the minimum cutting thickness determines the achievable surface roughness [5].

Weule et al. also stated that the minimum chip thickness depends on the cutting edge sharpness and on machined material properties. Several other studies have been carried out regarding the minimum chip thickness; among these, the ones by Kim et al. [15-16] proved the existence of the minimum chip thickness in micromilling.

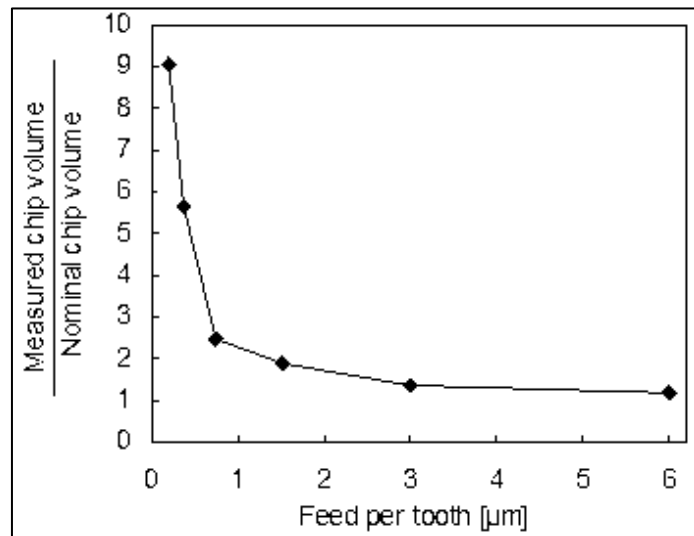


Fig. 1.7: Ratio of measured chip volume to nominal chip volume [15].

The authors estimated the chip volume obtained for different feedrates (basing on SEM images of the collected chips) and compared it with the nominal chip volume; they found that for very small feedrates, corresponding to a small uncut chip thickness, the measured chip volume was much higher than the nominal one, showing that chip did not form at each cutting edge pass.

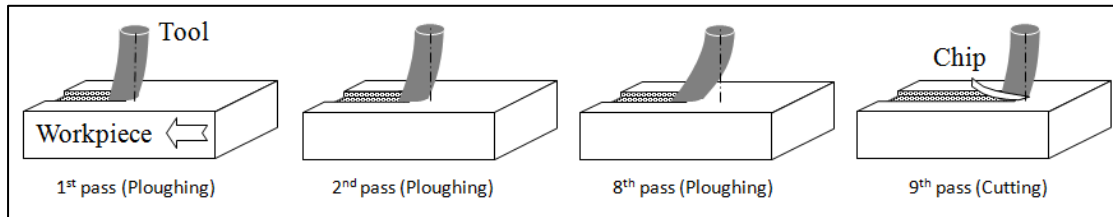


Fig. 1.8: Bending of the tool during the multiple non-cutting tool passes preceding the formation of a chip [15]

According to Kim et al. this fact means that the minimum chip thickness effect in combination with the low stiffness of the mill causes an intermittent chip production, which is confirmed by the distance between machining marks on the workpiece surface.

### 1.1.3 Consequence of material defects presence

Jackson's contribution in Davim's book [17] underlines another cause of material resistance increasing in micromachining: all metals contain defects and discontinuities (such as grain boundaries, dislocations, missing atoms, impurity, etc...) and when the uncut chip thickness is small, the probability to have stress-reducing microstructural defects inside it decreases, thus the energy required for chip removal increases.

Jackson also outlines that, since the shear stress and strain are unusually high, discontinuous microcracks tend to form on the primary shear plane; they continuously weld and reform while the strain increases, this way they work together with dislocations in generating slip on the shear plain.

### 1.1.4 Influence of material microstructure

The crystalline grain size of most commonly used engineering materials (such as steel, aluminum, etc ...) is comparable in size to the typical tool geometrical features and the uncut chip thickness used in micromachining ; this means that material microstructure influences the cutting process at this scale.



[3] reminds that the effect of the crystallographic orientation on the mechanism of chip formation, on surface generation and on cutting forces variation have been widely studied. For example, Vogler et al. [18] carried out endmilling tests with a 500  $\mu\text{m}$  diameter mill on both single-phase ferrite and pearlite and multiphase ductile iron.

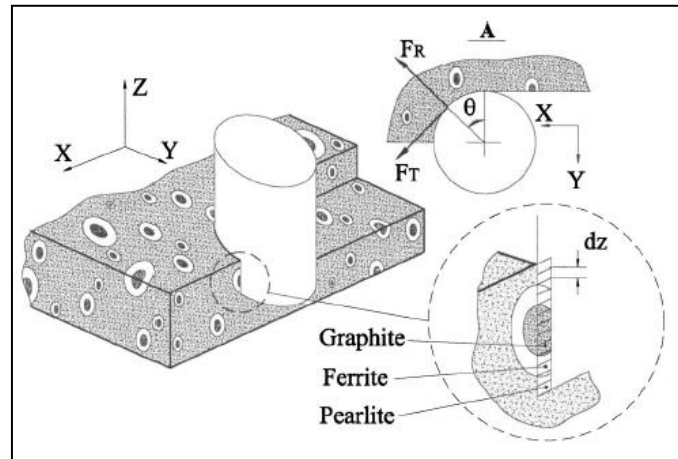


Fig. 1.9: Endmilling of multiphase ductile iron [18].

They found out that the cutting force spectra for machining ferrite and pearlite (Fig. 1.10 a) do not show energy at frequencies above 10 kHz while high-frequency components are present in spectra related to multiphase ductile iron (Fig. 1.10 b); this is an evidence that the high-frequency components are due to the multiphase microstructure and proves cutting forces are influenced by material microstructure.

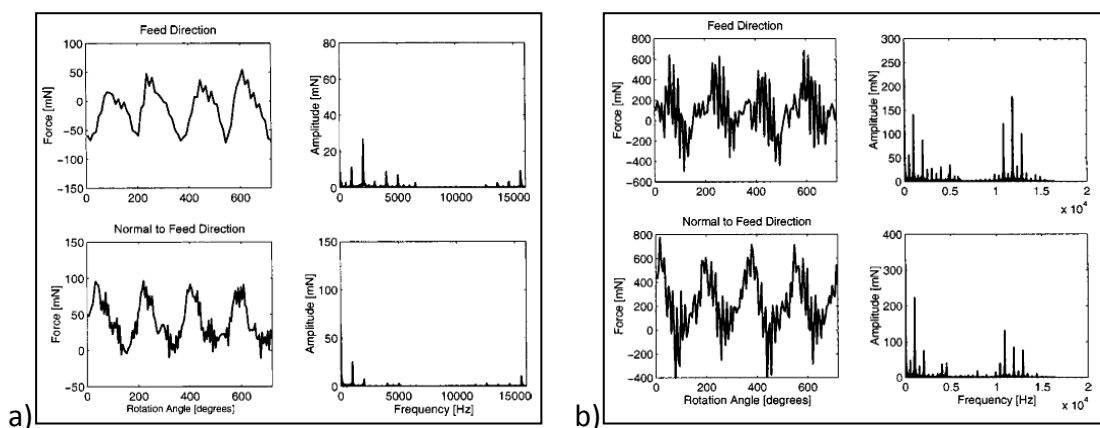


Fig. 1.10: Experimental forces and corresponding spectra for tests on a) single-phase ferrite and b) multiphase ductile iron [18].

Another study by Vogler et al. [19] investigates the effect of the material microstructure on the surface generation process; it shows that the surface roughness values ( $R_a$ ) for multiphase ductile iron (Fig. 1.11 b) are larger than those for the single-phase material (Fig. 1.11 a).

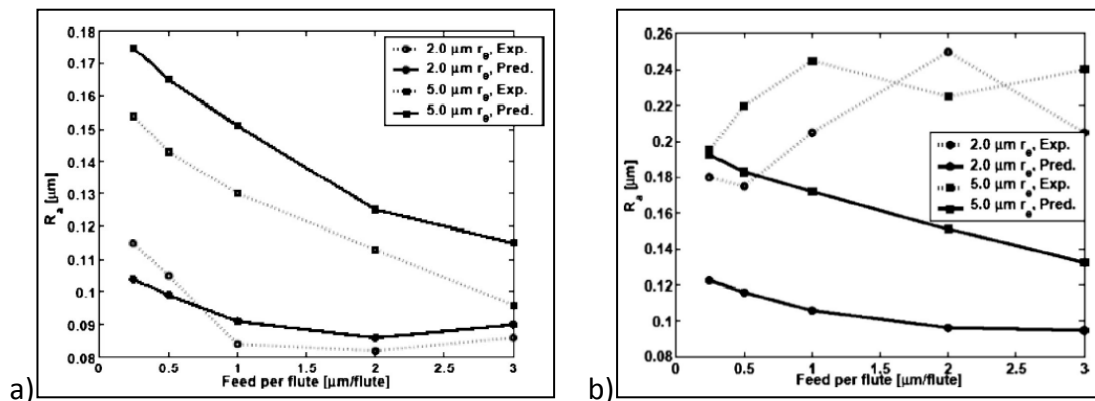


Fig. 1.11: Experimental and predicted roughness for tests on a) single-phase pearlite and b) multiphase ductile iron [19].

The explanation of the surface roughness increase was found in interrupted chip formation that takes place as the cutting edge passes through the different phases; this assumption is supported by the frequency spectra of the surface trace which are relatively flat and much lower in magnitude for ferrite and pearlite than for multiphase ductile iron.

### 1.1.5 Stable built-up edge

Several studies (such as the ones by Waldorf et al. [21-22] and Kountanya et al. [23]), assume that when machining in the microscale, there is a stable built-up edge adhering to the tool, which they call "dead metal cap". This statement has been proved by Waldorf et al. [22] thanks to machining experiments on aluminum 6061 [3]: they found out that a ploughing force model considering a stable build-up much better matches the experimental results than a model without it.

Kountanya et al. [23] carried out a study of micro-orthogonal cutting of cartridge brass with using a blunt tool and they observed the formation of a stable built-up edge by means of a high magnification visual (Fig. 1.12 b).

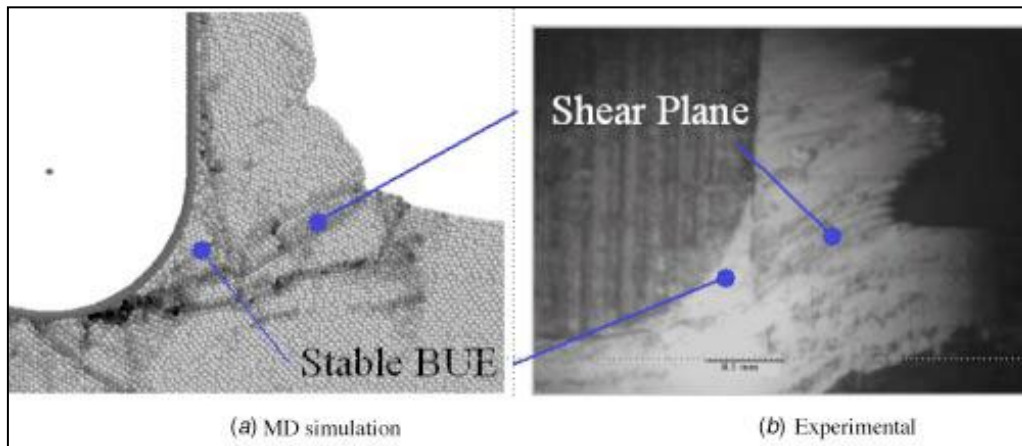


Figure 1.12. Material flow near a rounded cutting edge [3], b) from [23].

### 1.1.6 Cutting forces variability

Annoni et al. [24] made an analysis of the sources of force variability in micro-end-milling basing on a mechanistic force prediction model (derived from [10]) employed for a Montecarlo simulation; they found out that typical tolerance ranges and uncertainties due to the state-of-the-art tool tolerances, the process parameters and the target material behaviour are responsible for a wide variability of forces.

## 1.2 Quick Stop Devices

A Quick Stop Device (QSD) is a system which allows to freeze the chip formation in a steady condition by abruptly interrupting the cutting action; for this reason, it is a fundamental tool to study the chip formation process in mechanical machining.

Several different QSDs have been developed in past years to be used in studying macrocutting but no one has been especially designed for the microscale; some of the devices built for the macroscale have been used also for a smaller uncut chip thickness, for example in [44, 47-48], and a study about the cutting process in micromachining [49] has been carried out by means of a servo-hydraulic test machine, which is not able to provide the same performance of a quick-stop device and risks not to properly interrupt the cutting action. For this reason it has become necessary to design a new QSD suitable to be used within the typical cutting requirements of micromachining in order to better study the chip formation.

It is very important to characterize the performance of a QSD in order to validate the experiments carried out with it, but the existing studies show that often this is not made or it is made only once, before using the device, instead of during each quick stop test.

### 1.2.1 QSDs classification

A complete classification of the existing QSDs to use for orthogonal cutting conditions (summarized in Fig 1.13) can be derived from the partial classifications presented in the works of Hastings [27], Philip [33] and Black et al. [39].

The QSDs can be classified in two main groups basing on the situation they are applied to:

- i) the workpiece moves at the cutting speed  $V_c$  ([25, 27-28], "Aachen 1", "Aachen 2", "Aachen 3", "Berlino", "Delft 1", "Delft 3", "Göteborg", "Pisa 1" and "Pisa 2" in [29], [30-35, 38-39, 41-45, 47-48, 50]);
- ii) the tool moves at  $V_c$ .([26, 37, 46]).

The QSDs can then be divided according to the way they freeze the cutting process:

- i) by accelerating the stationary component - tool or workpiece - during cutting operations, making it faster than the cutting speed ([25-28], "Aachen 1", "Aachen 2", "Aachen 3", "Berlino", "Delft 3" and "Göteborg" in [29], [30-39, 41-48, 50]);
- ii) by decelerating the moving component ("Delft 1", "Pisa 1" and "Pisa 2" in [29]); the drawback is that some forces risk to be transmitted to the machine spindle (as in the analyzed devices) or structure and this can cause some undesirable effects.

In both cases, the tool-workpiece separation can be performed by means of several methods:

- i) quickly dropping the stationary component ([25, 45-46, 50]); the drawback is that the tool ([25, 45, 50]) or the workpiece ([46]) is retracted mainly thanks to the cutting force, therefore its acceleration is lower than in the other cases;
- ii) employing one or more shear pins ([26-28], "Aachen 1", "Berlino", "Delft 3" and "Göteborg" in [29], [30-39, 42-44, 47-48]); the drawback is that pins have to be carefully designed in order to resist to the cutting forces and to instantaneously break when an extra force is applied;
- iii) destroying the tool ("Aachen 2" and "Aachen 3" in [29], [41]); the drawback is that the same tool cannot be used for more than one experiment and this can introduce a certain variance in results; moreover,

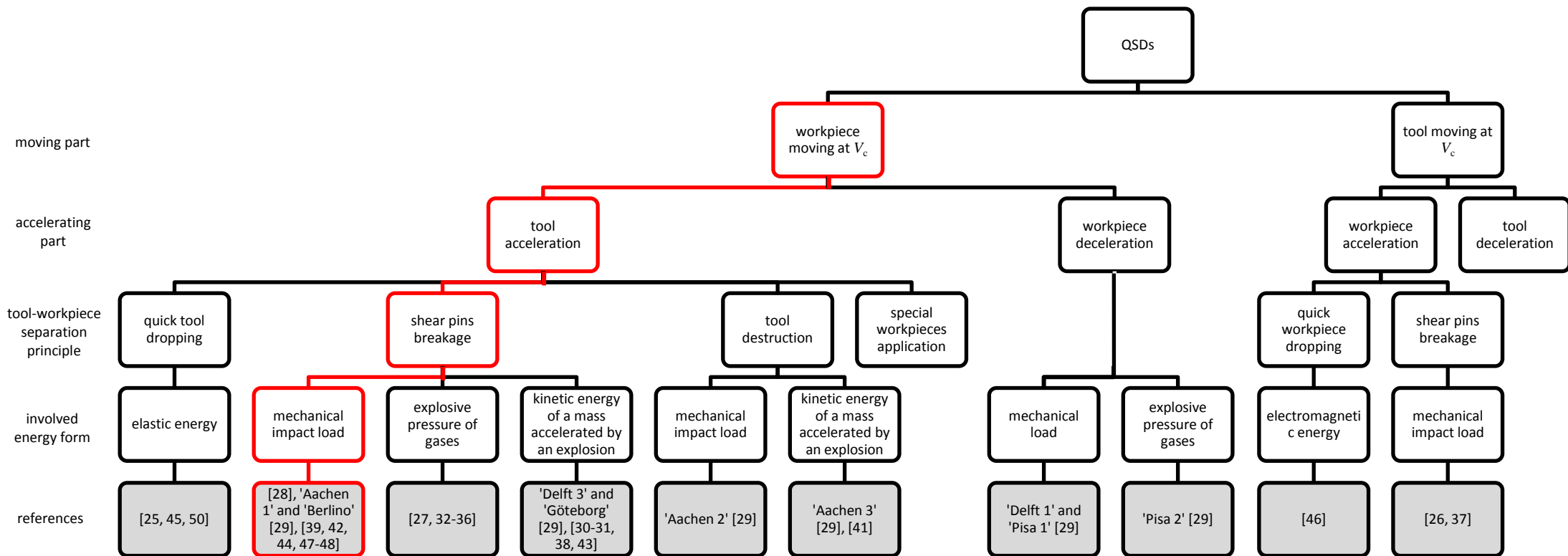
this way the tool trajectory during disengagement from the workpiece cannot be controlled and the chip risks to be damaged;

- iv) using especially designed workpieces; the drawback is that the workpieces have to be designed referring to the used device.

All these actions can be carried out by means of different energy forms:

- i) elastic energy ([25, 45, 50]); the drawback is that the moving component acquires an acceleration which is lower than in the other cases;
- ii) mechanical impact load ([26, 28], "Aachen 1", "Aachen 2", "Berlino", "Delft 1" and "Pisa 1" in [29], [37, 39, 42, 44, 47-48]); this is the easiest and safest way;
- iii) explosive pressure due to the ignition of some gases ([27], "Pisa 2" in [29], [32-36]); the drawback is that the explosion introduces some safety risks;
- iv) kinetic energy of a mass accelerated by an explosion ("Aachen 3", "Delft 3" and "Göteborg" in [29, 30-31, 38, 41, 43]); the drawback is that the explosion introduces some safety risks;
- v) electromagnetic force ([46]); the drawback is that the moving component acquires an acceleration which is lower than in the other cases.

Figure 1.13. Classification of existing QSDs (in red the solutions chosen for the micro QSD developed in the present study).



## 1.2.2 QSDs performance

In 1972 Brown and Komanduri, in their survey about QSDs [34], stated the essential requirement of quick-stop experiments (also reported later by Black [39] and Griffiths [40]) : “a specimen obtained by a quick-stop device should not be grossly influenced by the stopping conditions”. Since it is impossible to build a device with infinite acceleration, which is able to stop the cutting process in a null time, it is necessary to set some criteria to evaluate the performance of a QSD.

In order to reach this target, first of all it is necessary to make a general description of a quick-stop experiment with reference to the scheme of Fig. 1.14 (derived from the one introduced in the work of Ellis et al. [30] and then used also by Wu [46]) which represents the experimental set-up implemented in the present study.

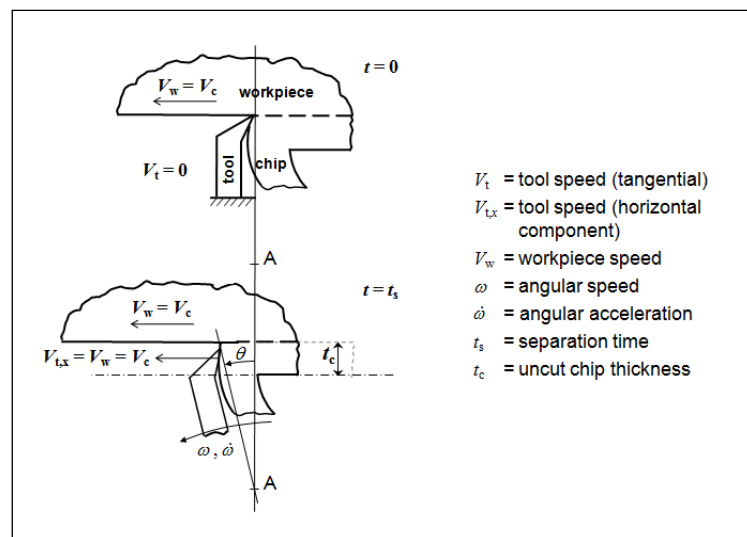


Fig. 1.14: Scheme of a quick-stop experiment with the micro QSD developed in this study (adapted from [30]).

The tool-workpiece separation begins at the instant  $t = 0$  and ends after the so-called “separation time”  $t = t_s$ , which has been defined [46] as the time that the moving part (the tool in Fig. 1.14) needs to pass from  $V_{t,x} = 0$  to  $V_{t,x} = V_c$ , the tool-workpiece relative speed to become equal to zero and the cutting action to stop.

According to Ellis et al. [30], the separation time  $t_s$  allows to calculate the so-called “separation distance”  $d_s$ ; it is defined as the distance the workpiece covers relatively to the tool during the tool-material separation process and it

can be obtained with the following equation, also derived from [30] (see Equation (1.2) in Section 1.2.3, Group 4).

$$d_s = d_w - d_t = V_c \cdot t_s - \int_0^{t_s} V_{LX}(t) dt \quad (1.1)$$

During the separation transient, the chip is subject to compressive and frictional actions which do not take place during the chip formation steady conditions. Taking into account the micro QSD the cutting edge moves downwards and the effective rake angle seen by the chip varies (due to the tool holder rotational motion during the transient); this fact does not necessarily imply that the chip is really affected by the separation process (because some effects could be eliminated by the elastic recovery), but, in any case, it points out that the transient time  $t_s$  should be as lower as possible in order to obtain the most unaffected conditions.

Since the tool holder motion is rotational, the tool can get out of the cutting area also for high values of the angular position  $\theta$ , even if the tool speed is not higher than the cutting speed, because the cutting edge distance from the machined surface becomes bigger than the uncut chip thickness; in this case the cutting action ends as well, but the chip alteration takes place for a longer time so it is better to avoid this separation way thanks to sufficiently high angular speed  $\omega$  and acceleration  $\dot{\omega}$ .

The above outlined observations underline that the best way to characterize a QSD performance is to measure the separation time  $t_s$  and then derive the separation distance  $d_s$ , because this is the length along which the chip continues to be affected from the tool, even if it is working in transient conditions. Therefore, since the objective of a QSD is to capture the steady cutting condition,  $t_s$  and  $d_s$  have to be minimized to improve the system performance.

The literature survey shows that the separation time  $t_s$  ([26-27, 30-31, 33, 37-38, 40-41, 46]), the separation distance  $d_s$  ([27, 30-31, 33-34, 40-41, 46]) and the angular acceleration  $\dot{\omega}$  (or the linear one when applicable, [27, 31-34, 39-40, 48]) can be used as indicators of a quick stop device performance (see Tab 1.1). It should be noticed that some works [40-41] underline the importance of expressing the QSD performance through the ratio between the separation distance  $d_s$  and the uncut chip thickness  $t_c$ , in order to evaluate the relative length of the workpiece zone affected by the transient taking into account the specific magnitude order of each test.



Table 1.1. Use of parameters for QSDs performance evaluation.

paper	acceleration	separation time $t_s$	separation distance $d_s$	$d_s / t_c$
[25]				
[26]		X		
[27]	X	X	X	
[28]				
[29] all devices				
[30]	[34]	X	X	
[31]	X	X	X	[40]
[32]	X	[34]	[34]	
[33]	X	X	X	
[34]	X	X	X	
[35]				
[37]		X		
[38]	[39]	X	[39]	
[39]	X			
[40]	X	X	X	X
[41]		X	X	X
[42]				
[43]				
[44]				
[45]				
[46]		X	X	
[47]				
[48]	X			
[50]				

### 1.2.3 QSDs details

All the existing QSDs used for the orthogonal cutting condition are briefly described in the following together with their performance characterization, if any. The devices are presented divided into the groups of the classification summarized in Fig. 1.13, reading the graph from left to right.

1) workpiece moving at  $V_c \rightarrow$  tool acceleration  $\rightarrow$  quick tool dropping  $\rightarrow$  elastic energy

In this kind of QSDs the tool is retracted from the workpiece thanks to the elastic force given by a spring and the cutting force, thus its acceleration is lower than in devices with another operation principle.

- In the QSD developed by Kececioglu [25], the tool block (A in Fig. 1.15) is mounted on a pivot and its edge (F in Fig. 1.15) opposite to the cutting one is in contact with a rotating pin (B in Fig. 1.15) which has a flat surface (E in Fig. 1.15) at its end; when the pin is manually rotated by the operator, the flat surface gets in contact with the tool block and this is free to rotate downward under the action of the cutting force acting on the cutting edge ( $F_c$  in Fig. 1.15) and of the force ( $Q$  in Fig. 1.15) applied by a spring (C in Fig. 1.15) and transmitted thanks to a bar (D in Fig. 1.15).

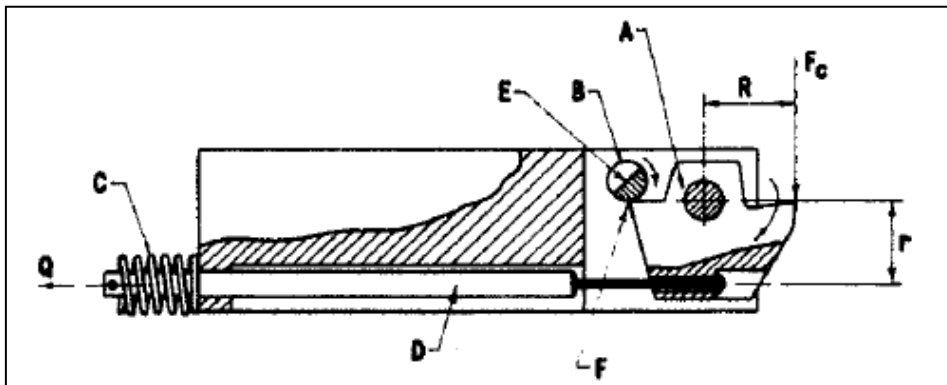


Fig. 1.15: Scheme of the QSD developed by Kececioglu [27].

Both in the work of the author who developed the device [25] and in the paper by Hastings [27] which described and commented it there is no mention to a performance measurement but in [25] some frames taken with a high speed camera (with an acquisition frequency of 60 and 3500 frames/s) are shown

since they have been used to better understand the tool motion during disengagement from the workpiece.

- Also in the QSD proposed by Chern [45] (Fig. 1.16), the tool-workpiece separation is performed exploiting the elastic load of a spring and is helped by the cutting force.

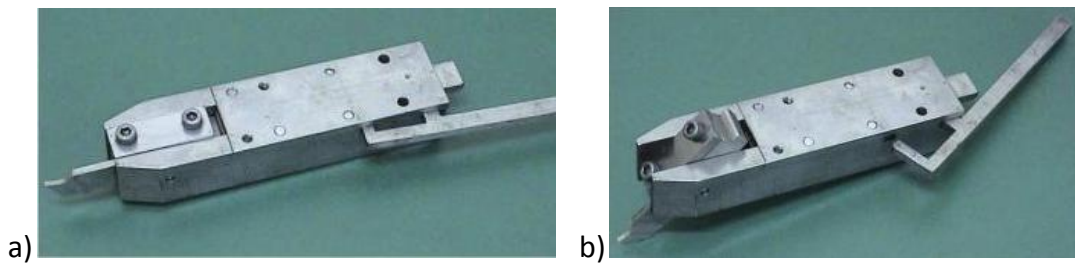


Fig. 1.16: QSD developed by Chern [45] a) before and b) after triggering.

During the cutting process, the force applied on the tool unit is resisted by the sliding block (B in Fig. 1.17) which is constrained by the trigger (C in Fig. 1.17), the device body (A in Fig. 1.17) and the cover plate (L in Fig. 1.17). When the trigger is manually rotated by the operator, it leaves the block free to slide on the device body so it is accelerated by two compressed springs (D in Fig. 1.17); the block motion allows the tool unit to rotate due to cutting force applied by the workpiece and the thrust force coming from the spring (F in Fig. 1.17) which is originally compressed between the device body and a plate (G in Fig. 1.17).

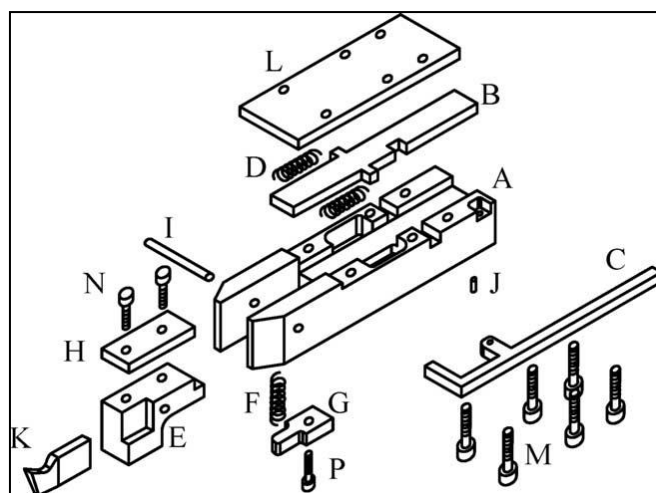


Fig. 1.17: Exploded model of the QSD developed by Chern [45].

In his work [45], the author explicitly says that the separation time has not been analytically studied or measured due to the limitation of the equipment but, basing on [38], he states that the uniformity of chip thickness can be considered as a measure of the efficiency of his QSD.

The QSD by Chern has been tested in quick-stop experiments on AISI 1017 low carbon steel with  $V_c = 14.1, 21.2, 24.3, 45.6$  m/min and  $f = 0.101, 0.130, 0.165, 0.191$  mm/rev; tests have been carried out using a high-speed steel tool (rake angles  $\gamma = 5, 10, 15, 20^\circ$ ; clearance angle  $\alpha = 20^\circ$ ). The following figure shows some micrographs obtained in those experiments, where Chern observed a built-up edge; these results are significant compared to those achieved thanks to the micro QSD developed in the present study (see the results of preliminary quick-stop tests in Chapter 5).

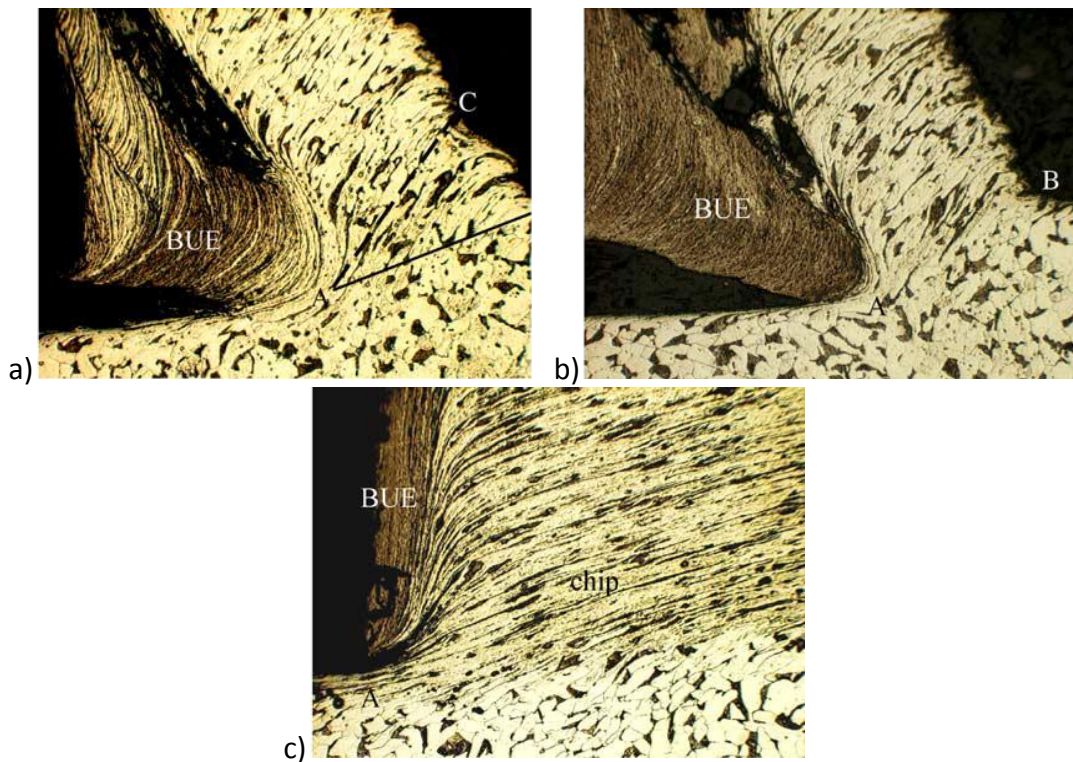


Fig. 1.18: Chip micrographs 200 x ; a)  $V_c = 24.3$  m/min,  $f = 0.101$  mm/rev,  $\gamma = 20^\circ$ ; b)  $V_c = 45.6$  m/min,  $f = 0.101$  mm/rev,  $\gamma = 10^\circ$ ; c)  $V_c = 45.6$  m/min,  $f = 0.191$  mm/rev,  $\gamma = 5^\circ$  [45].

- Zeb et al. [50] designed a QSD (Fig. 1.19) to be used on a vertical machining center with the workpiece mounted in the spindle and the device (with the cutting tool) fixed on the table. From this point of view, it is similar to the micro quick-stop device presented in the present study while all the analyzed QSDs

(except the ones by Wu et al. [46], Hsu [26] and Vorm [37]) have been designed to be mounted on a lathe.

As in the previous devices, the tool withdrawal from the workpiece is carried out by a spring but in this case the tool motion is translational and not rotational.

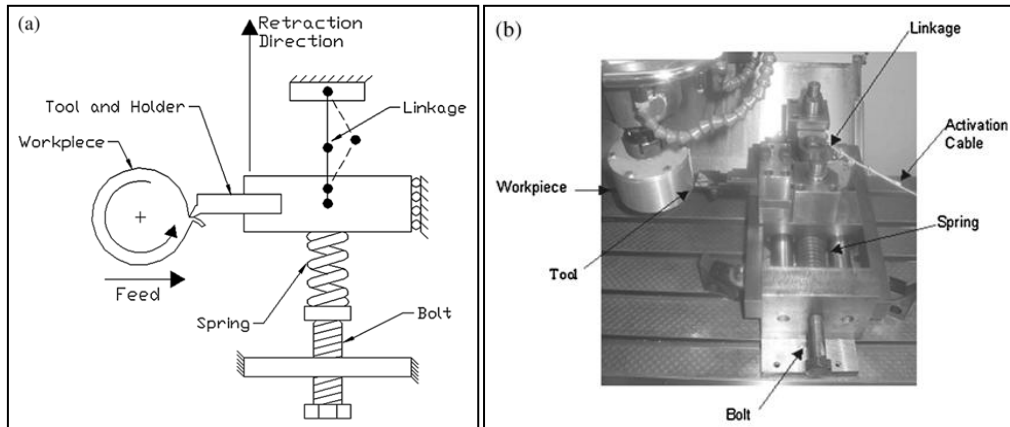


Fig. 1.19: Scheme and picture of the QSD developed by Zeb et al. [50].

No performance measurement has been performed by Zeb et al.

2) workpiece moving at  $V_c$  → tool acceleration → shear pins breakage → mechanical impact load

The main drawback of the QSDs of this Group is that shear pins have to be carefully designed in order to resist to the cutting forces and to instantaneously break when the mechanical impact load is applied.

- The QSD (Fig. 1.20) developed by Ponkshe [28] has been later used by Joshi et al. [44] and by Subbiah et al. [47-48] for studying chip formation in micromachining.

When steady cutting condition has been reached, a hammer blow manually applied to the top of the tool holder makes the notched shear pin break; this fact causes the tool holder to swivel out quickly, also because of the action of a spring.

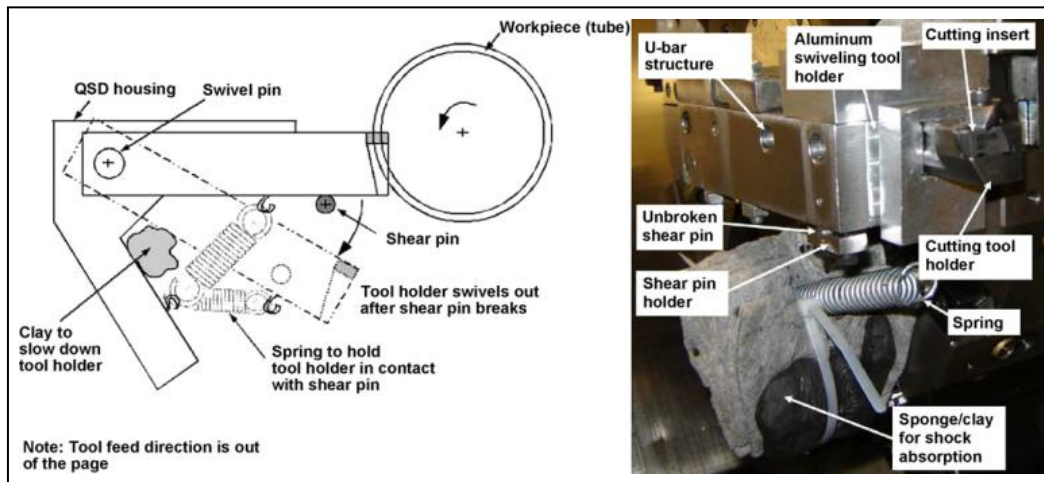


Fig. 1.20: Scheme and picture of the QSD developed by Ponkshe [28] and used by Joshi et al. [44], Subbiah et al. [47-48].

In the first work by Subbiah et al. [47] the QSD performance has been estimated as similar to the one of the device proposed by Black et al. [39] (i.e. acceleration of about  $10^8 \text{ m/s}^2$ ) where the blow is given by a hammer mounted on the device and not manually; in the following paper [48] the authors claim to have measured an acceleration of the tool holder equal to  $1.65 \pm 0.15 \cdot 10^3 \text{ m/s}^2$  but they do not specify the measurement procedure and timing (see Tab. 1.4).

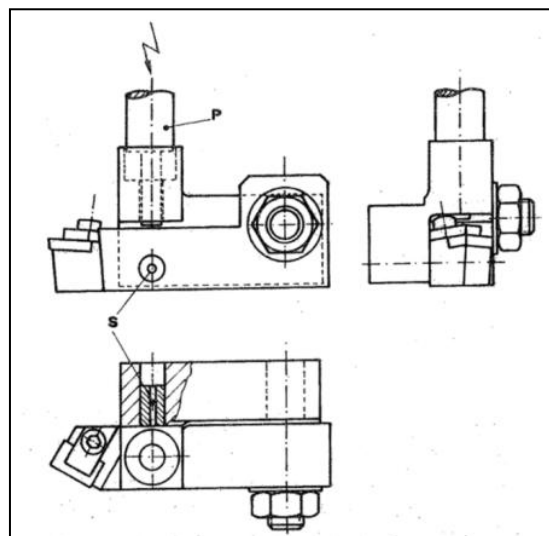


Fig. 1.21: Scheme of the "Aachen 1" QSD described in [29].

- The “Aachen 1” QSD described in the review by Giusti [29], the tool separates from the workpiece rotating around a swivel after the shear pin (S in Fig. 1.21) breakage caused by a hammer blow on the striker (P in Fig. 1.21). The review made by Giusti [29] does not talk about performance for all QSDs presented in it.
- The “Berlino” QSD shown in [29] has an operation similar to the “Aachen 1” device (the tool holder block, C in Fig. 1.22, moves away from the workpiece by swiveling) but in this case the striker (P in Fig. 1.22) rotates together with the workpiece (L in Fig. 1.22) and hits the tool holder with a speed ( $V_1$  in Fig. 1.22,  $V_{imp}$  in standard symbology) higher than the cutting speed ( $V$  in Fig. 1.22,  $V_c$  in standard symbology).

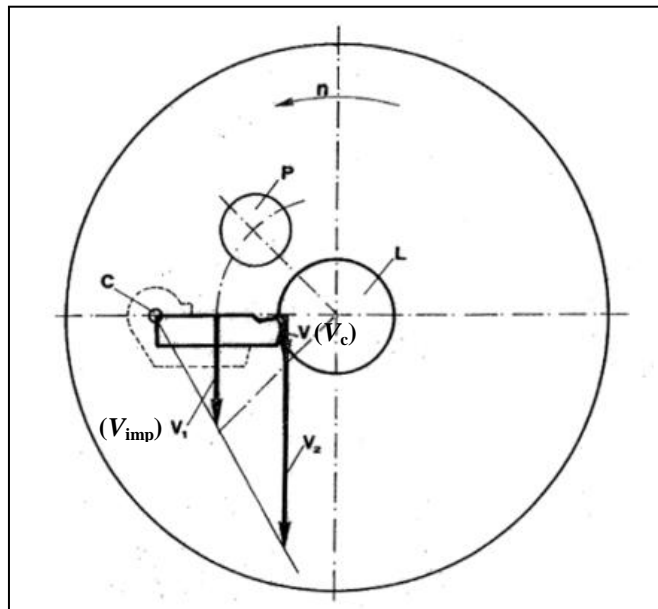


Fig. 1.22: Scheme of the “Berlino” QSD described in [29] (in brackets standard symbols).

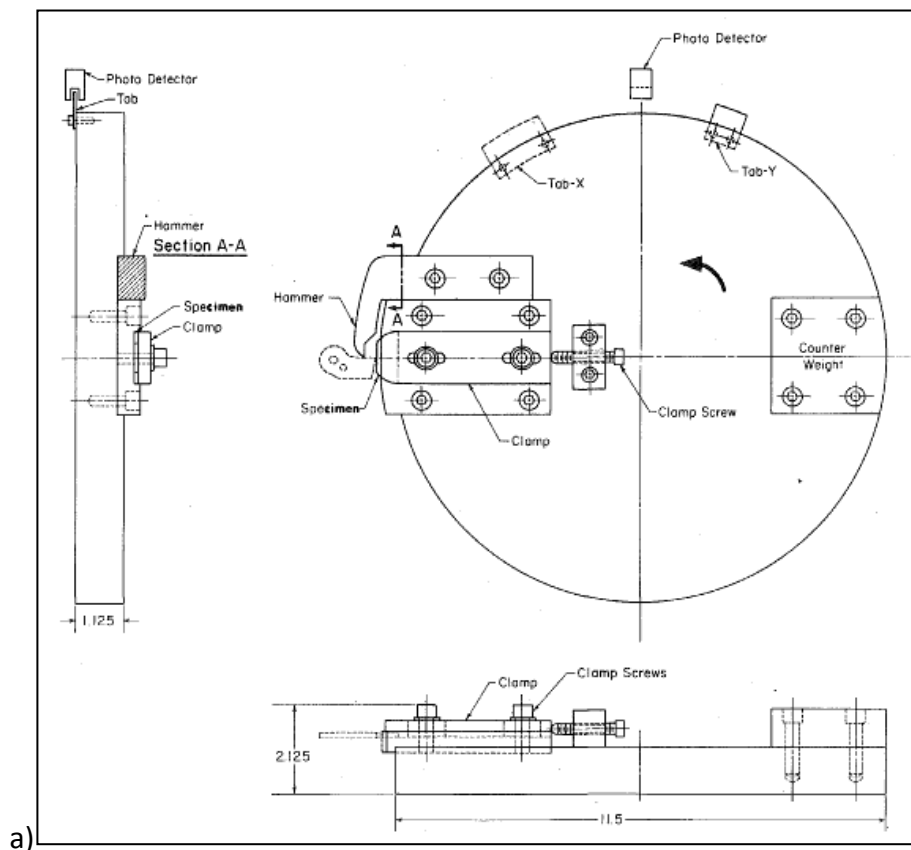
- In the device proposed by Black et al. [39], called “hammer QSD”, the tool is disengaged from the chip by accelerating it thanks to an hammer travelling with the workpiece, hence the rate at which the tool is removed is keyed to the cutting speed.

In this QSD, the workpiece and the hammer (used to remove the tool from the cutting area by breaking a shear pin) travel together and are mounted in a workholding device (Fig. 1.23 a) that replaces the traditional face plate on the lathe; the specimen is mounted in a radial configuration and held in place by a

clamp while the hammer is mounted above the specimen holder so it hits the tool behind its cutting edge.

The tool, which has a pivot and a shear pin, is fixed into a yoke; both the tool and the yoke are mounted in a device (Fig. 1.23 b) which replaces the tool post on the lathe; this device is held by a pivoted shank which has two positions: a latched one and a closed one. When the shank is maintained in the latched position by the latch plate, the tool is out of the workpiece trajectory so the workpiece can be brought up to the desired cutting speed; when the plate containing the workpiece and the hammer (Fig. 1.23 a) is up to the desired speed, the photodetector is activated and the solenoid is triggered so it releases the tool shank, which is driven in the cutting position by means of a heavy spring.

Once this configuration is achieved, the workpiece engages the tool which makes a cut to about the halfway point of the specimen and then the hammer strikes the tool, driving it away from the workpiece.





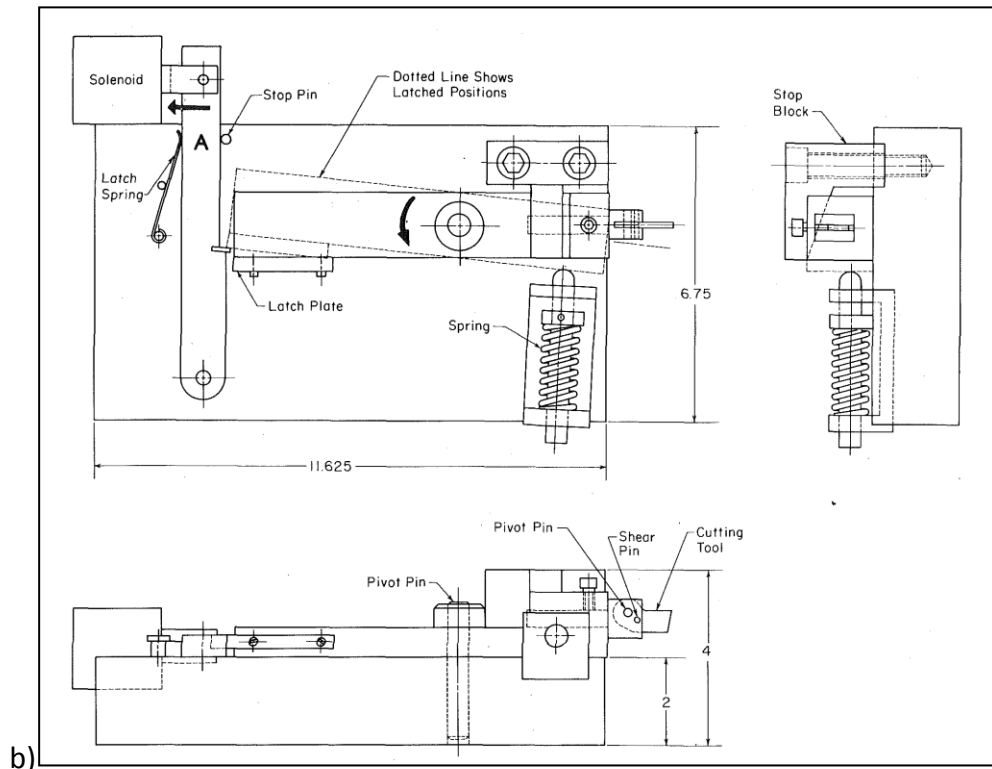


Fig. 1.23: Scheme of the QSD developed by Black et al. a) face plate and b) tool pivoting device [39].

Black et al. [39] estimated the performance of their QSD by means of acquisition made with a high speed camera with a frequency of 4000 frames/s during tests with a cutting speed of 20.32 m/s; since the tool has been removed completely from the workpiece within two frames, the author declare an acceleration of about  $10^8 \text{ m/s}^2$  (see Tab. 1.4).

Black et al. state that their device is similar in some respects to the one built by Kececioglu [25] which has a completely different working principle (since it uses a spring to withdraw the tool) but also exploits the cutting force as the “hammer QSD” does. Anyway, unlike the device by Black et al. , the one by Kececioglu is speed limited due to its slow rate of retraction and produced specimens not truly representative of the steady state process, according to Hastings [27] who reviewed this QSD.

- The QSD designed by Yeo et al. [42] to be used on a lathe has a working principle similar to the previously presented device by Black et al. [39]. A workpiece holder (1 in Fig. 1.24) is fixed on the spindle and a workpiece (5 in Fig. 1.24) is mounted on it together with a hammer (2 in Fig. 1.24) which is

used to provide an impact onto the tool holder, removing the tool from the cutting path. The tool-holder (4 in Fig. 1.24), which is pivoted at its end (7 in Fig. 1.24), is maintained out of the cutting area by an energized solenoid (3 in Fig. 1.24) when cutting is not required; to perform the orthogonal cutting the solenoid is switched off and the tool-holder is swung into the cutting position, with its axial movement opposed by a spring (6 in Fig. 1.24). At a pre-determined cutting position (which is at about the mid-point of the workpiece), the tool-holder is disengaged thanks to the breakage of the two shear pins holding it due to the hammer blow.

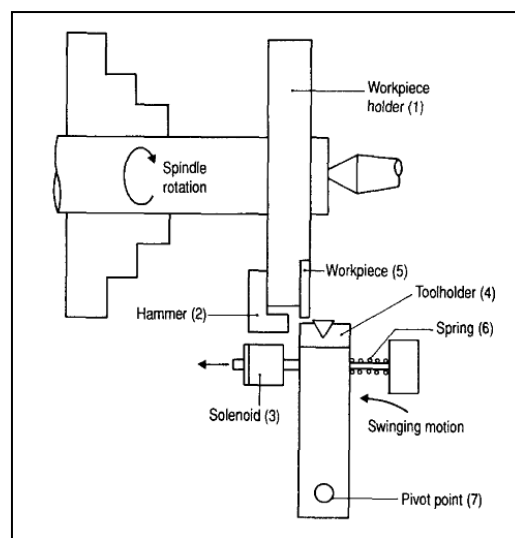


Fig. 1.24: Scheme of the QSD developed by Yeo et al. [42].

In their work, Yeo et al. do not make any performance measurement about the proposed quick-stop device.

**3) workpiece moving at  $V_c$  → tool acceleration → shear pins breakage → explosive pressure of gases**

As for the QSDs of Group 2, shear pins have to be carefully designed in order to resist only to the cutting forces but the main drawback of the devices of this Group is that the explosion introduces some safety risks.

- In order to overcome the problems associated with the use of quick-stop devices (such as the one by Kececioğlu [25] reviewed by Hastings in his paper

[27]) at high cutting speed, Hastings designed an explosively-operated tool holder (Fig. 1.25).

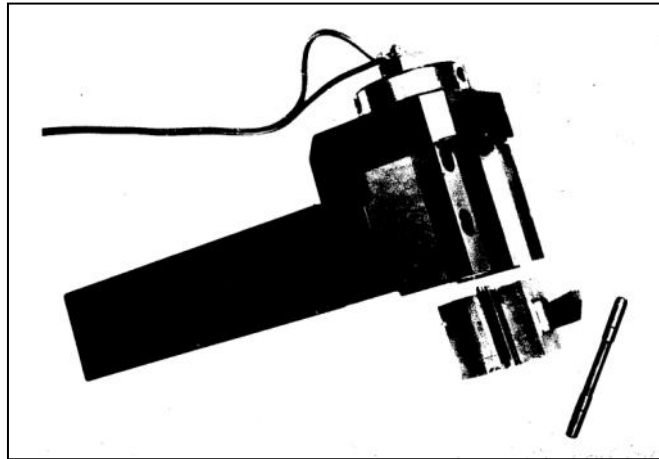


Fig. 1.25: QSD developed by Hastings [27].

An explosive charge (A in Fig. 1.26) located in the chamber (B in Fig. 1.26) provides the force necessary to break the notched shear pin (C in Fig. 1.26) which holds the tool holder block (E in Fig. 1.26) in the cutting position; this force is transmitted to the pin by means of a piston (D in Fig. 1.26).

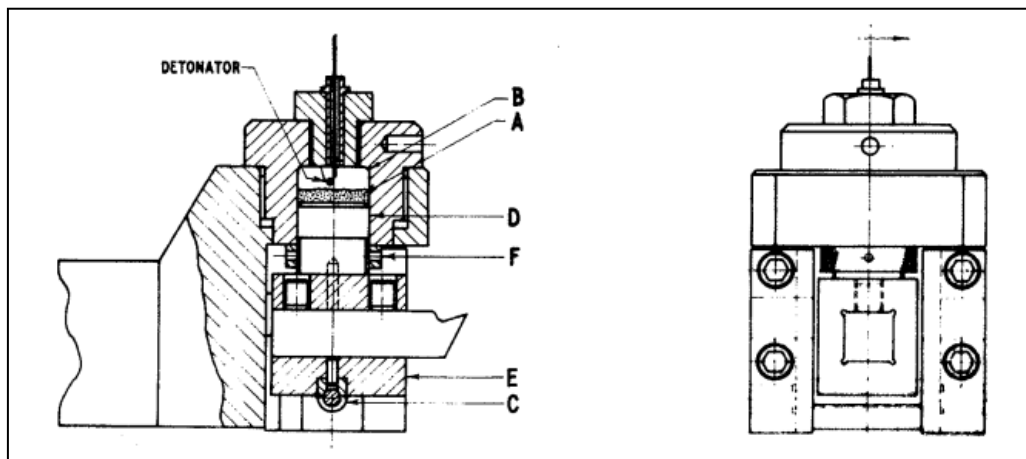


Fig. 1.26: Scheme of the QSD developed by Hastings [27].

As concerning the QSD performance (see Tab. 1.4), Hastings calculated the tool holder block acceleration from time-displacement records obtained using two independent methods: a high speed camera with an acquisition frequency of

3000 frames/s (used for recording the first half inch = 12.7 mm of movement) and a capacitive sensor (considering only the first 0.01 in = 0.254 mm of movement).

- The quick-stop device (Fig. 1.27) used in the study by Stevenson et al. [32] is basically the same one designed by Hastings [27] except for the shear pin material, which is cast iron instead of hardened steel.

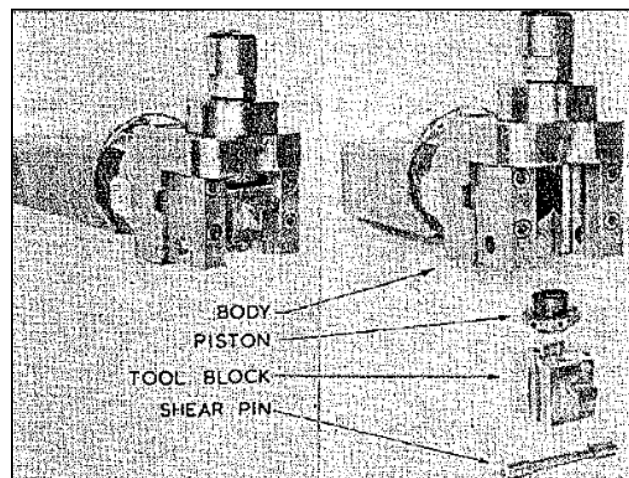


Fig. 1.27: QSD developed by Stevenson et al. [32].

Stevenson et al. measured the QSD performance by means of a wire strain gauge, glued between the device body and the tool block, during the first 0.002 in = 0.0308 mm of movement (for results see Tab. 1.4).

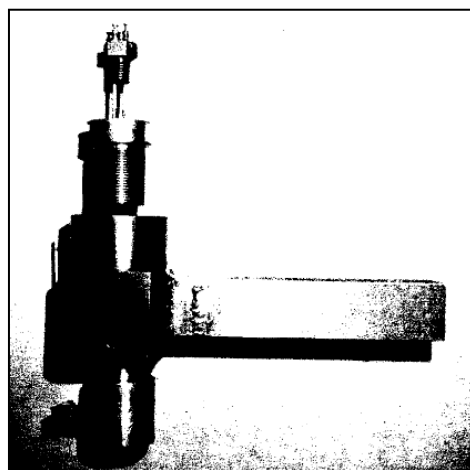


Fig. 1.28: QSD developed by Philip [33].

- The quick-stop device proposed by Philip [33] (Fig. 1.28) derives from the one designed by Hastings [27] but has a combustion chamber (5 in Fig. 1.29) with a variable volume and its shear pin (7 in Fig. 1.29) is preloaded, in order to improve the device stiffness and stopping efficiency.

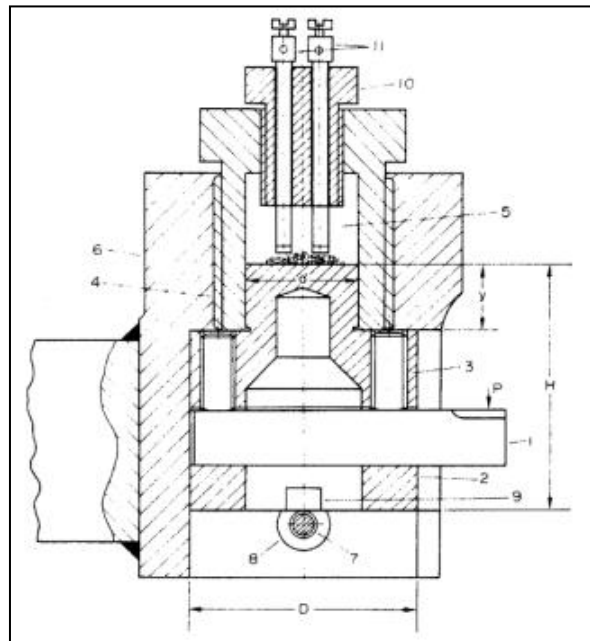


Fig. 1.29. Scheme of the QSD developed by Philip [33].

As said in Tab. 1.4, Philip evaluated the QSD performance thanks to a high speed camera with an acquisition frequency of 3000 frames/s both in case of non-preloaded and preloaded (with a torque of 7.75 kpm = 76 Nm) shear pin; results are shown in Tab. 1.2 and 1.3.

Table 1.2. Performance of the QSD developed by Philip with a non-preloaded shear pin [33].

Time $\frac{t}{3000}$ (sec)	Distance of tool travel (mm)	Acceleration (m/sec <sup>2</sup> )	Time for tool retraction at 100 m/min (msec)	Length of cutting during stopping (mm)
0	0			
7	2.0	$0.74 \times 10^3$	2.25	1.75
8	5.0	$0.22 \times 10^5$	—	—
9	9.0	$0.90 \times 10^4$	—	—
10	15.0	$1.80 \times 10^4$	—	—

Table 1.3. Performance of the QSD developed by Philip with a preloaded shear pin [33].

Time t (sec)	Distance of tool travel (mm)	Acceleration (m/sec <sup>2</sup> )	Time for tool retraction at 100 m/min (msec)	Length of cutting during stopping (mm)
0	0			
1	5.0	$0.9 \times 10^5$	0.0185	0.0154
2	12.0	$1.8 \times 10^4$	—	—

- In their study about chip segmentation in machining [35], Komanduri et al. used a quick-stop device developed by Brown et al. [34] (Fig. 1.31) which is almost identical to the one designed in Gladman et al. laboratory [36] (described by Hastings [27]) despite some minor changes: the tool holder and its slides have been tilted, the shank and the plunger dimensions have been changed, a safety helmet and some sensors (strain gauges and a piezoelectric transducer) have been added.

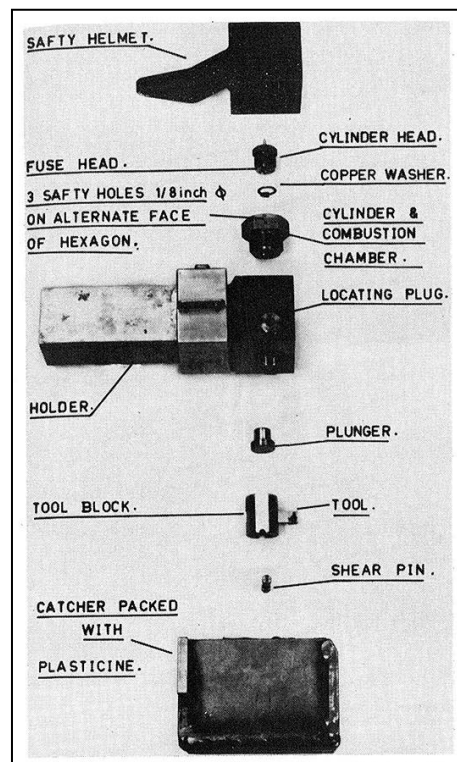


Fig. 1.30: Exploded view of the QSD developed by Brown et al. [35].

As concerning the device performance evaluation (see Tab 1.4), Brown et al. used a pressure transducer and a fotonic sensor (consisting of a tube of randomly oriented fiber optics) in order to record the displacement law of the tool holder and then calculate the separation time  $t_s$  and distance  $d_s$  as proposed by Ellis et al. [30] (whose QSD is in Group 4) and shown in the following graph (see Fig. 1.36).

In this case the performance measurement has been carried out thanks to an optical sensor as it has been done for the micro QSD by means of *ad hoc* built and calibrated angular position sensors (see Section 4.4).

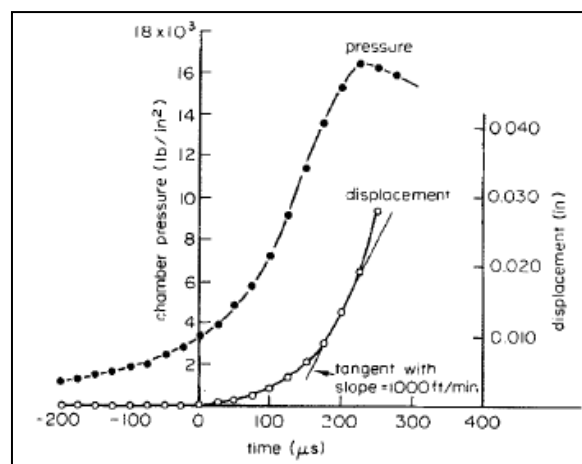


Fig. 1.31: Construction for  $t_s$  [35].

The time-displacement curve shown in Fig. 1.31 is very similar to the ones obtained in the performance measurement experimental campaigns (an example is depicted in Section 4.4 while all the graphs are shown in Appendix F).

**4) workpiece moving at  $V_c$  → tool acceleration → shear pins breakage → kinetic energy of a mass accelerated by an explosion**

QSDs belonging to this Group have the same drawbacks of the ones in Group 3.

- The “Delft 3” quick-stop device described in [29] carries out the tool-workpiece separation by means of the explosion of a cartridge (X in Fig. 1.32) which allows a cylinder (A in Fig. 1.32) to break a brass plate and hit the striker (P in Fig. 1.32); this makes the tool holder break the shear pin holding it in cutting position (S in Fig. 1.32) and rotate around a pivot (Y in Fig. 1.32).

Giusti's review [29] underlines that the pivot is not horizontal but is at an angle equal or higher than the helix of tool-workpiece relative motion.

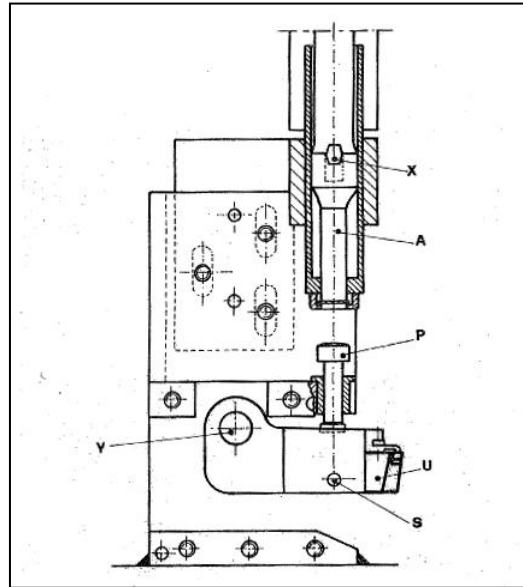


Fig. 1.32: Scheme of the "Delft 3" QSD described in [29].

- Like in the previous one, in the "Göteborg" QSD presented in the review by Giusti [29], the tool is disengaged from the workpiece thanks to the breakage of a shear pin (S in Fig. 1.33) due to the blow given by a mass accelerated by an explosion. The kinetic energy of the tool holder rotating around its hinge (A in Fig. 1.33) is absorbed by a lead pad (Q in Fig. 1.33).

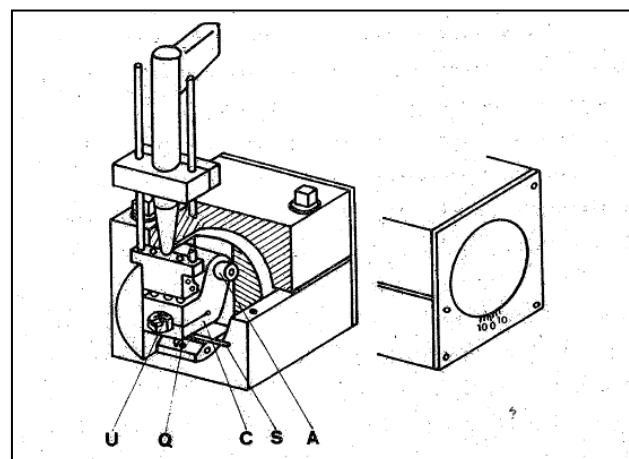


Fig. 1.33: Scheme of the "Göteborg" QSD described in [29].



- Ellis et al. [30] (Fig. 1.34) have chosen a straight line retraction of the tool from the workpiece for their QSD instead of a pivoted one as in the above described devices.

In the quick-stop device designed by Ellis et al. , the tool block, positioned within two slides, is supported by a notched shear pin during the cutting execution. When the gun is fired, a captive bolt is accelerated towards the tool block, the shear pin breaks due to its impact and the tool block accelerates downwards until it is arrested by plasticine.

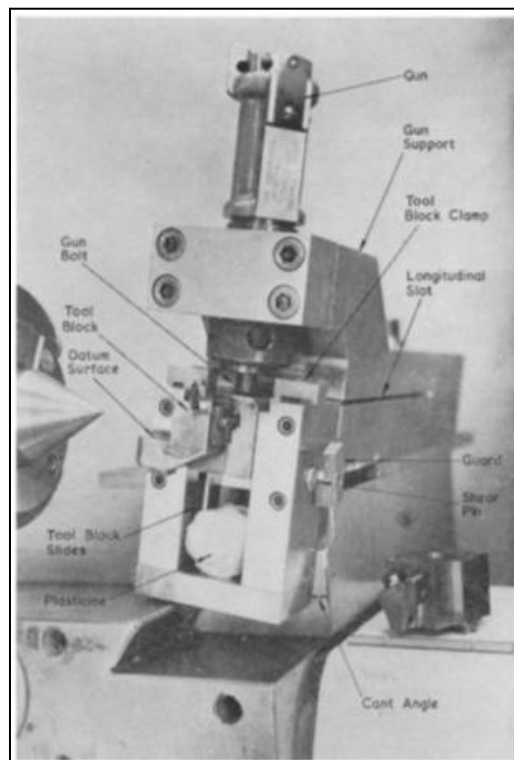


Fig. 1.34: QSD developed by Ellis et al. [30].

In their work [30], Ellis et al. introduced a simple scheme of the tool-workpiece separation, which is shown in Fig. 1.35. This scheme is so effective that it has been used to derive the scheme of a quick-stop experiment with the micro QSD which is presented in Fig. 1.14.

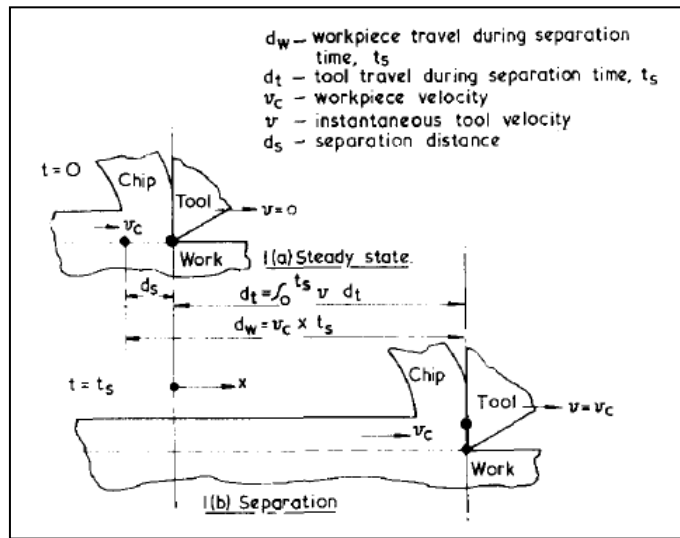


Fig. 1.35: Scheme of the tool-workpiece separation process [30].

The authors used a capacitive sensor to acquire the time-displacement curve of the tool block during its separation from the workpiece, in order to estimate the separation distance  $d_s$  according to the following equation (which is the origin of Equation (1.1) and comes from the scheme of Fig. 35):

$$d_s = d_w - d_t = v_c \cdot t_s - \int_0^{t_s} v_t(t) dt \tag{1.2}$$

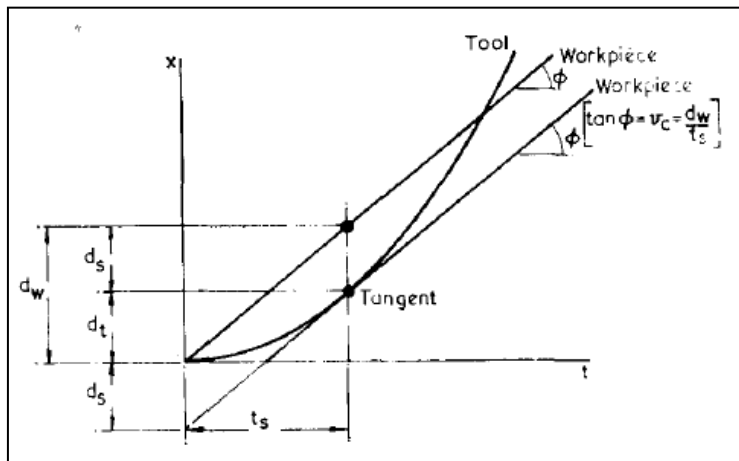


Fig. 1.36: Construction for  $t_s$  and  $d_s$  [30].

The separation time  $t_s$ , which should be used in Equation (1.2), can be obtained from the time-displacement graphs as shown in the construction of

Fig. 1.36: since it is the amount of time the tool needs to pass from  $V_t = 0$  to  $V_t = V_c$ , it corresponds to the instant when the tool displacement curve is tangent to a line with a slope equal to the cutting speed. Then, the difference between distances covered by the tool  $d_t$  and by the workpiece  $d_w$  (which is constantly moving at  $V_c$ ) is equal to their relative displacement after the separation time  $t_s$  which is the the separation distance  $t_s$ .

- In the QSD proposed by Williams et al. [31] (Fig. 1.37), the tool disengagement motion is again rotational, in fact the tool holder is pivoted at its end and is held into cutting position by means of a shearing pin, towards which it is pushed by a spring. When the cutting action should be interrupted, an experimenter manually fires a gun and a bolt hits the tool holder, which suddenly swings away from the cutting zone.

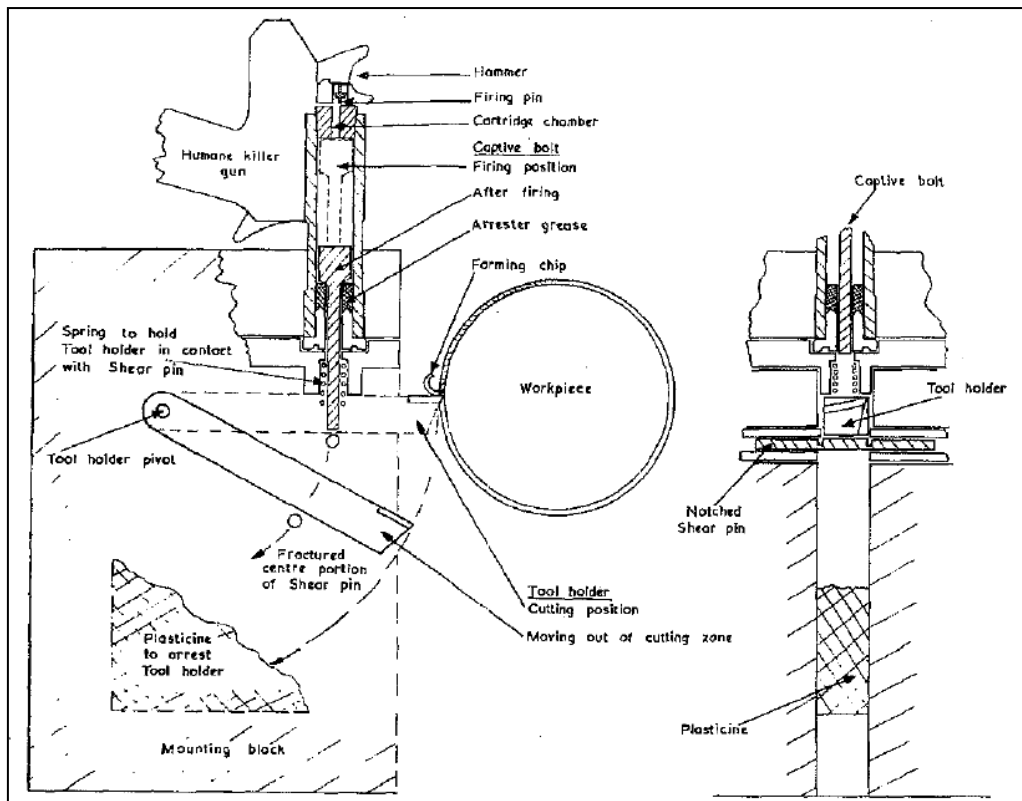


Fig. 1.37: Scheme of the QSD developed by Williams et al. [31].

A high-speed camera has been used by Williams et al. to evaluate the QSD acceleration basing on a record of the first 0.1 in = 2.54 mm (see Tab 1.4).

- Brown [38] states in his study that all the QSDs employing an explosive charge (either acting directly on a tool block or driving a bolt against it) can give a high acceleration rate to the tool block shortly after the shear pin breakage but all have a relatively low initial acceleration. For this reason, Black has designed a double pins quick-stop device (Fig. 1.38) such that a time delay is introduced between the explosive ignition and the blow against the tool block. This was achieved by setting a short free flight distance for the plunger before it strikes the tool block; by an appropriate selection of the free flight distance and a correct choice of the pin dimensions, the plunger can be made to strike the tool block as the explosive gas pressure approaches its maximum value, this way leading to a lower energy loss.

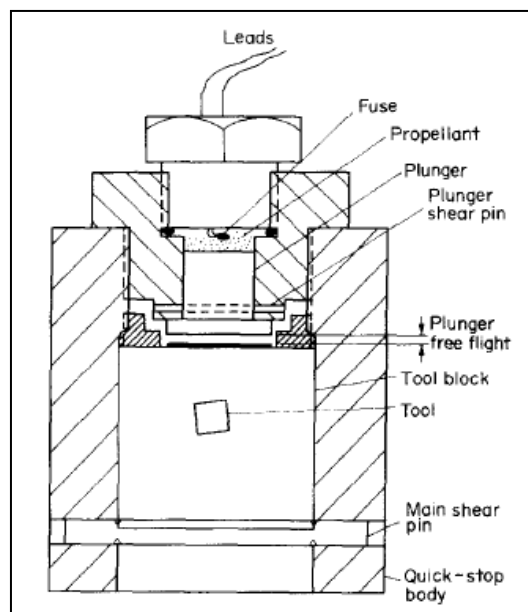


Fig. 1.38: Scheme of the QSD developed by Brown [38].

Also in this study, Brown used a pressure transducer and a photonic sensor (see the device used by Komanduri et al. in Group 3) to acquire the displacement of the tool holder and this way evaluate the QSD performance, which is of a magnitude order higher than the one of the single pin conventional devices (as stated in [40]).

- The quick-stop device used by Lin et al. [43] is very similar to the one designed by Williams et al. [31]: during machining the swiveling tool holder (H in Fig. 1.39), where a cutting insert (G in Fig. 1.39) is fixed by means of a tool

clamp (F in Fig. 1.39), is supported by a double-necked shear pin (I in Fig. 1.39) and also held by the fixing screws (A in Fig. 1.39) to prevent it from freely moving. Once the gun is triggered, the explosive force pushes the piston (C in Fig. 1.39) which strikes the tool holder on the impact pad (E in Fig. 1.39) by means of the impacting head (D in Fig. 1.39); this causes the shear pin breakage and the sudden tool disengagement from the workpiece.

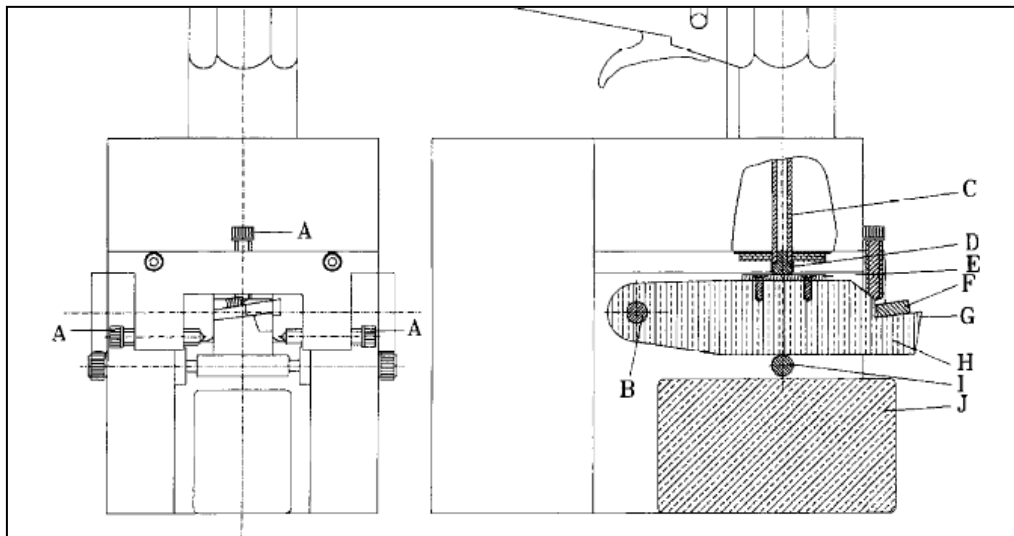


Fig. 1.39: Scheme of the QSD developed by Lin et al. [43].

Lin et al. have carried out no performance measurements of their QSD.

**5) workpiece moving at  $V_c$  → tool acceleration → tool destruction → mechanical impact load**

The quick-stop devices where the tool-workpiece is performed by destroying the tool risk to have a certain variance in results due to the fact that the same tool cannot be used for more than one experiment. Moreover, in this QSDs the tool trajectory during disengagement cannot be controlled and the chip may be damaged.

- Among the others, Giusti's review [29] describes the "Aachen 2" QSD, where the tool separation from the workpiece is performed by removing the tool tip through a blow on the striker (P in Fig. 1.40); the used tool is made up of carbides and has a notch which makes its breakage easier.

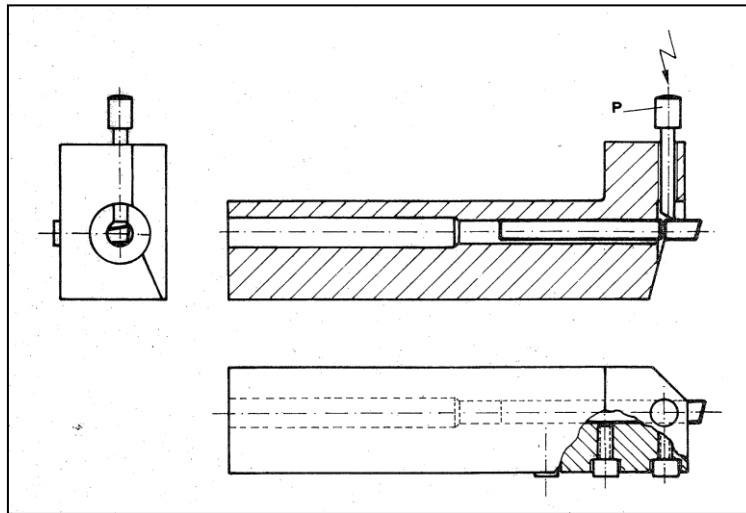


Fig. 1.40: Scheme of the "Aachen 2" QSD described in [29].

**6) workpiece moving at  $V_c$  → tool acceleration → tool destruction → kinetic energy of a mass accelerated by an explosion**

The QSDs in this group have the same problems as the ones in Group 5 but also have some safety risks due to the explosion.

- In the "Aachen 3" device (Fig. 1.41), presented in [29], the cutting action is interrupted by breaking the tool tip thanks to a bullet accelerated by the explosion of a cartridge, which is primed by a hammer blow on a striker.

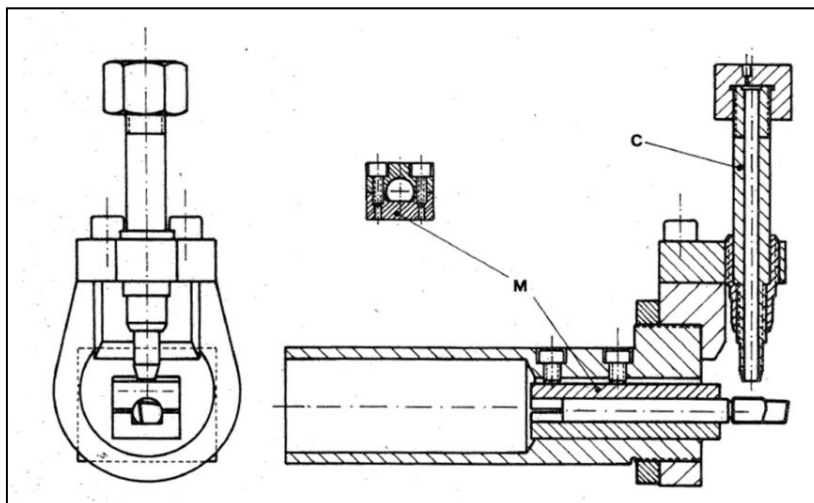


Fig. 1.41: Scheme of the "Aachen 3" QSD described in [29].

- The quick-stop device designed by Giusti et al. [41] to be used for cutting speeds up to 1000 m/min again uses the energy of a mass (a bullet) accelerated by an explosion (which is primed by a striker, 1 in Fig. 1.42 a, and takes place inside a combustion chamber, 2 in Fig. 1.42 a) to destroy the tool (5 in Fig. 1.42 a).

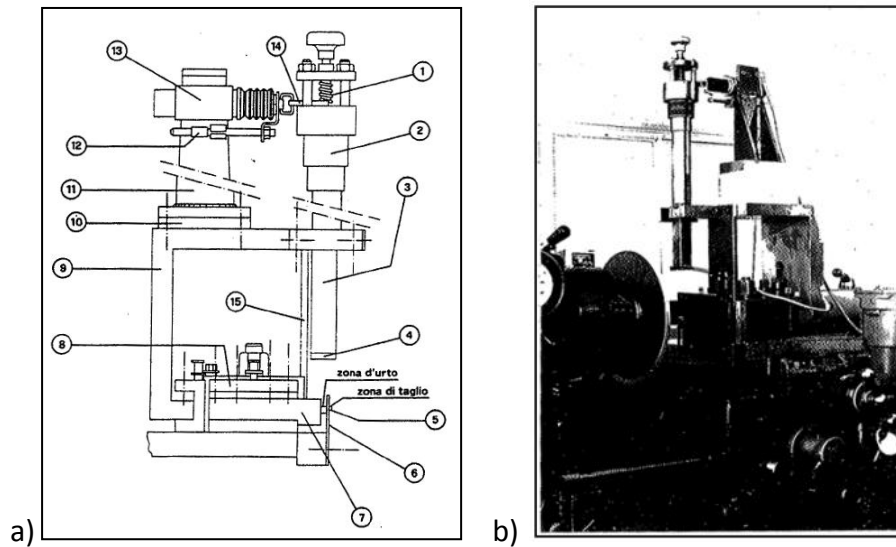


Fig. 1.42: a) Scheme and b) picture of the QSD developed by Giusti [41].

For each quick-stop test, the time needed to interrupt the tool-workpiece interaction (i.e. the separation time  $t_s$ ) is obtained as the sum of two quantities:

- the tool breakage duration, which has been measured before the quick-stop experiments thanks to an optical sensor and is equal to  $0.8 \mu\text{s}$  (after this interval the tool fragments has a speed of almost 12 m/s);
- the time necessary to accelerate the tool up to the cutting speed, which is calculated basing on the pin shear stress (determined in preliminary experiments), the cutting speed and the tool fragments mass.

Results for some tests are reported in Tab. 1.4.

The described performance measurement method allows to evaluate the separation time  $t_s$  for each tests but does not obtain it directly on signals acquired during experiments, as it is for the micro QSD developed in the present study (see Section 4.4).

**7) workpiece moving at  $V_c \rightarrow$  workpiece deceleration  $\rightarrow$  mechanical load**

The drawback of the QSDs in this Group is that some forces risk to be transmitted to the machine spindle.

- The “Delft 1” QSD shown in Giusti’s review [29] exploits a mechanical load to stop the chip formation decelerating the workpiece.

This device is composed of a coupling (M in Fig. 1.43) fixed between lathe spindle and tailstock; the ring-shaped workpiece (P in Fig. 1.43) is mounted on a ring (A in Fig. 1.43) which has a projection and is fastened to the coupling by means of four pins (Z in Fig. 1.43). When the cutting action should be stopped, a bar (K in Fig. 1.43) pushed by a spring (M in Fig. 1.43) moves forward and, when it hits the ring projection, the pins break and the workpiece stops rotating.

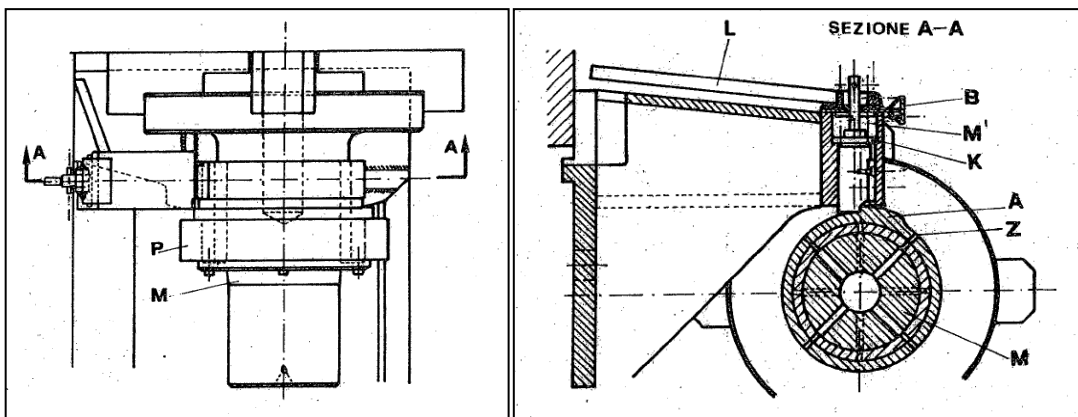


Fig. 1.43: Scheme of the “Delft 1” QSD described in [29].

- The “Pisa 1” quick-stop device presented in [29] again uses a mechanical load to stop the workpiece but it realized exploiting the lathe steady rest, one of whose supports is substituted by the stopping stud (C in Fig. 1.44). The workpiece is fixed inside a ring (M in Fig. 1.44) which acts like a carrier and has a notch (G in Fig. 1.44); when the stud is moved forward by the spring (H in Fig. 1.44) and comes in contact with the notch, the cutting action is stopped due to the breakage of the notched drive pin (Q in Fig. 1.44).



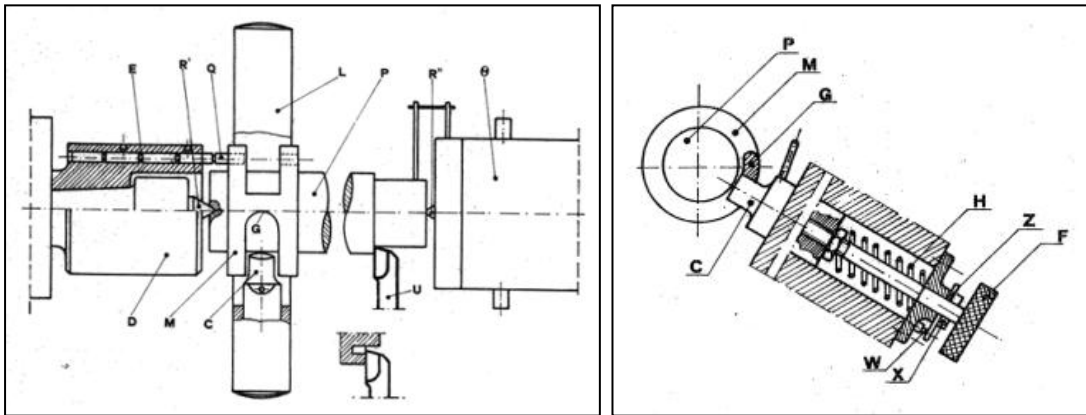


Fig. 1.44: Scheme of the "Pisa 1" QSD described in [29].

**8) workpiece moving at  $V_c$  → workpiece deceleration → explosive pressure of gases**

As in the previous Group, some forces risk to be transmitted to the machine spindle and, moreover, the explosion introduces some safety risks.

- The "Pisa 2" QSD shown in [29] is almost identical to the "Pisa 1" device: only the stopping stud (C in Fig. 1.45) has been modified by introducing a piston (Y in Fig. 1.45) at its end with an explosion chamber (S in Fig. 1.45); this allows to take advantage of the explosive load produced by cartridge when the stud comes in contact with the notch (G in Fig. 1.45) of the ring (M in Fig. 1.45) carrying the workpiece.

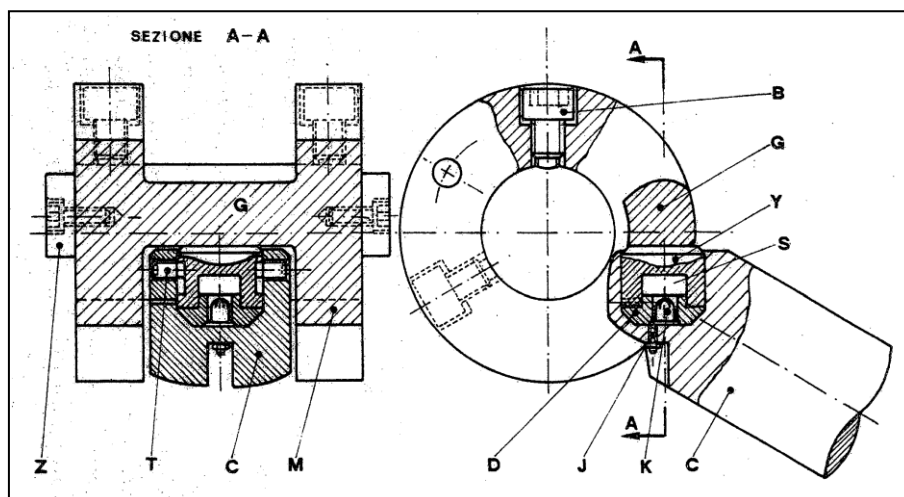


Fig. 1.45: Scheme of the "Pisa 2" QSD described in [29].

9) tool moving at  $V_c$  → workpiece acceleration → quick workpiece dropping → electromagnetic energy

The only quick-stop device belonging to this Group has a lower acceleration than other QSDs, since it exploits electromagnetic energy and cutting force to move the workpiece away from the tool.

- The QSD proposed by Wu et al. [46] is the only one, among those analyzed in this study, which uses an load to stop the cutting action; it has been designed to be used on a shaping machine and disengages the workpiece from the tool by translation (Fig. 1.46).

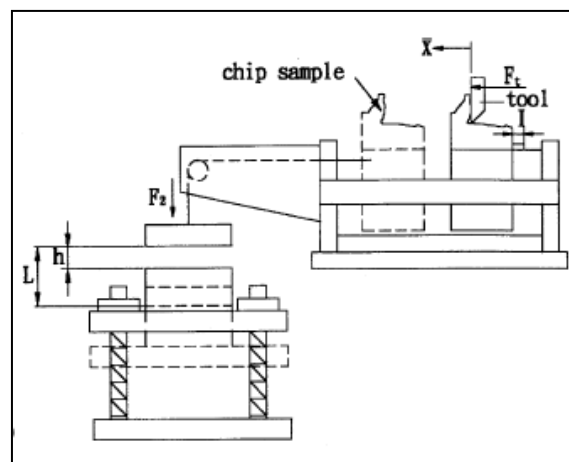


Fig. 1.46: Working principle of the QSD developed by Wu et al. [46].

In this device the workpiece (7 in Fig. 1.47) is fastened on the clamp (9 in Fig. 1.47) which is free to slide along the axis of the guiding pole (4 in Fig. 1.47). If the control electrical circuit is turned on, the electromagnet n°1 (6 in Fig. 1.47) is active and attracts the clamp, as represented in Fig. 1.46 with a solid line. A photoelectricity switch (3 in Fig. 1.47) is able to send a voltage signal to the control circuit as the tool passes by; after it has received this signal for three times, it turns off the electromagnet n°1 and turns on the electromagnet n°2 (19 in Fig. 1.47) which attracts the guiding plate (18 in Fig. 1.47). The plate pulls the clamp through a steel wire (17 in Fig. 1.47) and, as depicted with a dashed line in Fig. 1.46, separates the workpiece from the tool, whose motion is stopped after the control circuit has received a signal from the limit switch (5 in Fig. 1.47).

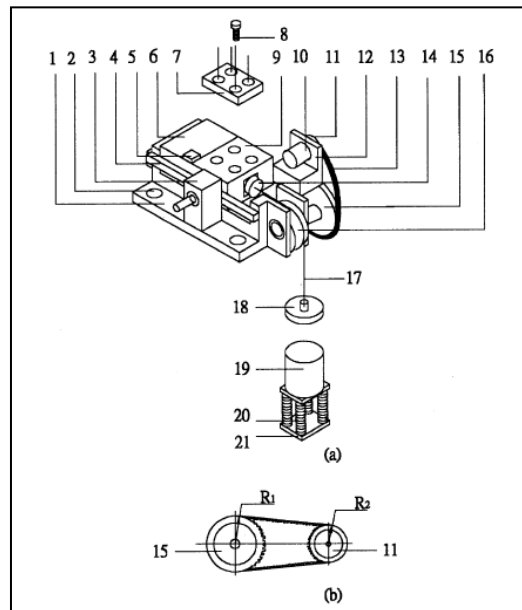


Fig. 1.47: Scheme of the QSD developed by Wu et al. [46].

As shown in Tab 1.4, Wu et al. made some preliminary non-cutting tests in order to define their QSD performance (in terms of separation time  $t_s$  and distance  $d_s$ ) thanks to time-displacement measurements, according to the method (see Fig. 1.36) proposed by Ellis et al. [Ellis] (whose QSD is in Group 4). The tool motion has been derived from encoder measurements. In the quick-stop device, a roller (16 in Fig. 1.47) and a large circular wheel (15 in Fig. 1.47) are secured at two ends along one rotating axis, moreover a small circular wheel (11 in Fig. 1.47) is aligned with the centerline of the encoder (10 in Fig. 1.47); when the workpiece clamp (9 in Fig. 1.47) is pulled away by the steel wire, the roller and the large circular wheel are rotated for a corresponding angular displacement and meanwhile the small circular wheel is also rotated for a corresponding angular displacement, thanks to a timing belt (13 in Fig. 1.47) which transmits the drive. The workpiece displacement can be calculated basing on the small circular wheel angular displacement, taking into account the radii of all wheels.

Wu et al. also performed a theoretical calculation of the separation distance  $d_s$  and stated that performance measurement can be omitted during tests since error between measured and theoretical  $d_s$  is small.

**10) tool moving at  $V_c$  → workpiece acceleration → shear pins breakage → mechanical impact load**

The only drawback of QSDs in this group is that pins have to be carefully designed in order to resist to the cutting forces and to instantaneously break when the mechanical impact load is applied.

- In the QSD designed by Hsu [26] the tool moves at the cutting speed while the workpiece remains still until it is accelerated by an impact load and the cutting action is thus stopped.

The workpiece is fixed on a support (A in Fig. 1.48, where the clamping system is not shown) which is able to slide inside the device base (B in Fig. 1.48). During the orthogonal cutting execution the specimen support is prevented from moving by means of a ring (C in Fig. 1.48) held by shear pins; after the tool has cut about half an inch (= 12.7 mm), the tool holder tongue (D in Fig. 1.48) hits the workpiece support and makes the pins break so the specimen accelerates and separates from the tool.

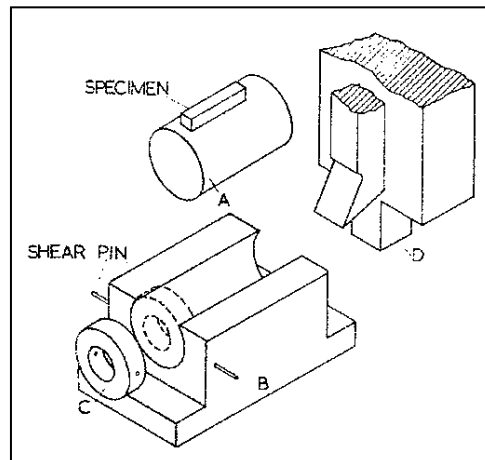


Fig. 1.48: Scheme of the QSD developed by Hsu [Hsu].

Hsu evaluated the performance of his QSD by means of the cutting force measurements made by a dynamometer.

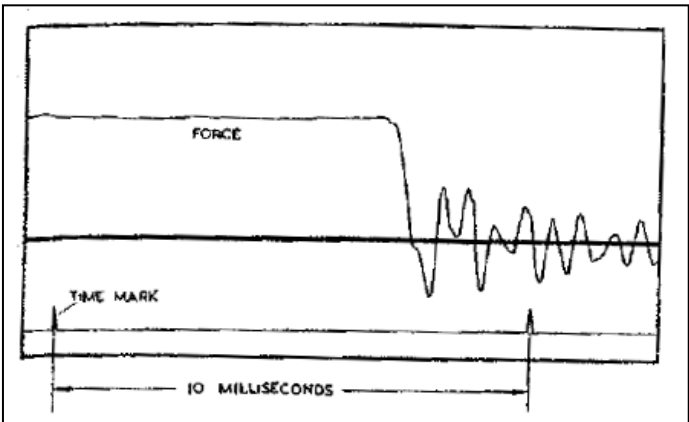


Fig. 1.49: Oscillogram of cutting force acquired during a quick-stop test [26].

In the analyzed test (Fig. 1.49) the force decay, corresponding to the cutting action interruption, has taken place in less than 50  $\mu$ s (see Tab 1.4).

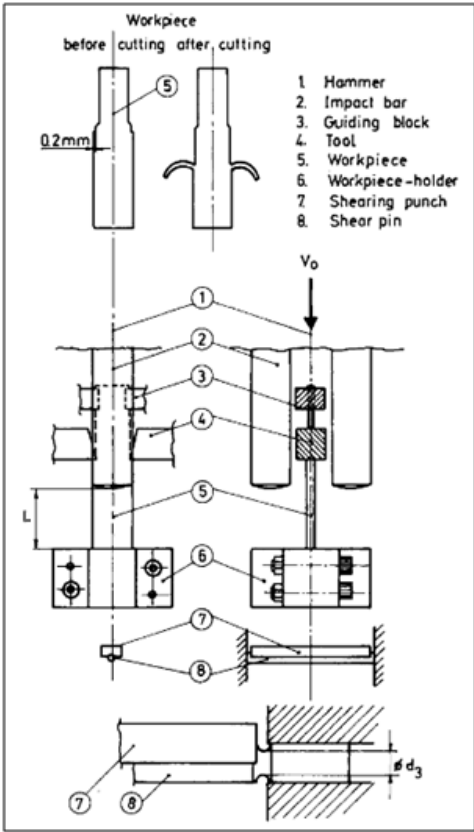


Fig. 1.50: Scheme of the QSD developed by Vorm [37].

- In the QSD designed by Vorm [Vorm], orthogonal cutting is carried out symmetrically on the two sides of a sheet workpiece (5 in Fig 1.50) which is held in position between the cutting tools (4 in Fig 1.50) by means of two guiding blocks (3 in Fig 1.50); the workpiece and its holder (6 in Fig 1.50) are hanging in the guiding blocks during the hammer descent until the workpiece-holder hits the shearing punch (7 in Fig 1.50), the workpiece is stopped and the two cutting processes are carried out with the workpiece sliding in the guiding blocks. After covering the cutting length ( $L$  in Fig 1.50), the impact bars (2 in Fig 1.50) hit the workpiece-holder and thus the shearing punch which breaks the shear pin (8 in Fig 1.50); the workpiece is then accelerated and moves away from the tool, making the cutting process end.

Vorm used a laser transducer for directly measure the time-displacement curve during workpiece acceleration; this way, it has been possible to determine the workpiece equation of motion and then, according to [30], the separation time  $t_s$  has been found as the time when the curve slope equals the cutting speed (see Fig. 1.36).

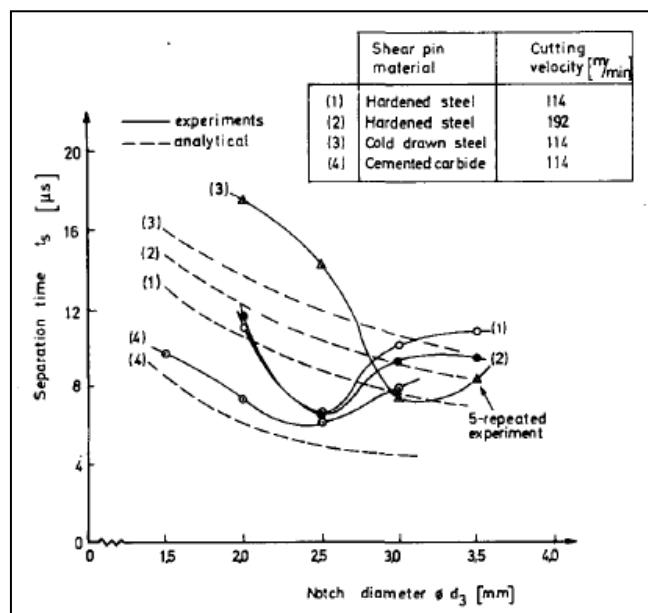


Fig. 1.51: Separation time for different shear pin notch diameters [37].

Fig. 1.51 shows the result of some experiments made for different cutting velocities (which result from the falling height of the hammer) and shear pins materials in order to investigate the influence of the notch diameter on the separation time while Fig. 1.52 depicts the results of a series of experiments made to better analyze the influence of the cutting speed.

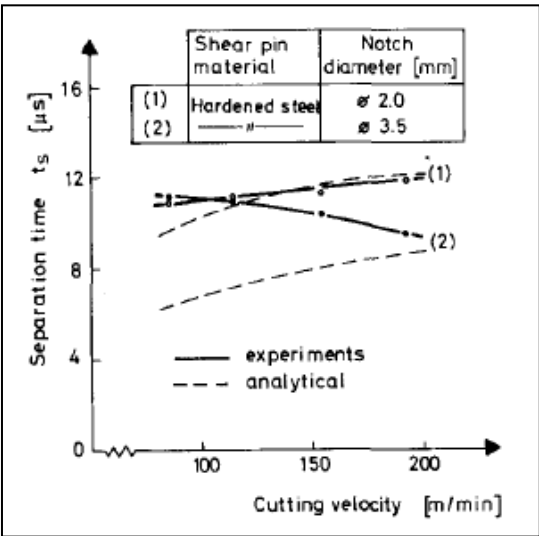


Fig. 1.52: Separation time for different cutting speeds [37].

Table 1.4. Summary of QSDs performance evaluation.

paper	performance measurement method	performance measurement timing	acceleration	separation time $t_s$	separation distance $d_s$	$d_s / t_c$
[25]	performance is not measured	-----	-----	-----	-----	-----
[26]	through cutting forces acquired by means of a dynamometer	not specified; only the result of one test is shown	-----	< 50 $\mu$ s	-----	-----
[27]	high speed camera with acquisition frequency of 3000 frames/s (only the first 12.7 mm of movement have been recorded)	not specified; only the result of one test is shown	$1.5 \cdot 10^6 \text{ m/s}^2$	3.3 $\mu$ s ( $V_c = 5.1 \text{ m/s}$ )	7.62 $\mu$ m ( $V_c = 5.1 \text{ m/s}$ )	-----
	capacitive sensor (only the first 0.254 mm of movement are considered)		$1.01 \cdot 10^7 \text{ m/s}^2$ ( $V_c = 5.1 \text{ m/s}$ )	0.5 $\mu$ s ( $V_c = 5.1 \text{ m/s}$ )	1.27 $\mu$ m ( $V_c = 5.1 \text{ m/s}$ ) calculated basing on measured acceleration	$t_c = 0.04318 \text{ mm}$ $d_s / t_c = 0.03$
			$1.01 \cdot 10^7 \text{ m/s}^2$ ( $V_c = 20.3 \text{ m/s}$ )	-----	20.3 $\mu$ m ( $V_c = 5.1 \text{ m/s}$ )	$t_c = 0.04318 \text{ mm}$ $d_s / t_c = 0.47$



paper	performance measurement method	performance measurement timing	acceleration	separation time $t_s$	separation distance $d_s$	$d_s / t_c$
[28]	performance is not measured	-----	-----	-----	-----	-----
[29] all devices	performance is not measured	-----	-----	-----	-----	-----
[30]	capacitive sensor	not specified; only the result of some preliminary tests (with and without cutting action) is shown	$1.3 \cdot 10^5 \text{ m/s}^2$ $1.65 \cdot 10^5 \text{ m/s}^2$ not uniform	31 $\mu\text{s}$ ( $V_c = 5.1 \text{ m/s}$ )	63.5 $\mu\text{m}$ ( $V_c = 5.1 \text{ m/s}$ )	-----
[31]	high-speed camera (only the first 2.54 mm of movement have been recorded)	not specified; only the result of one test is shown	$3.3 \cdot 10^5 \text{ m/s}^2$	15.2 $\mu\text{s}$ ( $V_c = 5.1 \text{ m/s}$ )	101.6 $\mu\text{m}$ ( $V_c = 5.1 \text{ m/s}$ )	$d_s / t_c = 0.15$

paper	performance measurement method	performance measurement timing	acceleration	separation time $t_s$	separation distance $d_s$	$d_s / t_c$
[32]	wire strain gauge (acceleration has been measured during the first 0.0308 mm of movement)	not specified	$2.5 \cdot 10^5 \text{ m/s}^2$	20 $\mu\text{s}$ ( $V_c = 5.1 \text{ m/s}$ )	50.8 $\mu\text{m}$ ( $V_c = 5.1 \text{ m/s}$ )	-----
[33]	high speed camera with acquisition frequency of 3000 frames/s	not specified; only the result of some tests is shown	$1.8 \cdot 10^4 \text{ m/s}^2$ ( <b>non-preloaded shear pin</b> , after 1/300 s)	2.25 ms ( $V_c = 1.67 \text{ m/s}$ )	1.75 mm ( $V_c = 1.67 \text{ m/s}$ )	$t_c = 0.15 \text{ mm}$ $d_s / t_c = 11.7$
			$1.8 \cdot 10^4 \text{ m/s}^2$ ( <b>preloaded shear pin</b> , after 1/500 s)	18.5 $\mu\text{s}$ ( $V_c = 1.67 \text{ m/s}$ )	15.4 $\mu\text{m}$ ( $V_c = 1.67 \text{ m/s}$ )	$t_c = 0.15 \text{ mm}$ $d_s / t_c = 0.1$
[34] [35]	pressure transducer + fotonic sensor	not specified	$7.1 \cdot 10^4 \text{ m/s}^2$	200 $\mu\text{s}$ ( $V_c = 5.1 \text{ m/s}$ )	330.2 $\mu\text{m}$ ( $V_c = 5.1 \text{ m/s}$ )	-----

paper	performance measurement method	performance measurement timing	acceleration	separation time $t_s$	separation distance $d_s$	$d_s / t_c$
[37]	laser transducer with an acquisition frequency of 5 MHz	not specified; only some results are shown	-----	6-18 $\mu$ s ( $V_c = 1.9$ - $3.2$ m/s, pin notch diameter = 2-3.5 mm) (Fig. 1.51)	-----	-----
			-----	8-12 $\mu$ s ( $V_c = 1.7$ - $3.3$ m/s, pin notch diameter = 2-3.5 mm) (Fig. 1.52)	-----	-----
[38]	pressure transducer + fotonic sensor	not specified; only the result of some preliminary tests (with cutting action) is shown	$\approx 2.5 \cdot 10^5$ m/s <sup>2</sup>	< 10 $\mu$ s ( $V_c = 5.1$ m/s)	330.2 $\mu$ m ( $V_c = 5.1$ m/s)	-----
[39]	high speed camera with an acquisition frequency of 4000 frames/s	not specified; only the result of one test (with cutting action) is shown	$\approx 10^8$ m/s <sup>2</sup> ( $V_c = 20.32$ m/s)	-----	-----	-----

paper	performance measurement method	performance measurement timing	acceleration	separation time $t_s$	separation distance $d_s$	$d_s / t_c$
[40]	capacitive sensor	not specified; only the result of one test is shown	$3.3 \cdot 10^5 \text{ m/s}^2$	15 $\mu\text{s}$ ( $V_c = 5.1 \text{ m/s}$ )	43.2 $\mu\text{m}$ ( $V_c = 5.1 \text{ m/s}$ )	$d_s / t_c = 0.022$ ( $V_c = 1.3 \text{ m/s}$ )
[41]	optical measures by means of a beam focalized on the tool cutting edge + calculation based on shear stress, cutting speed and mass of tool mass of tool fragments	not specified; only the result of some tests (without cutting action) is shown	-----	1.8 $\mu\text{s}$ ( <b>C40 steel</b> , $V_c = 900 \text{ m/min}$ )	8.7 $\mu\text{m}$ ( <b>C40 steel</b> , $V_c = 900 \text{ m/min}$ )	$t_c = 0.16 \text{ mm}$ $d_s / t_c = 0.05$
			-----	4.4 $\mu\text{s}$ ( <b>OT67 brass</b> , $V_c = 1200 \text{ m/min}$ )	26 $\mu\text{m}$ ( <b>OT67 brass</b> , $V_c = 1200 \text{ m/min}$ )	$t_c = 0.20 \text{ mm}$ $d_s / t_c = 0.13$
			-----	7.5 $\mu\text{s}$ ( <b>Avional 2024</b> , $V_c = 1200 \text{ m/min}$ )	38 $\mu\text{m}$ ( <b>Avional 2024</b> , $V_c = 1200 \text{ m/min}$ )	$t_c = 0.20 \text{ mm}$ $d_s / t_c = 0.19$
			-----	13 $\mu\text{s}$ ( <b>Avional 2024</b> , $V_c = 1600 \text{ m/min}$ )	106 $\mu\text{m}$ ( <b>Avional 2024</b> , $V_c = 1600 \text{ m/min}$ )	$t_c = 0.20 \text{ mm}$ $d_s / t_c = 0.53$
			-----	18.5 $\mu\text{s}$ ( <b>Avional 2024</b> , $V_c = 2000 \text{ m/min}$ )	211 $\mu\text{m}$ ( <b>Avional 2024</b> , $V_c = 2000 \text{ m/min}$ )	$t_c = 0.20 \text{ mm}$ $d_s / t_c = 1.05$
[42]	performance is not measured	-----	-----	-----	-----	-----

paper	performance measurement method	performance measurement timing	acceleration	separation time $t_s$	separation distance $d_s$	$d_s / t_c$
[43]	performance is not measured	-----	-----	-----	-----	-----
[44] [47] [48]	not specified	-----	$1.65 \pm 0.15 \cdot 10^3$ m/s <sup>2</sup>	-----	-----	-----
[45]	performance is not measured	-----	-----	-----	-----	-----
[46]	rotary encoder	not specified (it is said that performance measurement can be omitted during tests since error between measured and theoretical $d_s$ is small)	-----	120 $\mu$ s (theoretical = 116 $\mu$ s, <b>6061 aluminum</b> , $V_c = 5.1$ m/s)	0.3 mm (theoretical = 0.29 mm, <b>6061 aluminum</b> , $V_c = 5.1$ m/s)	-----

paper	performance measurement method	performance measurement timing	acceleration	separation time $t_s$	separation distance $d_s$	$d_s / t_c$
[50]	performance is not measured	-----	-----	-----	-----	-----
Spaans in [38]	high speed camera with an acquisition frequency of 40000 frames/s	-----	$7.1 \cdot 10^5 \text{ m/s}^2$	$7 \mu\text{s}$ ( $V_c = 5.1 \text{ m/s}$ )	$17.78 \mu\text{m}$ ( $V_c = 5.1 \text{ m/s}$ )	-----

### 1.3 Objectives

For the reason outlined in Section 1.1, the main objective of this study is to design a new quick-stop device (QSD) to carry out frozen cut experiments within the typical microscale cutting requirements (i.e. cutting speed lower than 200 m/min and chip thickness between less than 1  $\mu\text{m}$  and 100  $\mu\text{m}$ ); this new device should overcome the drawbacks of the existing QSDs (discussed in Section 1.2.1 and 1.2.3), have a good repeatability and fulfil safety requirements.

Moreover, the literature survey points out how the new QSD should be characterized in terms of performance in order to validate each quick-stop experiment. Hence, in the present work *ad hoc* sensors and procedures have to be developed in order to calculate the performance indexes previously discussed in Section 1.2.2.





## Chapter 2

### Equipment

Since the aim of the present work is to study the chip formation in the microscale, it has been decided to perform the quick stop experiments on the KERN Evo 5-axis CNC high precision machining centre, which is available at the “MI\_crolab” within the Manufacturing and Production System laboratory of Department of Mechanics of Politecnico di Milano (this choice has been done in order to exploit the high precision of the machine).

In order to acquire cutting forces signals during the tests, a triaxial piezoelectric load cell has been used (placed under the QSD tool holder block), together with a data acquisition device, which is mounted on a PC and controlled through LabVIEW® programs.

The quick stop experiments are triggered by means of an electronic control system based on the signal acquired by a USB data acquisition device and coordinated by a LabVIEW® program.

Signals coming from the angular position sensors, which are used in the micro QSD performance measurement, are acquired thanks to a digital oscilloscope.

#### 2.1 Machining centre

The KERN Evo [51] (Fig 2.1) is a specific machining centre for micromachining since it has a high speed spindle (revolution speed from 500 to 50'000 rpm and a maximum power of 6.4 kW) with a rotational accuracy (“run out”) lower than 1  $\mu\text{m}$ . It guarantees high precision (Tab 2.1 and Tab 2.2) and provides an excellent surface finish ( $R_a \leq 0.1 \mu\text{m}$ ). The polymer concrete monobloc machine frame optimally damps vibrations and therefore the machine can reach high acceleration rates (up to 8  $\text{m/s}^2$ ) and high feed rates (between 0.01 and 16'000 mm/min), without compromising the machining quality.

Entering into details of machine characteristics, high precision prismatic linear guides, which are roller seated and backlash-free pre-stressed, ensure stability in positioning accuracies. Reaching high acceleration and feed rates is allowed by digital direct axes drives, which optimize contour tracing on dynamic machining; moreover jamming of the axes is avoided thanks to the central alignment of the major drive and command elements. High precision ball screw

actuators are used into the axes centre next to the Heidenhain incremental glass scales, with a resolution of  $0.1 \mu\text{m}$ .

The polymer concrete machine frame ensures both static and dynamic stiffness which are much higher than traditional cast iron structures (thanks to its big cross sections) and damps vibrations 10 times more, resulting in up to 30% higher tools life and a surface finish  $0.1 \mu\text{m} R_a$ . Moreover, the polymer concrete has a heat conductivity 50 % lower than steel or cast iron, so it doesn't react to temperature fluctuations and minimizes the deformation due to temperature variations, increasing the workpiece accuracy.

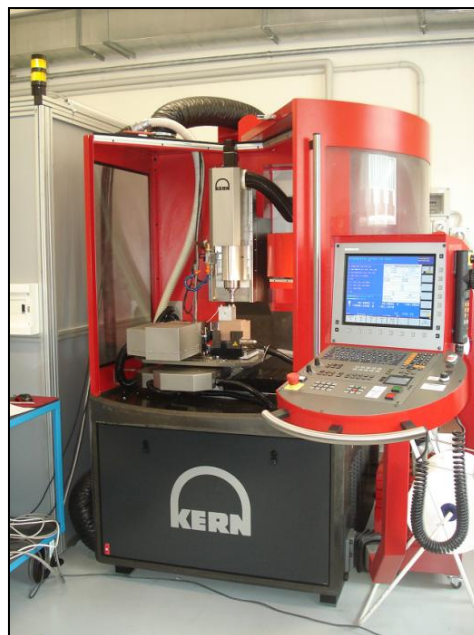


Figure 2.1. Overview of KERN Evo machining centre.

The following tables show the machining centre specifications (note that all quantities are defined according to VDI/DGQ 3441 standard [52]).

Table 2.1. KERN Evo specifications, relating to X, Y and Z axes.

quantity	value
resolution	$0.1 \mu\text{m}$
positioning tolerance $P$	$\pm 1 \mu\text{m}$
positioning scatter $P_s$	$\pm 0.5 \mu\text{m}$
precision on the workpiece	$\pm 2 \mu\text{m}$

Table 2.2. KERN Evo specifications, relating to B and C axes.

quantity	value
positioning scatter $P_s$	$\leq 1''$
precision on the workpiece	$\leq 5''$

The KERN Evo machining centre is controlled by a Heidenhain numerical contouring control system, which allows to use both ISO and a more user-friendly Heidenhain programming language; moreover it contains several fixed cycles for milling and drilling, it is able to perform up to 5 axes interpolation and tool radius correction for 5-axis simultaneous operations and it manages the automatic tool changer.

The machine is equipped with a laser presetting system (Fig. 2.2): it is a tool measurement device which is positioned on the machine table and is equipped with a 30  $\mu\text{m}$  diameter laser beam. This system permits the non-contact measurement of several tool characteristics (such as length and radius, but also profile and integrity of cutting edges) and automatically sends the obtained data to the numerical control. According to its datasheet [53], the laser presetting system has an accuracy of 1  $\mu\text{m}$ .



Figure 2.2. Laser presetting system during the measurement of a mill.

The KERN Evo machining centre is also equipped with a touch probe device (Fig. 2.3) with a wireless infrared data transmission system, which can automatically transfer the height and position of the workpiece to the CNC.

According to its datasheet, the touch probe has a unidirectional repeatability of  $\pm 1 \mu\text{m}$  in case it mounts a stylus with a 50 mm diameter sphere.

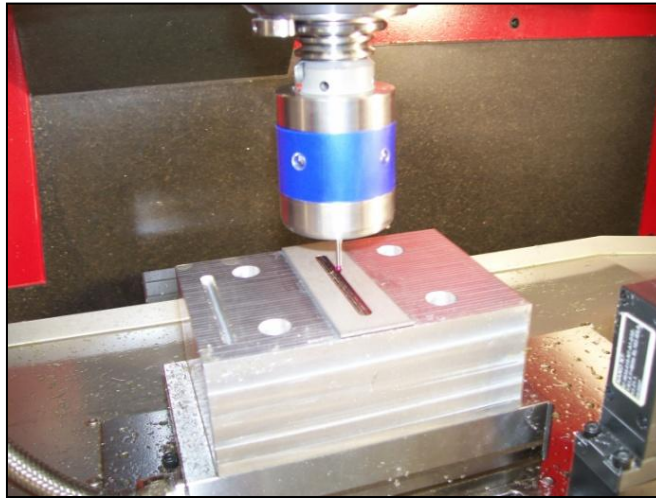


Figure 2.3. Touch probe system during the measurement of the upper surface of a workpiece.

## 2.2 Forces measurement system

The system used for measuring the cutting forces during the experiments is made up by a triaxial load cell, a data acquisition system, which receives the signals sent by the dynamometer, and a connecting unit placed between them. The LabVIEW® program which acquires the cutting force signals is shown in detail in Appendix B.

### 2.2.1 Triaxial load cell

The load cell used for acquiring the force signals is the Kistler 9257BA [54] (Fig. 2.4), which is able to measure three force components along the orthogonal X, Y and Z directions.

The dynamometer is composed by four three-components piezoelectric force sensors fitted under high preload between a base plate and a cover plate, thus the force components are measured practically without displacement. Moreover, the four sensors are ground-isolated and this almost excludes ground loop problems. Finally, the load cell is largely insensitive to temperature influence since its cover plate has a special thermal insulation layer.

A 3-channel charge amplifier is embedded into the dynamometer and thus the output signal has a low impedance.



Figure 2.4. Triaxial load cell.

The load cell is controlled by the Kistler 5233A1 unit [54] (Fig. 2.5), which allows to select the measuring range of forces in X and Y directions and in Z direction separately.



Figure 2.5. Load cell control unit.

**2.2.2 Data acquisition device**

The data acquisition device (DAQ) used for acquiring signals from the dynamometer is the National Instrument PCI-6034E (Fig. 2.6), embedded into a personal computer.



Figure 2.6. PC embedded data acquisition system.

According to its datasheet [55], this DAQ has sixteen multiplexed analog input channels (which means sixteen single-ended or eight differential channels) with 16-bit resolution and a maximum sampling frequency of 200 kS/s; it has also eight digital I/O channels and two 24-bit counters.

Before arriving to the data acquisition device, signals are conditioned by means of the I/O connector block National Instrument SCB-68 [56] (Fig. 2.7); this shielded block, combined with shielded cables, provides very low-noise signals.



Figure 2.7. I/O connector block.

## 2.3 Data acquisition device used in the QSD controlling and synchronizing system

The quick stop experiments are managed by a purpose-built electronic system (see Section 3.2.3) which receives signals from a USB data acquisition device and sends the trigger signal to the QSD. That electronic device is controlled by a LabVIEW® program (whose details are shown in Appendix C) which synchronizes the subsequent test phases.



Figure 2.8. USB data acquisition system.

The data acquisition device used for the QSD controlling and synchronizing system is the National Instrument UBS-6210, which, according to its datasheet [57], has four digital I/O channels and sixteen multiplexed analog input channels with 16-bit resolution and a maximum sampling frequency of 250 kS/s.

## 2.4 Oscilloscope

The digital oscilloscope used for acquiring the voltage signals coming from the angular position sensors (see Section 4.4.1) is the Tektronix TDS1012B [58].

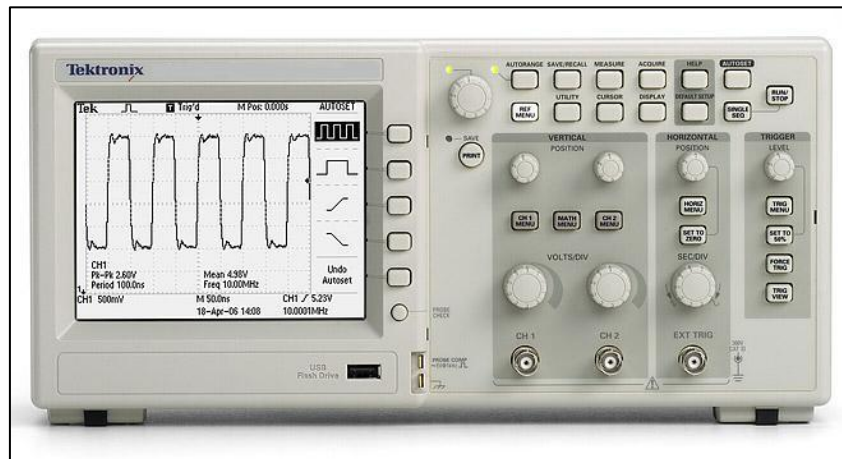


Figure 2.9. Digital oscilloscope.

This oscilloscope has two channels with a maximum sampling rate of 1 GS/s on each of them (the possible time bases are between 5 ns/div to 50 s/div) and 8-bit vertical resolution; moreover, the device can acquire maximum 2500 points at all time bases. If an external trigger is not used, a trigger can be set up on one channel basing on rising / falling edges or pulses.



## Chapter 3

### Micro QSD design

The so called “micro quick-stop device” object of this study (briefly described in [59-61] and more extensively in [62]) has been designed to be used in the range of the typical microscale cutting parameters, which means cutting speed lower than 200 m/min and chip thickness between less than 1  $\mu\text{m}$  and 100  $\mu\text{m}$ . The micro QSD has been especially designed to be mounted on the Kern EVO 5-axis machining centre available at the “MI\_crolab” within the Manufacturing and Production System laboratory of Department of Mechanics of Politecnico di Milano, in order to exploit its high precision to properly investigate the chip formation in the microscale.

#### 3.1 Micro QSD requirements

Since the aim of the present work is to develop and characterize a device which allows to study the chip formation in the microscale, it has been decided to investigate the simplest cutting condition, i.e. orthogonal cutting (Fig. 3.1). This condition is defined as the one where the cutting speed  $V_c$  is perpendicular to the cutting edge and the cutting process can be analyzed as bidimensional, since all quantities (such as speeds and forces) lie on a plane.

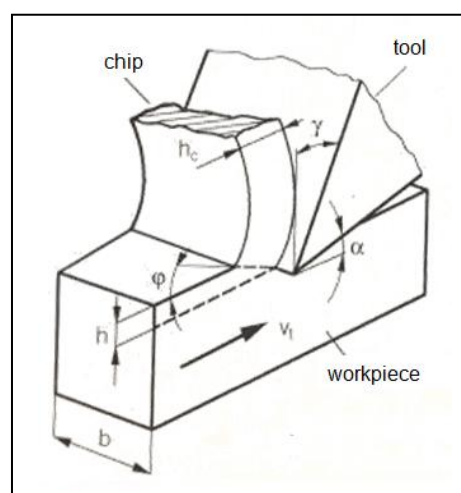


Figure 3.1. Orthogonal cutting.

In order to approximate the orthogonal cutting condition, it has been decided to perform a tube turning operation on the chosen machining centre, as shown in Fig 3.2. This layout reproduces well the orthogonal cutting if the tube diameter is large enough and the wall thickness is sufficiently small to make the difference in speed between the inner and the outer tube face negligible.

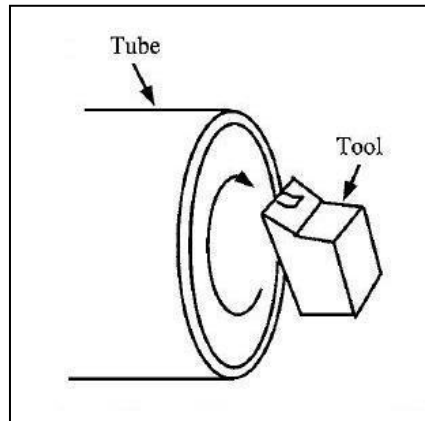


Figure 3.2. Tube orthogonal cutting [47].

This operation can be done thanks to a thin-walled tubular workpiece (external diameter = 11 mm, wall thickness = 0.5 mm) mounted on the machine spindle and a tool holder placed on the machine table, as depicted in the scheme of Fig. 3.3.

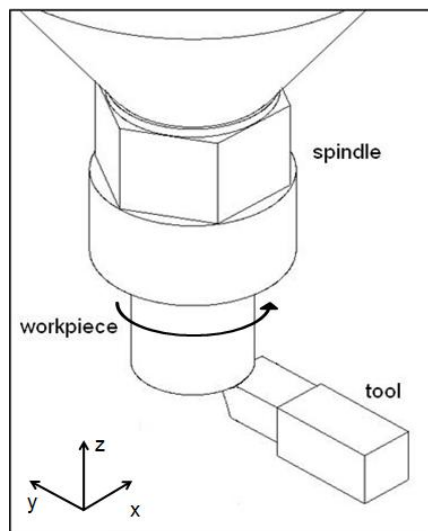


Figure 3.3. Orthogonal cutting operation on the machining centre.

This solution has been chosen instead of turning a disc-shaped workpiece (Fig. 3.4), because in this case more vibrations arise during the cutting operation and, moreover, it is necessary to set a system to continuously change the spindle revolution speed in order to keep the cutting speed constant while the workpiece diameter is reducing. Such a system would not guarantee a smooth motion.

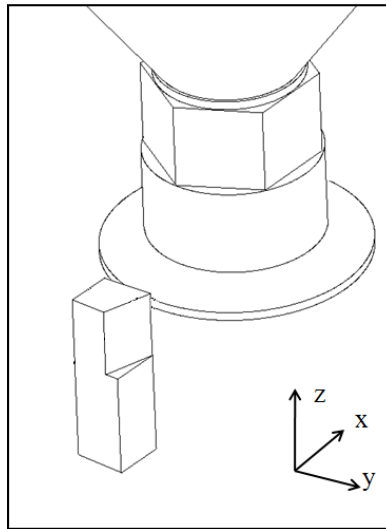


Figure 3.4. Disc orthogonal cutting.

The chosen turning layout implies that the cutting action cannot be interrupted by stopping the workpiece or moving it apart from the tool, otherwise some impulsive forces could be transmitted to the machine spindle and damage it; therefore the cutting process should be interrupted by abruptly moving the tool apart from the workpiece (see Section 1.2.1).

During turning operations, the tool is held in its working position by means of a pin, whose breakage allows the tool holder rotation and the tool-workpiece separation. Since cutting forces are low in micromachining, pins can be made up by glass (Fig. 3.5) because this material has a quite high tensile strength and is able to make the tool holder system stiff enough during the cutting steady phase, but it is also fragile when subject to an impulsive load allowing the tool holder to quickly separate the tool from the workpiece without absorbing much energy.

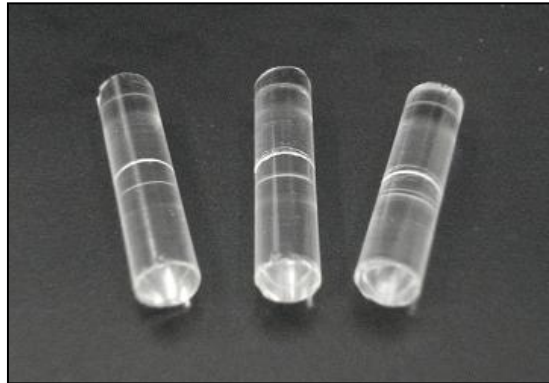


Figure 3.5. Glass shear pins.

In order to allow the device to reach high accelerations while moving the tool apart from the workpiece and, in the meantime, to fulfill the safety rules, it has been decided to make the tool holder move by means of an impulsive load applied by a striker powered by the energy of pressurized air.

To summarize the device design, referring to the QSDs classification presented in Section 1.2.1 (see Fig 1.13), the developed micro QSD presents the following characteristics:

- the object moving at the cutting speed  $V_c$  is the workpiece;
- the tool-workpiece separation is performed thanks to the tool acceleration from  $V_t = 0$  to  $V_t = V_c$  (Fig. 3.6);
- the tool acceleration is allowed by the breakage of specifically designed shear pins;
- the pin breakage is due to a mechanical impact load.

### 3.2 Micro QSD layout

The micro QSD designed in the present study according to the above discussed choices, is composed by two main parts which can be seen in the device layout of Fig 3.6. The two fundamental components of the device are the tool holder block (on the right of Fig 3.6) and the percussion system (on the left of Fig 3.6).

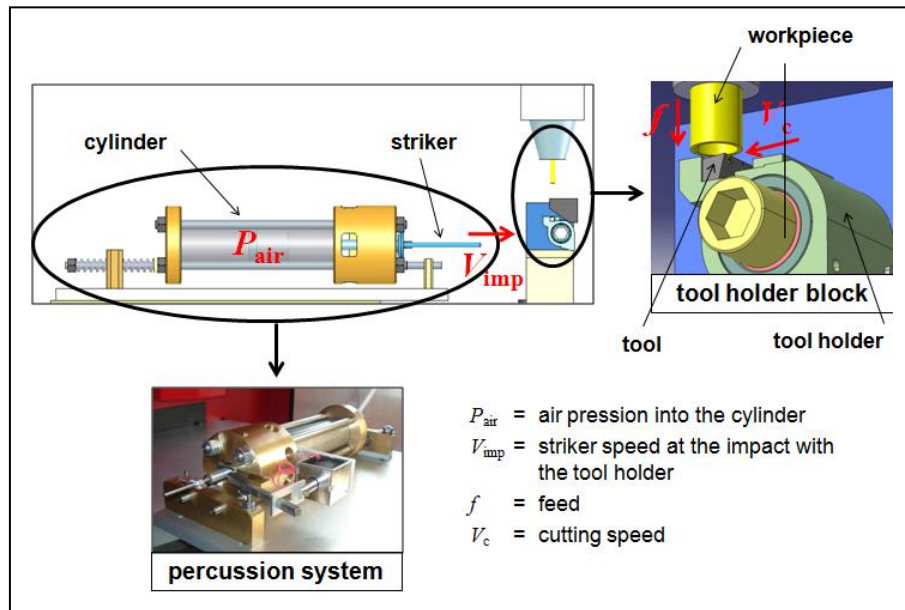


Figure 3.6. Scheme of the micro QSD layout.

The tool holder block (A in Fig. 3.7) is fixed to the machine table through a resin block in order to damp the vibrations caused by the impact between the striker and the tool holder. The percussion system (B in Fig. 3.7) is powered by compressed air and is mounted on the machine rigid frame by means of an aluminum support which is not in contact with the tool holder block in order to avoid transmission of forces.

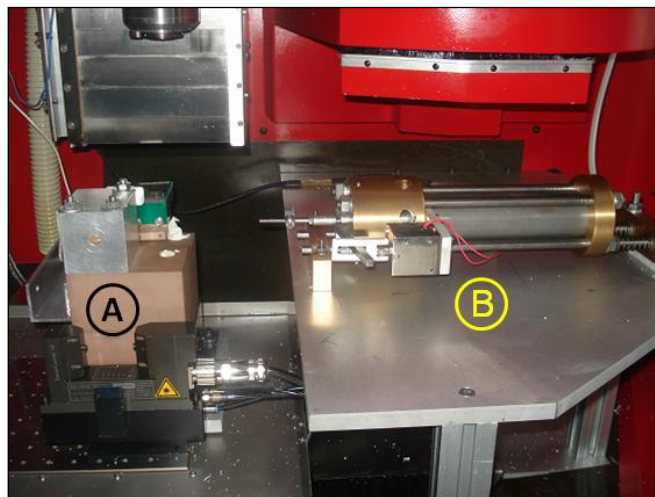


Figure 3.7. Overview of the micro QSD placed in the Kern EVO machining centre [A = tool holder block, B = percussion system] .

### 3.2.1 Tool holder block

The tool holder block consists of a stationary part (D in Fig. 3.8) and a rotating part (C in Fig. 3.8) whose rotation allows the tool motion from the cutting area and thus its separation from the workpiece.

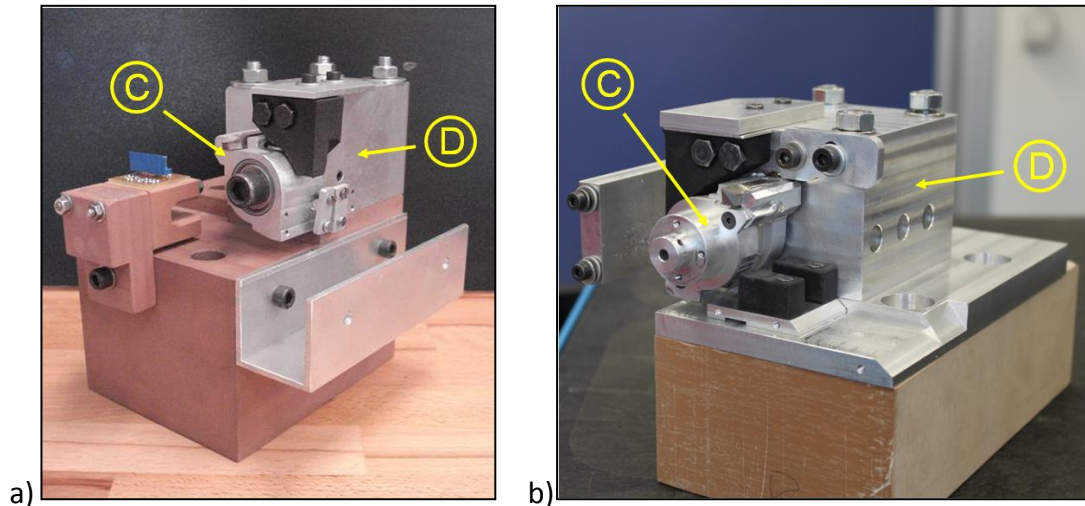


Figure 3.8. a) First and b) second version of the tool holder block [C = rotating part, D = stationary part] .

The tool holder stationary part is composed by an aluminum support (1 in Fig. 3.9) fixed on a resin block; this is screwed on the load cell used for acquiring cutting forces, which is mounted on the machine table. The rotating part (2 in Fig. 3.9) is a purpose-milled aluminum part which holds the turning tool and is hinged on the stationary part.

A second version of the tool holder block (Fig. 3.8 b) has been carried out to improve the first version (Fig. 3.8 a), which does not allow the operator to see the turning operation (see Fig. 3.7 which has been taken from the operator point of view). Thanks to the new version, the quick-stop tests can also be visually controlled during their execution. In any case, in the following all pictures and model will refer to the first version of the tool holder block, since only the position of the tool holder rotating part has changed passing through the first to the second version

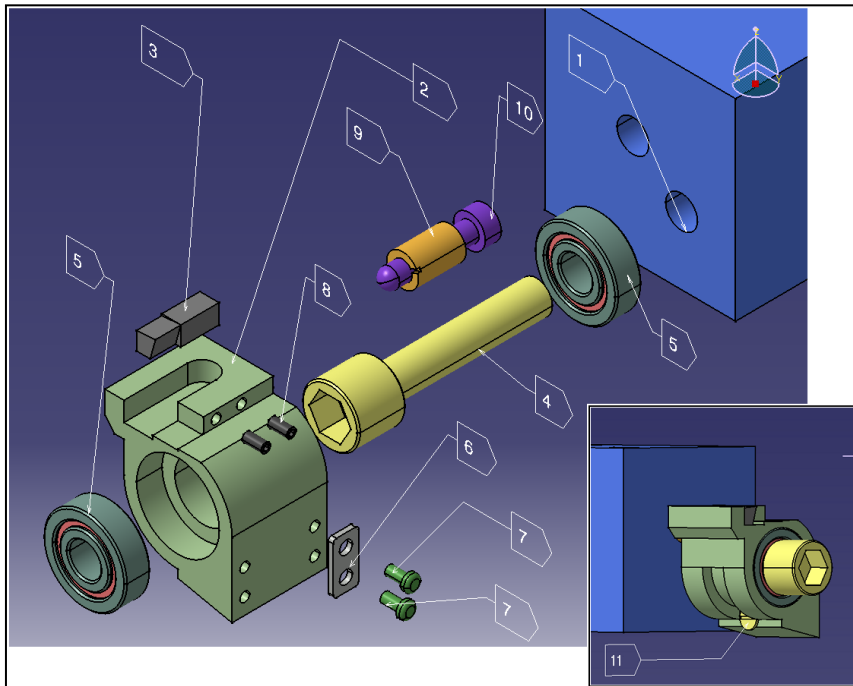


Figure 3.9. Exploded model of the tool holder block.

The exploded model of Fig. 3.9 allows to better detail the tool holder block components, which are:

- (1) aluminum support;
- (2) tool holder rotating part;
- (3) turning tool;
- (4) hinge;
- (5) ball bearings, which should limit the frictional resistance during the tool holder rotation;
- (6) plate, which fixes the glass shear pins between the tool holder fixed and rotating part;
- (7) screws;
- (8) grub screws, which secure the tool in its slot;
- (9) retainer stop;
- (10) rotating part retainer, which should prevent the tool holder rotating part from moving backwards;
- (11) striker target, which is made of hard steel, in order to prevent the striker from damaging the aluminum rotating part.

The tool holder rotating part has been designed in order to reduce the angle the tool should cover to exit from the cutting area determined by the uncut

chip thickness  $t_c$  (hatched in Fig. 3.10) and thus to separate from the workpiece.

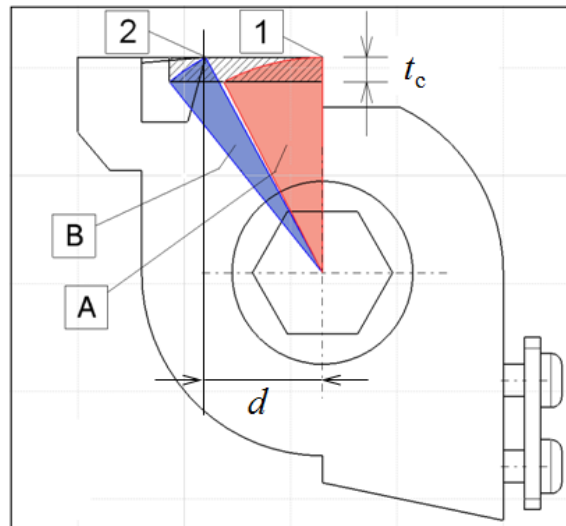


Figure 3.10. Separation angle for different positions of the tool cutting edge.

If the tool cutting edge is vertically aligned with the tool holder hinge (1 in Fig. 3.10) the angle needed for the tool-workpiece separation (A in Fig. 3.10) is larger than in case the cutting edge is further from the vertical axis (2 and B in Fig. 3.10).

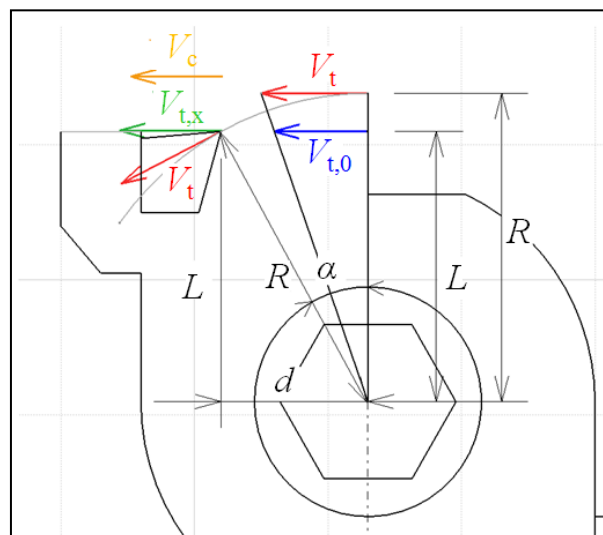


Figure 3.11. Kinematics of the tool holder rotating part.



The above explained solution makes the tool speed ( $V_t$  in Fig. 3.11) increase respect to the case the tool cutting edge has a distance  $L$  from the hinge ( $V_{t,0}$  in Fig. 3.11). In order to determine the completion of tool-workpiece separation, the cutting speed  $V_c$  has not to be compared with the tool holder tangential speed ( $V_t$  in Fig. 3.11) but with its horizontal projection ( $V_{t,x}$  in Fig. 3.11). This issue has already been introduced in Section 1.2.2 about Fig. 1.14 and will be discussed again in Section 4.1.

### 3.2.2 Percussion system

The percussion system is composed by a cylinder (H in Fig. 3.12) where the expansion of pressurized air accelerates a piston which has a striker at its end (E in Fig. 3.12); an electromagnetic solenoid (G in Fig. 3.12) is used to activate the trigger (F in Fig. 3.12) and let the striker move towards the tool holder.

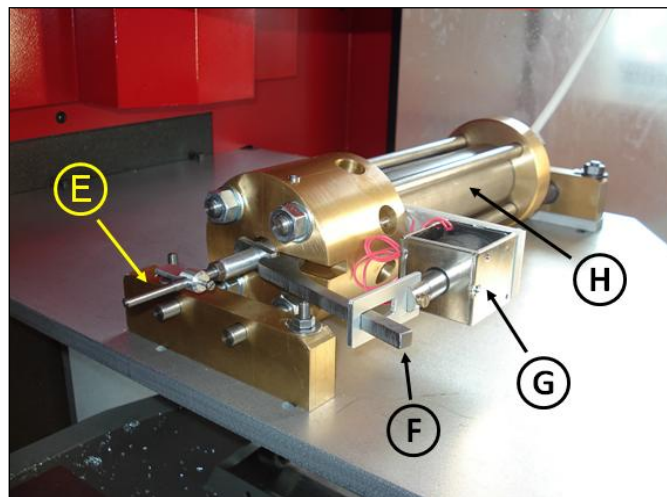


Figure 3.12. Percussion system [E = striker, F = trigger, G = solenoid, H = cylinder] .

The model of Fig. 3.13 allows to better detail the percussion system components, which are:

- (1) brass front cylinder head;
- (2) brass back cylinder head;
- (3) drawn steel cylinder;
- (4) upper threaded tie rods, which only constrain the cylinder heads;
- (5) lower threaded tie rods, which allows the cylinder to translate during the percussion system operation; they are equipped with springs in order to absorb the impact load;
- (6) front support;

- (7) back support;
- (8) striker, which is made of steel in order to better withstand impacts;
- (9) trigger, which allows the piston motion when needed;
- (10) electromagnetic solenoid [63], which activates the trigger when required by the electronic control system;
- (11) slot, which connects the solenoid plunger and the trigger;
- (12) threaded locking ring, which secures the striker to the piston;
- (13) vent holes, which allows the air to exit from the front chamber during the piston motion.

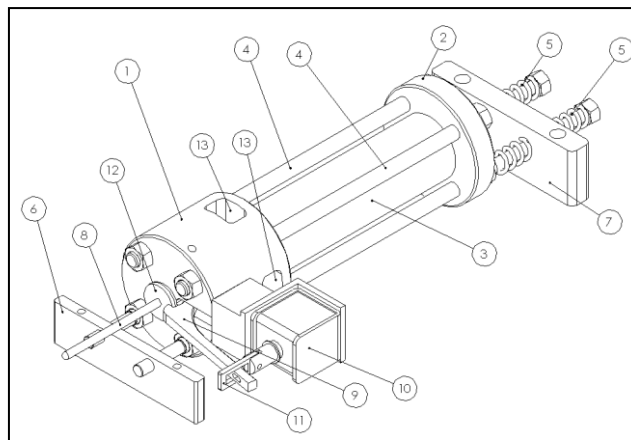


Figure 3.13. Model of the percussion system.

In order to completely describe the percussion system, it is necessary to refer to the cylinder section of Fig. 3.14, where other details can be seen:

- (1) air entrance;
- (2) back chamber, which is pressurized during the system use;
- (3) aluminum piston, whose cup shape has been studied to increase the initial back chamber volume;
- (4) front chamber, which is always at atmospheric pressure;
- (5) rubber pad, which decelerates the piston at the end of its motion;
- (6) vent holes;
- (7) O-ring.

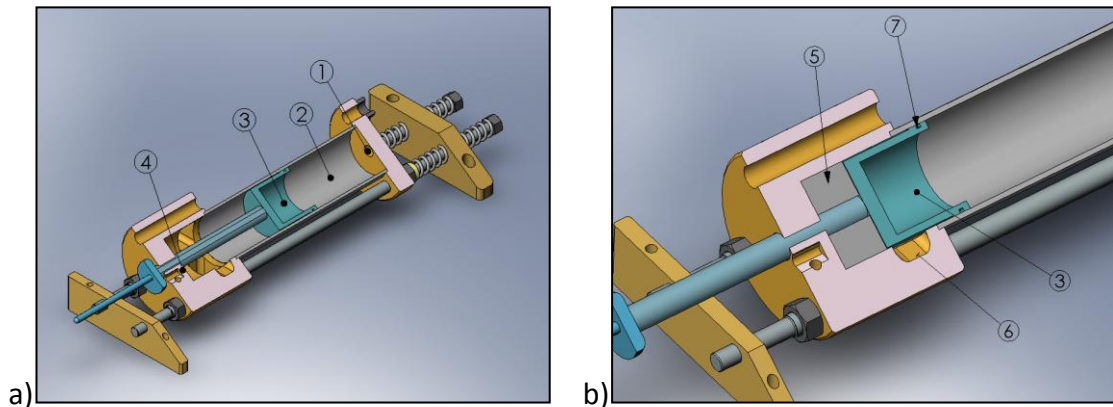


Figure 3.14. Section of percussion system with the piston in its a) initial and b) final position.

The percussion system has been dimensioned thanks to a physical model of the cylinder implemented in a Matlab® program (details in Appendix A); the program divides the piston stroke in several steps (Fig. 3.15) calculates the air pressure, the piston acceleration and its speed at each one.

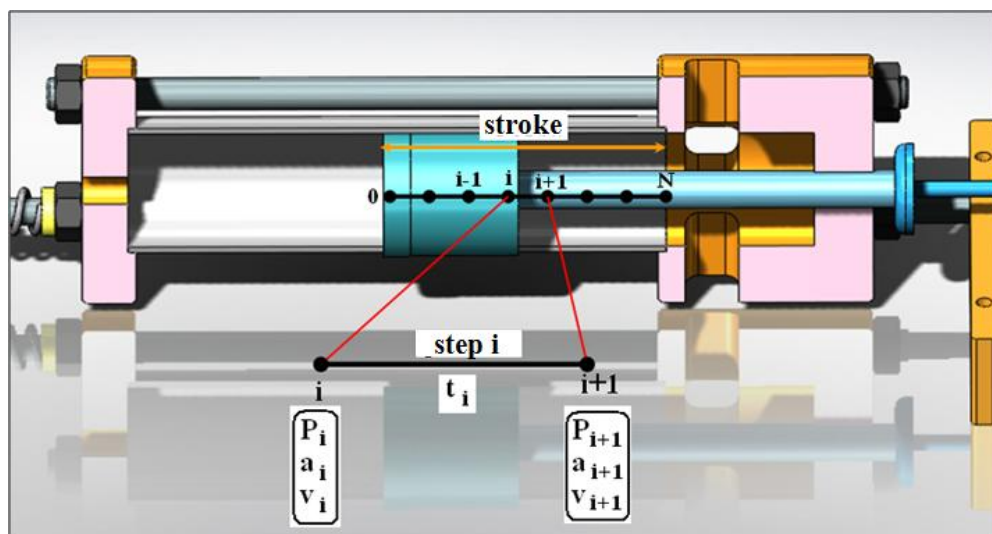


Figure 3.15. Piston stroke discretization.

The cylinder dimensions have been chosen in order to achieve the desired performance of the percussion system in terms of final piston speed (for performance evaluation see Section 4.2).

For example, the following graphs depict the expected piston speed, in case of a maximum stroke of 100 mm, for different values of cylinder diameter  $\phi$  (Fig. 3.16) and back chamber volume  $V_0$  (Fig. 3.17) with air pressure inside the

cylinder back chamber  $P_{\text{air}} = 1$  MPa. In the graphs, the reference value of final striker speed  $\overline{V}_{\text{imp}} = 18.4$  m/s (calculated in Section 4.2.1) is shown.

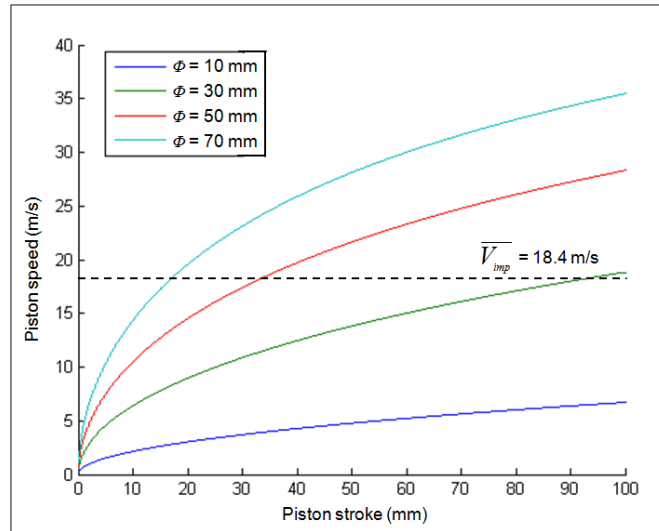


Figure 3.16. Expected piston speed for different values of cylinder diameter ( $P_{\text{air}} = 1$  MPa,  $V_0 = 19.6 \cdot 10^{-5} \text{ m}^3$ ).

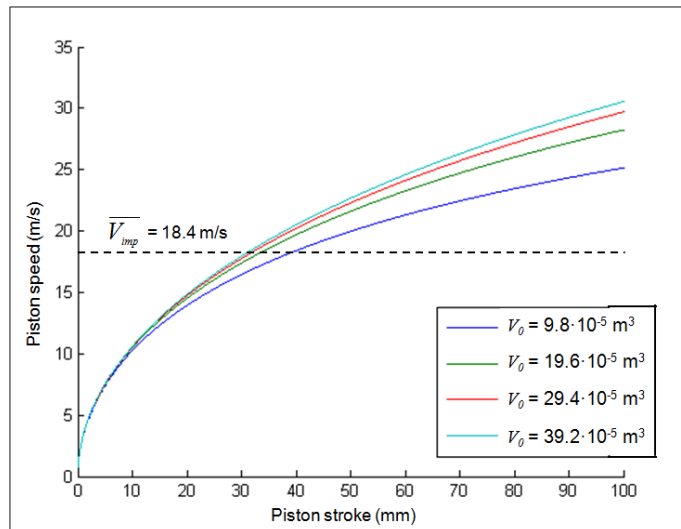


Figure 3.17. Expected piston speed for different values of cylinder back chamber volume ( $P_{\text{air}} = 1$  MPa,  $\phi = 50$  mm).

Note that the back chamber volume  $V_0$  depends on the cylinder diameter  $\phi$  and on the back chamber initial length  $X_0$ , as shown in Fig. 3.18.

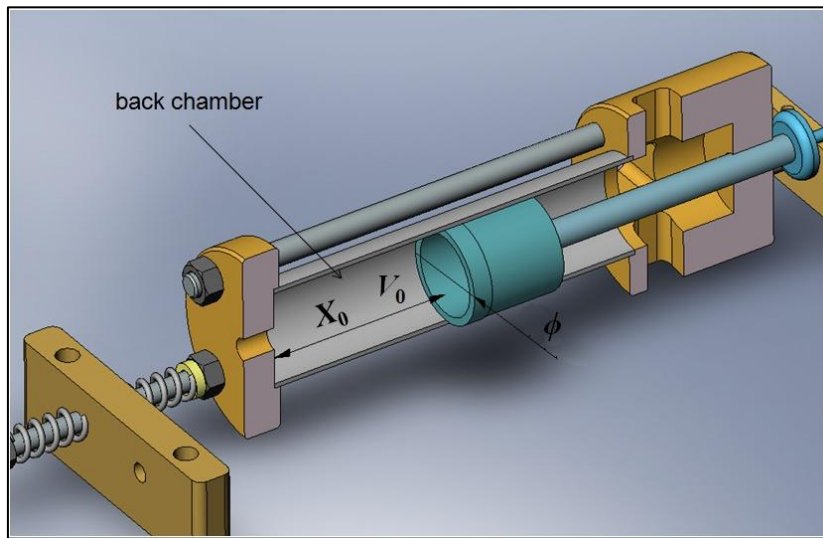


Figure 3.18. Back chamber section.

Both the previous graphs refer to a situation in which the air pressure inside the back chamber  $P_{\text{air}}$  decreases when the back chamber volume increases (this condition corresponds to closed air inlet valve); the following graph (Fig. 3.19) compares it to the situation in which  $P_{\text{air}}$  keeps constant due to the ideal connection to an infinite cylinder volume (open air inlet valve case).

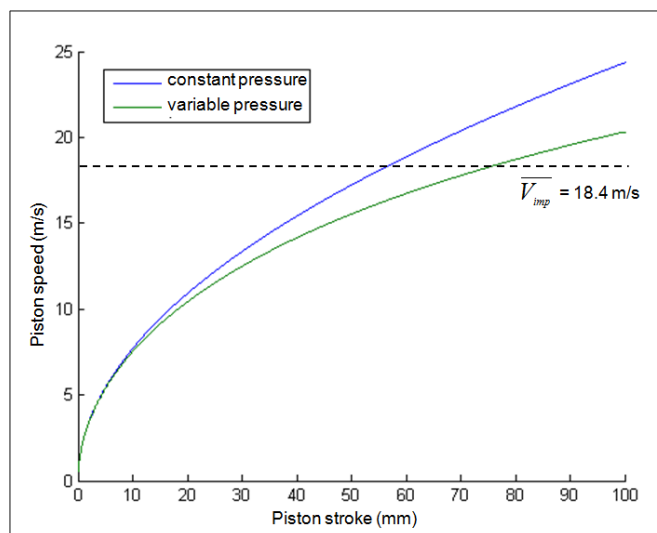


Figure 3.19. Expected piston speed for variable and constant  $P_{\text{air}}$  ( $P_{\text{air}} = 0.5 \text{ MPa}$ ,  $\phi = 50 \text{ mm}$ ,  $V_0 = 19.6 \cdot 10^{-5} \text{ m}^3$ ).

Calculations show that a cylinder diameter  $\phi = 50$  mm and a back chamber initial volume  $V_0 = 19.6 \cdot 10^{-5} \text{ m}^3$  (corresponding to a chamber initial length  $X_0 = 90$  mm) ensure the desired QSD performance (see Section 4.2.1) for an air pressure inside the cylinder  $P_{\text{air}}$  down to 0.5 MPa (the maximum pressure supplied by the compressed air circuit is 1 MPa but for safety reasons it is recommended to operate with a lower pressure).

Due to materials availability, the actual percussion system dimensions should be slightly different from those listed above. The final system specifications are summarized in Tab. 3.1.

Table 3.1. Percussion system specifications.

quantity	value
Cylinder diameter $\phi$	50 mm
Cylinder length	200 mm
Cylinder wall thickness	2.5 mm
Back chamber initial length $X_0$	90 mm
Back chamber initial volume $V_0$	$18 \cdot 10^{-5} \text{ m}^3$
Piston stroke	110 mm

### 3.2.3 Controlling and synchronizing system

The micro QSD is managed by an electronic system specifically designed for this purpose, which is able to handle the different phases of quick-stop experiments. The system concept is shown by Fig. 3.20 while the software which controls it is described in detail in Appendix C.

This system is composed by three circuits, each one devoted to control a phase of the quick-stop experiment:

- 1 (red in Fig. 3.20) detects the beginning of the turning operation by means of an electric contact between the tool and the workpiece and sends this information to the control software via the purpose-built electronic circuit (which is depicted in Fig. 3.21 and whose schematics is shown in Appendix C);
- 2 (blue in Fig. 3.20) creates a voltage which activates the solenoid and triggers the percussion system after the amount of time from the turning operation beginning set in the software;
- 3 (orange in Fig. 3.20) measures the striker speed at the impact  $V_{\text{imp}}$ .

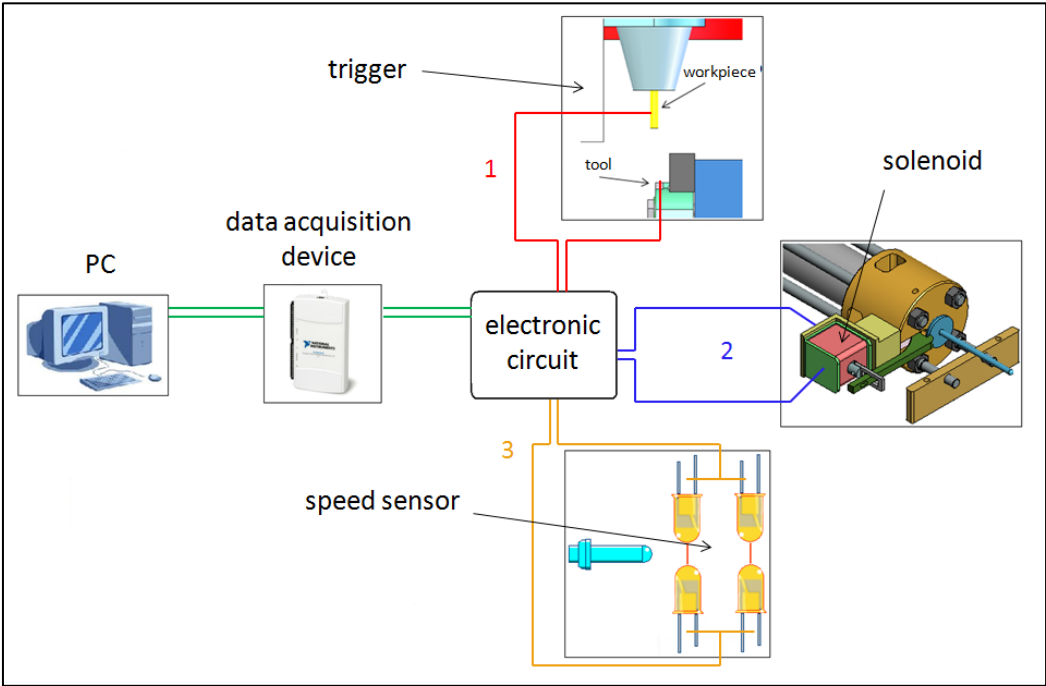


Figure 3.20. QSD controlling and synchronizing system.

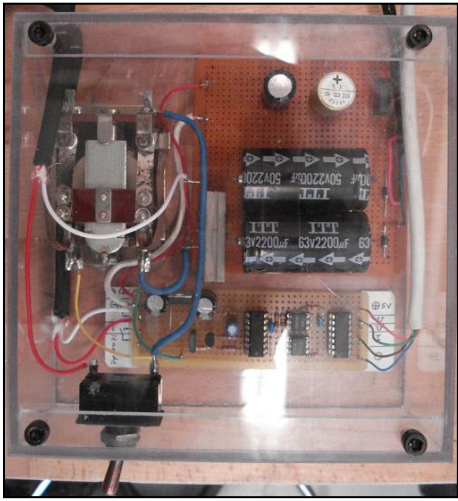


Figure 3.21. Electronic circuit.





## Chapter 4

### Micro QSD performance characterization

As stated in Chapter 1, the main objective of the present study is not only to characterize the developed micro QSD performance but to carry out a system able to evaluate such a performance at each experiment. This way, each chip micrograph can be provided with the conditions under which it has been obtained. This is an improvement respect to most of the existing QSDs, which have been only once characterized before their use ([26-27, 30-34, 37-40, 46, 48]) or have not been characterized at all ([25, 28], all devices described in [29], [42-43, 45, 50], see Tab 1.4).

#### 4.1 Performance characterization

It is not possible to directly measure (on the QSD or on the chip micrographs) the parameters quantifying the QSD performance, i.e. the separation time  $t_s$  and the separation distance  $d_s$ , but, as shown by Equation (1.2) in Section 1.3, Group 4, they can be evaluated from the tool speed law  $V_t(t)$  (Fig. 4.1).

As shown in Section 3.2.1, since in the developed micro QSD the tool holder motion is rotational, the tool-workpiece separation is completed when the horizontal component of the tool speed  $V_{t,x}$  becomes equal to the cutting speed  $V_c$ ; therefore  $V_{t,x}(t)$  has to be placed in Equation (1.2) instead of  $V_t(t)$  obtaining Equation (1.1), here reported for sake of clarity.

$$d_s = d_w - d_t = V_c \cdot t_s - \int_0^{t_s} V_{t,x}(t) dt \quad (4.1)$$

The tool speed law  $V_t(t)$  which will then be projected on the horizontal direction, can be calculated according to three cases:

- i) basing on the air pressure inside the cylinder  $P_{air}$  (Fig. 4.1) acquisitions and on the piston and tool holder motion physical models (see Section 4.2);
- ii) basing on the striker speed at the impact  $V_{imp}$  (Fig. 4.1) acquisitions and on the tool holder motion physical model (see Section 4.3);
- iii) basing on direct acquisitions of  $V_t(t)$  (see Section 4.4).

Note that these cases are presented in order of increasing accuracy since, passing from i) to iii), less restrictive physical hypothesis are applied to the

employed models (if any). In any case, the accuracy of the  $V_t(t)$  law is obviously affected by the applied sensors performances.

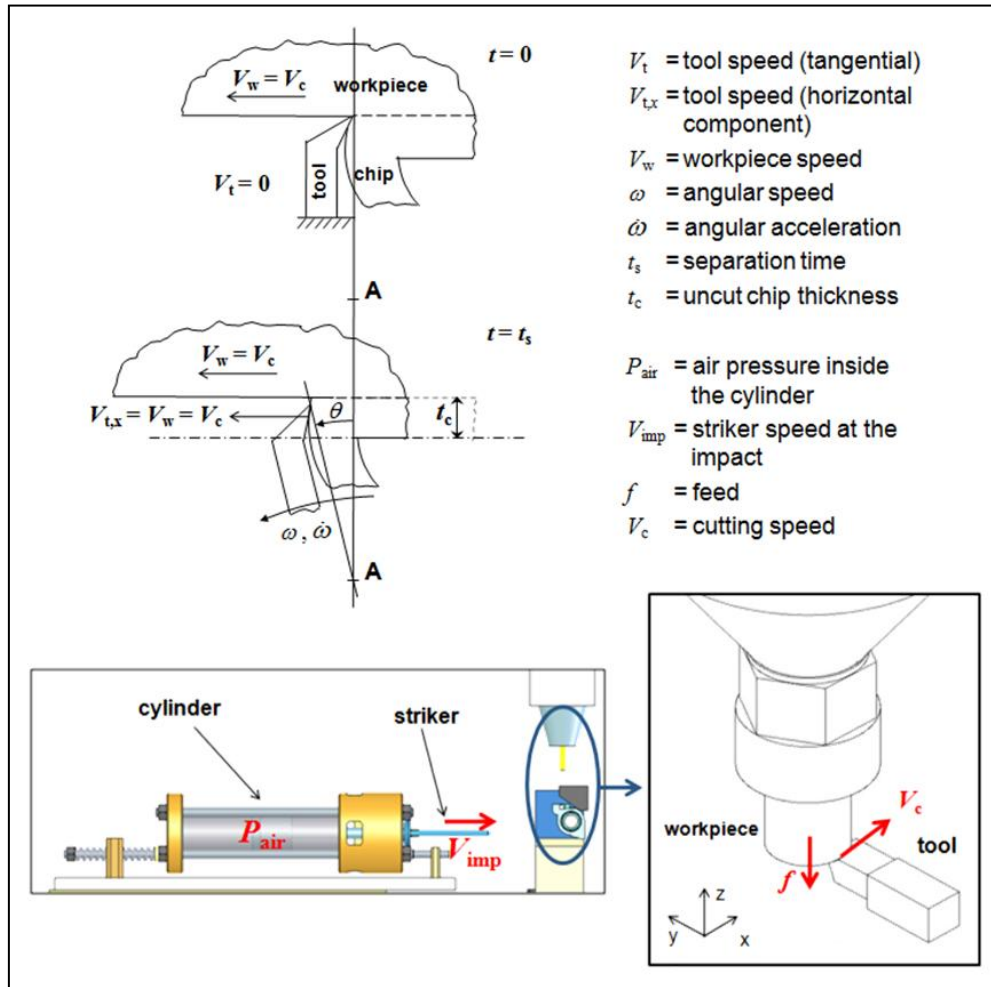


Figure 4.1. Scheme of the quick-stop experiment (adapted from [30]) and layout of the micro QSD.

## 4.2 First performance characterization method

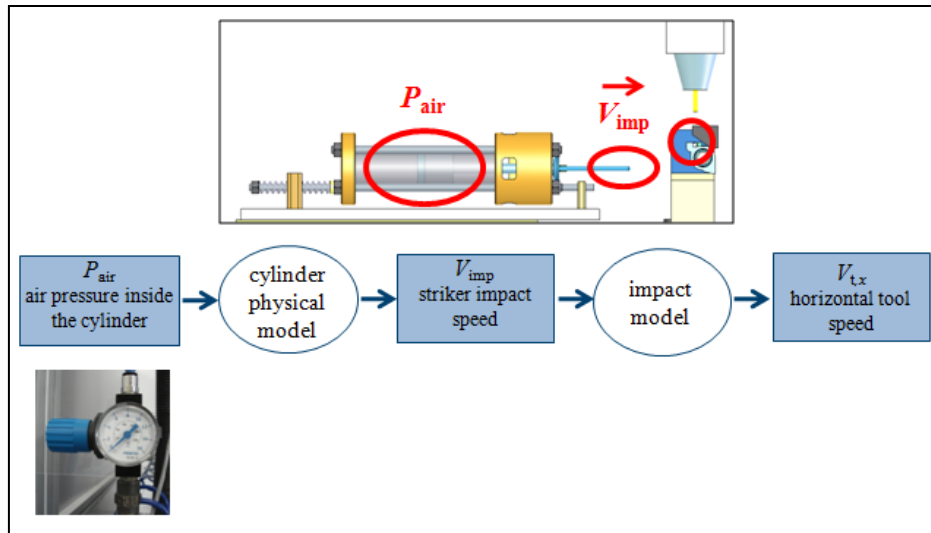


Figure 4.2. Scheme of the first performance characterization method.

The first performance characterization method (described in detail in [59-60]) allows to calculate an expected value of the horizontal component of the tangential tool speed  $V_{t,x}$  basing on the acquired value of the air pressure inside the cylinder  $P_{air}$ .

Starting from the initial air pressure, a physical model of the air expansion inside the cylinder is used to estimate the expected final striker speed, called “striker speed at the impact”  $V_{imp}$  (the used Matlab® program is described in detail in Appendix A).

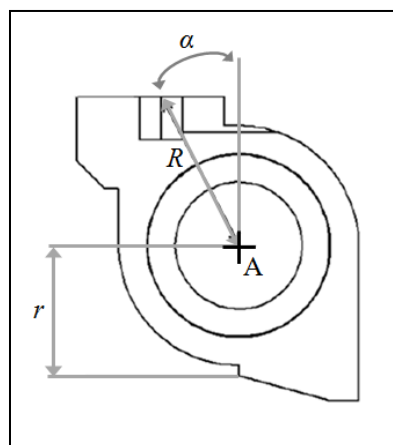


Figure 4.3. Scheme of the tool holder rotating part (front view).

After that, the angular momentum conservation law under the hypothesis of perfectly plastic and instantaneous impact [64] is applied to calculate the angular speed  $\omega$  of the tool as shown in the following equation:

$$\omega = \frac{V_{imp} \cdot r \cdot m_1}{(I_2 + m_1 \cdot r^2)} \quad (4.2)$$

where  $r$  is the distance (equal to 18.5 mm, Fig. 4.3) between the impact area at the tool holder and the tool holder hinge (point A in Fig. 3.11 and Fig. 4.3),  $m_1$  is the concentrated mass of the striker (equal to 0.27 kg) and  $I_2$  is the tool holder moment of inertia comprising the tool (equal to  $2.34 \cdot 10^{-5} \text{ kg} \cdot \text{m}^2$ ). The foregoing equation comes from modelling the striker-tool holder impact as the eccentric impact between a sphere and an homogeneous rod pivoted at its end [64], like shown in Fig. 4.4.

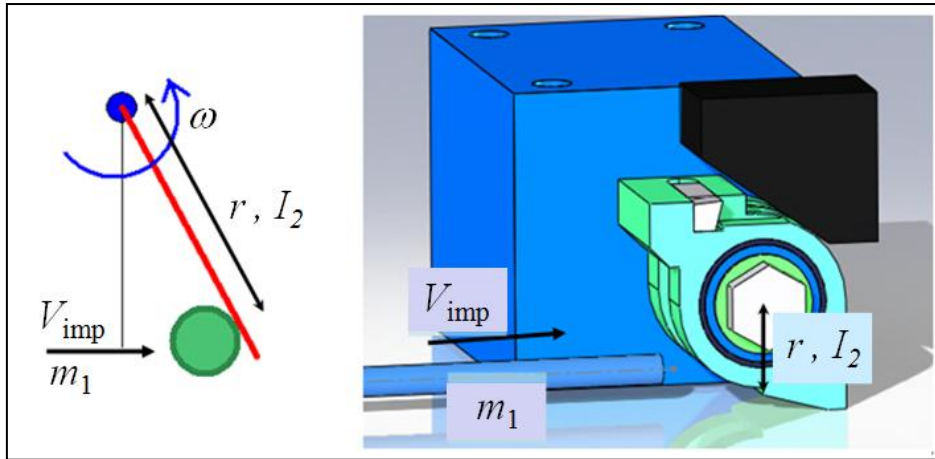


Figure 4.4. Scheme of the impact model.

Finally, the horizontal component of the tangential tool speed  $V_{t,x}$  is calculated as follows:

$$V_{t,x} = \omega \cdot R \cdot \cos(\alpha) \quad (4.3)$$

where  $R$  is the distance (equal to 23.7 mm, Fig. 3.11 and Fig. 4.3) between the tool cutting edge and the tool holder hinge and  $\alpha$  is an angular offset (equal to 0.483 rad, Fig. 3.11 and Fig. 4.3) between the tool cutting edge and the vertical line passing from the tool holder hinge.

### 4.2.1 Results

The graph depicted in Fig 4.5 shows the expected striker speed at the impact  $V_{\text{imp}}$  for different values of the initial air pressure inside the cylinder  $P_{\text{air}}$ ; the dotted line refers to the most favourable case in which  $P_{\text{air}}$  can be considered constant due to an infinite cylinder volume (this condition corresponds to open air inlet valve) while the dashed line describes the worst case in which  $P_{\text{air}}$  keeps decreasing due to the piston back chamber volume increase (this is the case in which air inlet valve is closed). For more details see Section 3.2.2 while the used Matlab® program is reported in Appendix A.

The dashed blue lines represents the  $P_{\text{air}}$  value considered in the percussion system design phase (see Section 3.2.2).

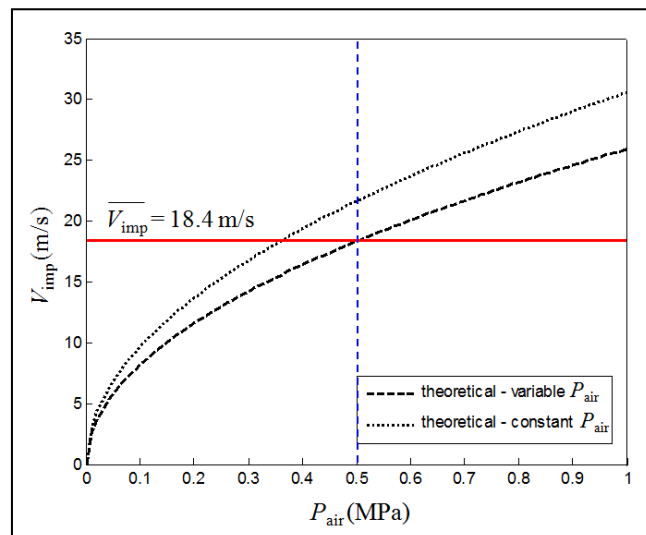


Figure 4.5. Expected striker speed at the impact  $V_{\text{imp}}$  (dashed blue = design  $P_{\text{air}}$  value).

According to a reverse approach, the same graph of Fig. 4.5 (which explicitly depends on the device design) can be used to choose the proper air pressure inside the cylinder  $P_{\text{air}}$  for each test, depending on the striker speed at the impact  $V_{\text{imp}}$  which is needed to correctly separate the tool from the workpiece which is moving at a certain cutting speed  $V_c$ .

For example, considering a required cutting speed  $\bar{V}_c$  equal to 1000 m/min (this value comes from a cutting speed which is typical for micromachining  $\bar{V}_c = 200$  m/min multiplied by a safety factor equal to 5) Equation (4.3) lead to  $\bar{\omega} = 794$  rad/s and then Equation (4.2) leads to  $\bar{V}_{\text{imp}} = 18.4$  m/s. This means that in a quick-stop test where the workpiece has a cutting speed

$V_c = 1000$  m/min, an air pressure inside the cylinder  $P_{air}$  between about 0.4 and 0.5 MPa should be used in order to correctly achieve the tool-workpiece separation. These values of the critical quantities have been considered for the system design (see Section 3.2.2).

### 4.3 Second performance characterization method

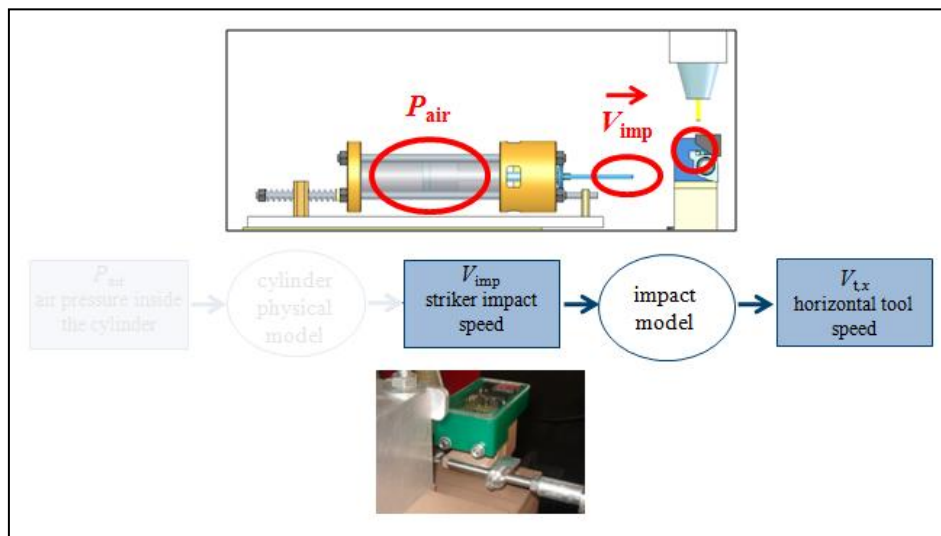


Figure 4.6. Scheme of the second performance characterization method.

According to the second performance characterization method (presented in detail in [59]) the horizontal component of the tangential tool speed  $V_{t,x}$  is obtained by measuring the striker velocity at the impact  $V_{imp}$  at each run thanks to an electronic system composed by two couples of facing photodiodes (Fig. 4.7); then the already discussed Equations (4.2) and (4.3) are respectively applied in order to calculate the angular speed  $\omega$  of the tool holder rotating part through the angular momentum conservation law [64], and the horizontal component of the tangential tool speed  $V_{t,x}$ , which represent the QSD performance.

#### 4.3.1 Impact speed sensor

The electronic system developed for measuring the striker speed at the impact  $V_{imp}$  (whose versions for the two tool holder block layouts are shown in Fig. 4.7) is composed by two couples of facing photodiodes and is positioned before the rotating part of the tool holder.

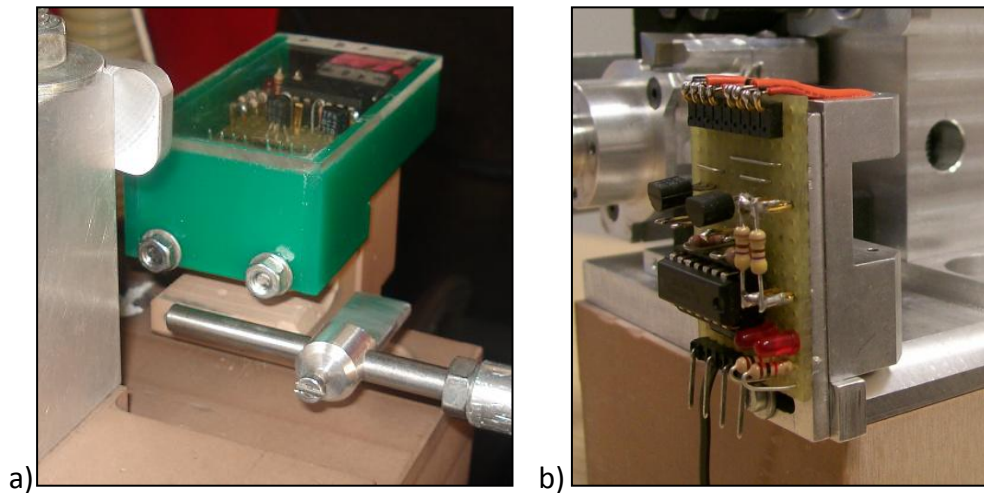


Figure 4.7.  $V_{imp}$  measuring sensor for the a) first and b) second version of the tool holder block.

When the striker passes through a couple of photodiodes, it reduces the amount of light acquired by the receiver making the diode output voltage lower; the measuring system is able to calculate the time period between the voltage losses related to the striker passage through the two couples of photodiodes and, since their distance  $D$  (Fig. 4.8) is known, it allows the calculation of  $V_{imp}$  by dividing  $D$  by that time period.

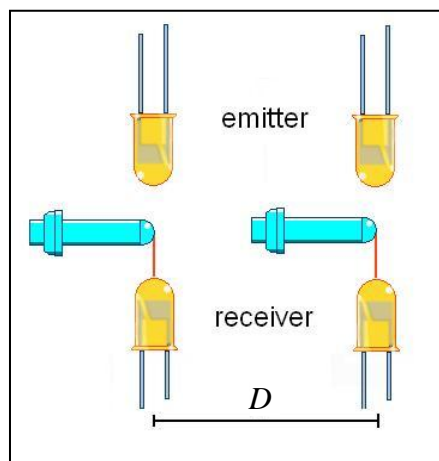


Figure 4.8. Scheme of the  $V_{imp}$  measuring sensor.

Since this system relies on a data acquisition device, the speed calculation resolution is determined by the maximum acquisition frequency (125 kS/s) since it defines the minimum time step between the acquired points (for

example, in the range of acquired velocities, the resolution passes from 0.23 m/s for  $V_{\text{imp}} = 15$  m/s to 0.41 m/s for  $V_{\text{imp}} = 20$  m/s).

### 4.3.2 Results

The results of a striker speed measurement campaign for different values of pressure inside the cylinder  $P_{\text{air}}$  is shown in Fig. 4.9 and in details in Fig. 4.10. Five tests have been carried out for each one of the five pressure levels.

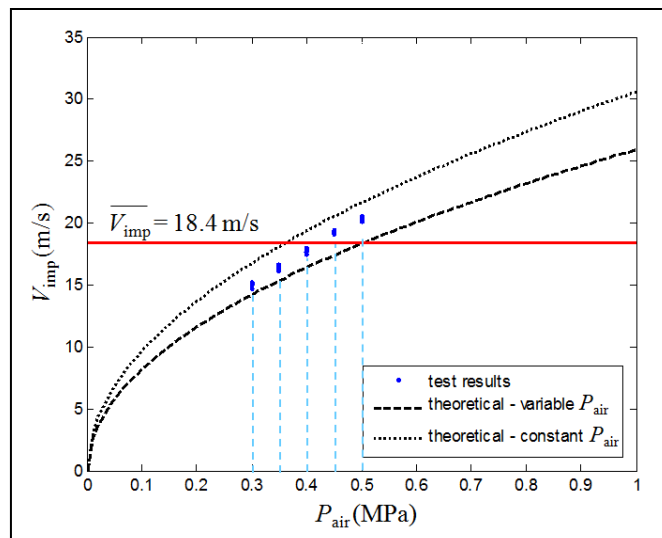


Figure 4.9. Results of  $V_{\text{imp}}$  measured (blue) and expected striker speed at the impact  $V_{\text{imp}}$ .

These results confirm that the micro QSD performance is coherent with the device design; as a matter of fact, Fig. 4.10 shows that the obtained values of the striker impact speed  $V_{\text{imp}}$  are distributed around the target value  $\overline{V_{\text{imp}}} = 18.4$  m/s.



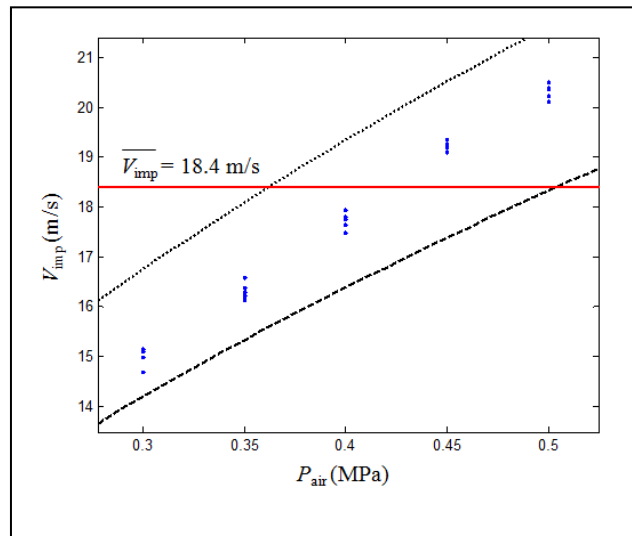


Figure 4.10. Results of the  $V_{\text{imp}}$  measurements (detail).

The experimental points are placed between the two theoretical limit cases of constant and variable  $P_{\text{air}}$  even if during tests the inlet valve is open and the pressurized air can continuously feed the percussion system; the reason for this fact is that the cylinder physical model does not take into account the pressure losses in the inlet valve, the O-ring frictional behaviour during the piston motion and the pressure variation due to the manual regulation of the inlet pressure.

In each quick stop experiment, the measured value of the striker speed at the impact  $V_{\text{imp}}$  has to be used to calculate the horizontal component of the tangential tool speed  $V_{t,x}$  thanks to Equations (4.2) and (4.3); the obtained  $V_{t,x}$  should then be compared with the workpiece cutting speed  $V_c$  in order to validate or refuse the effectiveness of the micro QSD for that particular test.

Applying the Equations (4.2) and (4.3) to the presented  $V_{\text{imp}}$  measurement results, it is possible to point out how the quick-stop device is effective for  $V_c < 798$  m/min at  $P_{\text{air}} = 0.3$  MPa (where  $V_{\text{imp}} = 14.69 \pm 0.19$  m/s). Effectiveness improves at higher  $P_{\text{air}}$ .

#### 4.4 Third performance characterization method

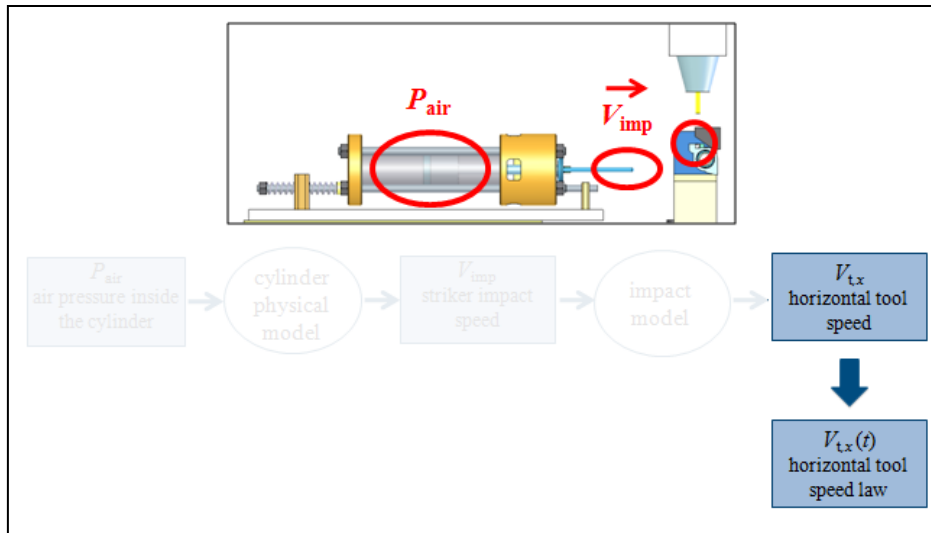


Figure 4.11. Scheme of the third performance characterization method.

The third performance characterization method (discussed in [61]) consists in measuring the angular position of the tool holder rotating part ( $\theta(t)$ ) during each test by means of an *ad hoc* sensor, and then calculating the horizontal tool speed law  $V_{tx}(t)$  deriving  $\theta(t)$  in time and projecting the resulting speed on the horizontal direction.

##### 4.4.1 Angular position sensors

Due to the high impact load and the dramatic acceleration to which the tool holder is subject, contact or fragile sensors (such as potentiometers and encoders) cannot be used for acquiring its angular position because breakage rapidly takes place.

A very promising kind of non contact sensors are the high speed cameras but the higher the acquisition frequency is, the lower the image resolution, thus the acquired frames tend not to be defined enough to be graphically analyzed in order to obtain the angular displacement law of the tool holder rotating part. This is clear in the sequence of Fig. 4.12 referring to a test carried out at  $P_{air} = 0.1$  MPa: the frames acquired with a frequency of 34482 frames/s have a resolution of 128 x 128 pixels (the used Phantom v5.1 high speed camera [65] has a minimum acquisition frequency of 1200 frames/s at a full resolution of

1024 x 1024 pixels and a maximum acquisition frequency of 95000 frames/s at a resolution of 64 x 32 pixels).

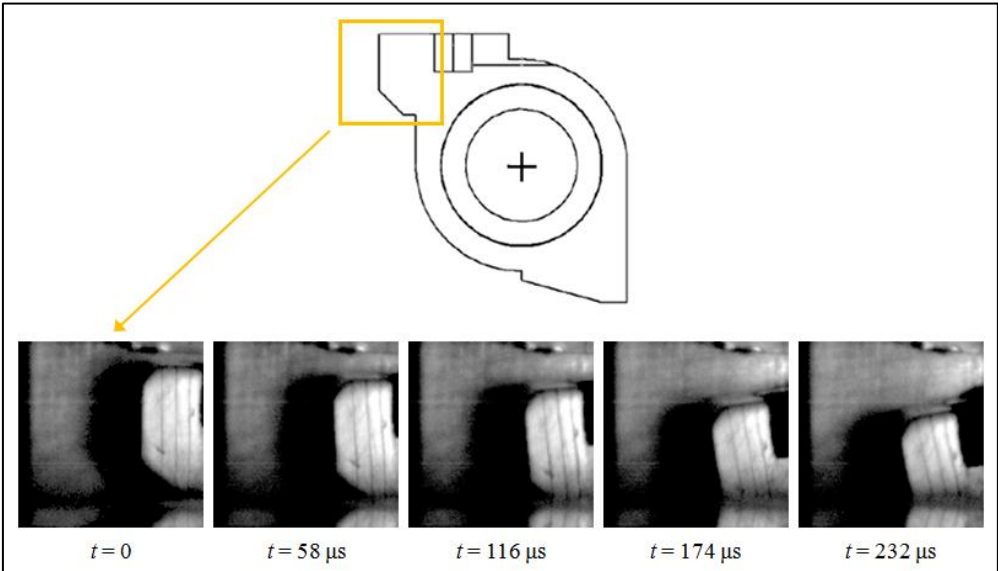


Figure 4.12. Sequence acquired by means of the high speed camera.

For the above stated reason, a sensor based on the laser triangulation principle and a sensor using polarizing filters have been designed and built in the frame of the present study in order to acquire the tool holder angular position law  $\theta(t)$ . Operation of both sensors will be discussed in the following, while their electronic circuit schematics are reported in Appendix D.

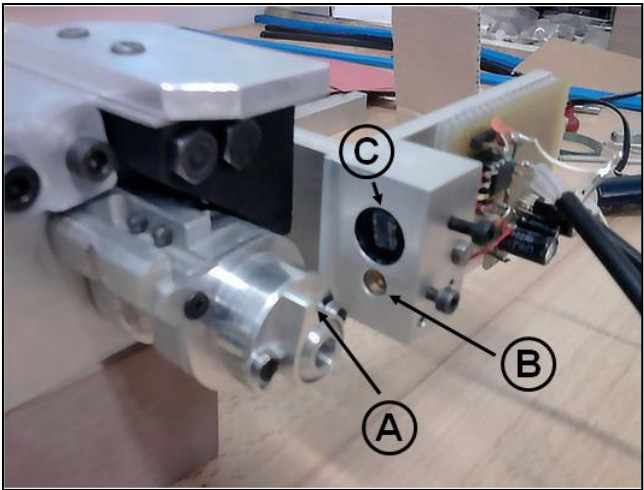


Figure 4.13. Laser triangulation sensor [A = reflecting surface, B = emitting diode, C = receiving diodes].

The laser triangulation sensor (shown in Fig. 4.13 already mounted on the tool holder block and schematized in Fig. 4.14) allows to measure the tool angular displacement from the cutting position according to the following principle: the laser beam coming from the emitting diode (B in Fig. 4.13) is reflected by a plane surface (which is part of a piece positioned on the rotating part of the tool holder; A in Fig. 4.13) and reaches a couple of receiving diodes (C in Fig. 4.13) whose output voltage is maximum when the beam hits the diode centre and decreases when it moves to the diode sides.

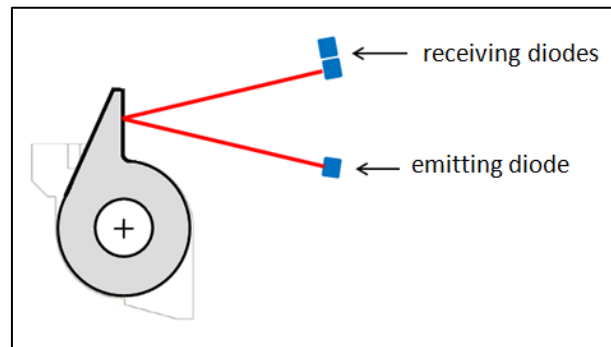


Figure 4.14. Scheme of the laser triangulation sensor.

Since the laser beam receiving part is made up by two diodes, the difference of the diodes output voltage signals is divided by their sum in order to obtain a single signal which is linear in the interval of interest (corresponding to the initial part of the tool holder motion, immediately after the impact) and also unaffected by the environmental light intensity.

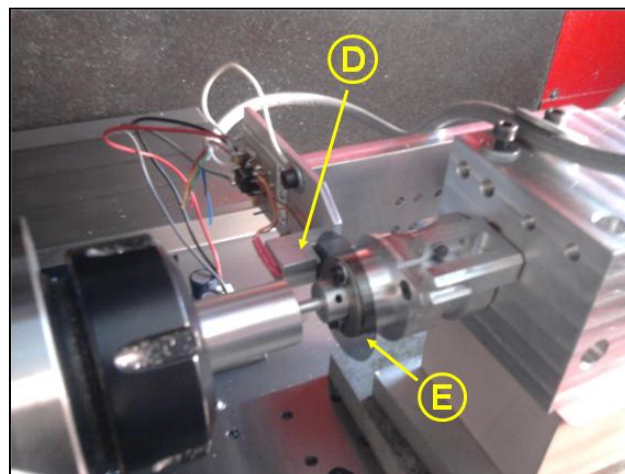


Figure 4.15. Angular position sensor based on polarizing filters [D = diodes holder, E = polarizing filter disc] during calibration.

The second angular position sensor developed in the present study (shown in Fig. 4.15 during its calibration and schematized in Fig. 4.16) consists of two parts: a disc of polarizing filter (with both linear and circular polarization) mounted on the tool holder rotating part (E in Fig. 4.15) and a fixed part (D in Fig. 4.15) with an emitting and a receiving diode, the second one covered by a foil of polarizing filter. The light intensity seen by the receiving diode is maximum when the polarization axis of the fixed and moving filters are parallel and is zero when they are perpendicular: therefore it is possible to know the tool holder angular position through the output voltage of the receiving diode.

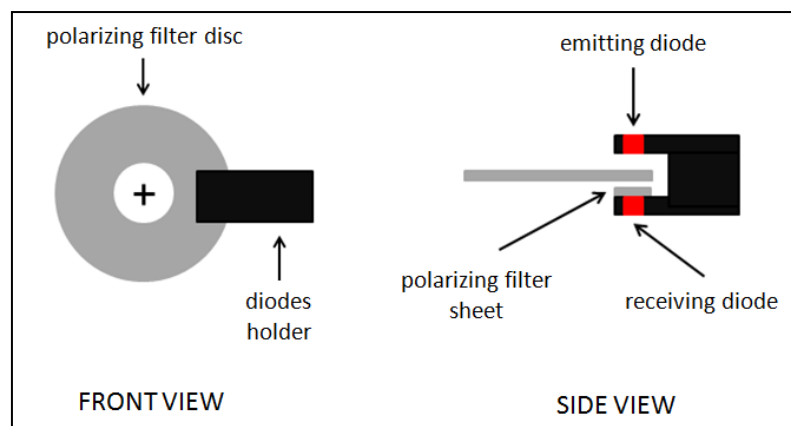


Figure 4.16. Scheme of the angular position sensor based on polarizing filter

It is mandatory for both sensors to perform a calibration in order to obtain the angular position of the tool holder from the acquired voltage signal; the best way to do it is to impose an angular displacement through the KERN Evo C axis (which has an accuracy of  $\pm 5'' = 0.014^\circ$  [51]) and then measuring the corresponding output voltage.

Fig 4.17 shows the two voltage signals of the sensor receiving diodes during one of the ten calibration tests performed on the laser triangulation sensor with an angular step of  $0.5^\circ$ ; Fig. 4.18 represents the results of dividing the difference of these signal by their sum.

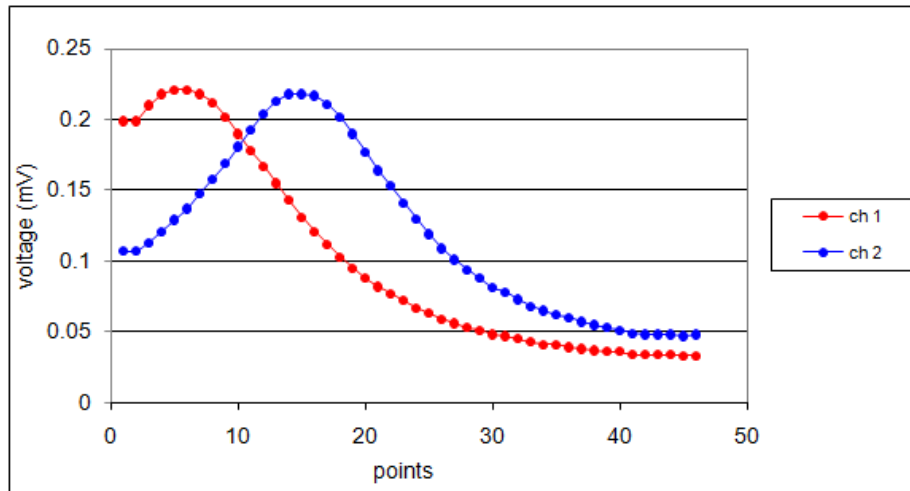


Figure 4.17. Signals acquired during a calibration test of the laser triangulation sensor.

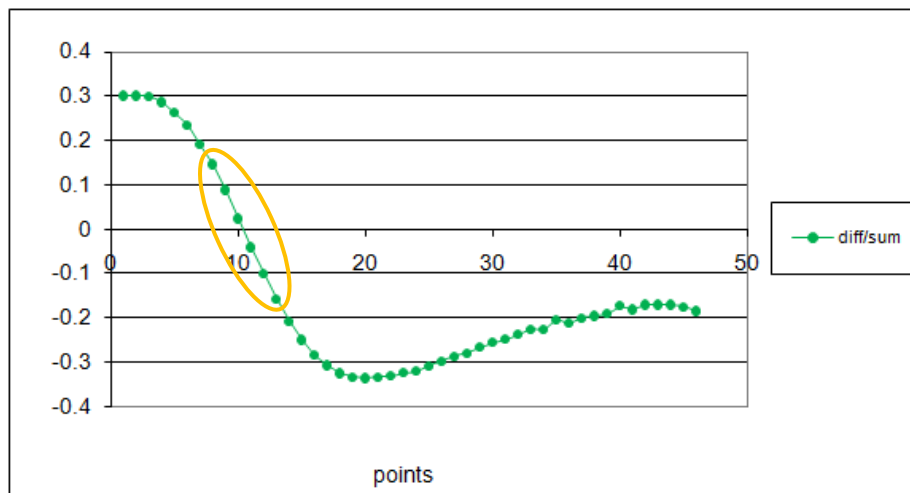


Figure 4.18. Result of dividing the difference of the Fig. 4.17 signals by their sum (laser triangulation sensor).

The resulting signal is almost linear only in a short interval (highlighted by the orange ellipse in Fig. 4.18) corresponding to a displacement of  $2^\circ$  thus, since the sensor calibration aims to find a proportionality between voltage and angular position, it should be carried out basing on the points included in that interval. The foregoing does not represent a problem since simple geometrical calculations show that, considering e.g. a reference uncut chip thickness  $t_c = 100 \mu\text{m}$ , the tool is able to leave the cutting area defined by  $t_c$  for an angular displacement equal to  $0.52^\circ$ ; anyway this means that the sensor signal

will be effectively transformed only in the same interval used in the calibration phase.

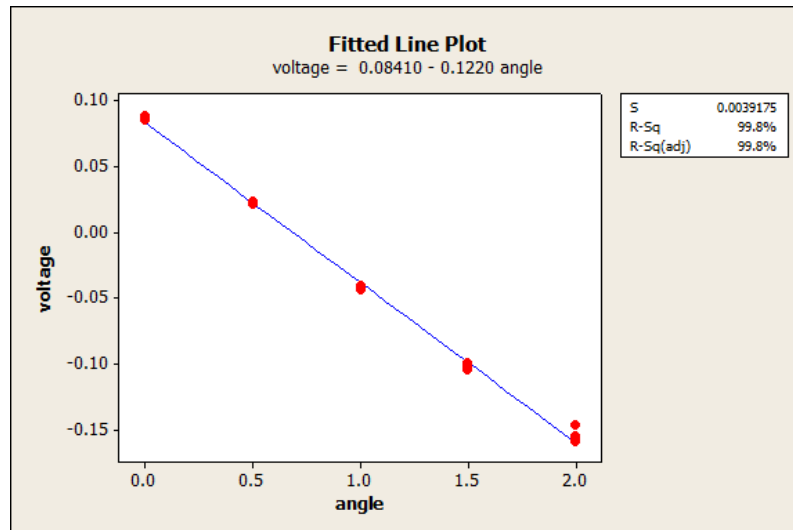


Figure 4.19. Result of linear regression on the selected points (laser triangulation sensor).

A standard procedure has been used for analyzing the calibration tests data. Fig. 4.19 depicts the result of the linear regression with a first degree polynomial applied to the 10 calibration test repetitions in the interest angle interval, as just the relative displacement from an arbitrarily imposed reference position is the matter of interest, only the line slope, which means the proportionality factor between angular position and voltage, should be considered.

For the laser triangulation system, the relation between voltage (expressed in mV) and angular displacement (expressed in degrees) is:

$$\text{difference} / \text{sum} = -0.1120 \cdot \theta \quad (4.4)$$

Fig 4.20 shows the voltage signals acquired from the angular position sensor based on polarizing filters during one of the ten calibration tests carried out with the KERN Evo C axis imposing an angular step of 0.5°.

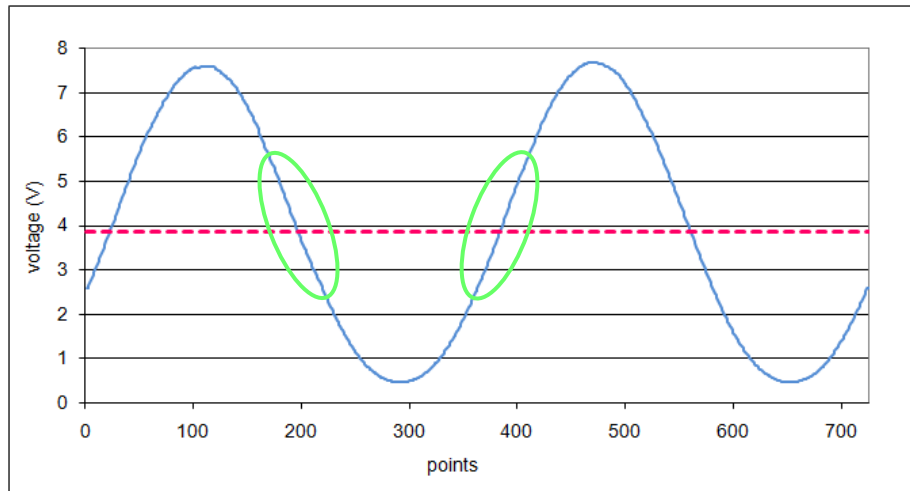


Figure 4.20. Signals acquired during a calibration test of the angular position sensor based on polarizing filters.

In the ascending and descending parts of the curve, the signal seems to be almost linear for an interval of 20 points (highlighted by the green ellipses in Fig. 4.20) around the signal mean (which is the red dashed lined in Fig. 4.20); therefore it is reasonable to use one of these sets of points to calculate the proportionality factor between voltage and angular position, also because they correspond to an angular displacement higher than the value needed by the tool to leave the cutting area.

Carrying out a linear regression with a first degree polynomial on the 10 calibration test repetitions in the interest angle interval (as shown in Fig. 4.21), the relation between voltage (expressed in V) and angular displacement (expressed in degrees) results:

$$\text{voltage} = 0.1291 \cdot \theta \quad (4.5)$$



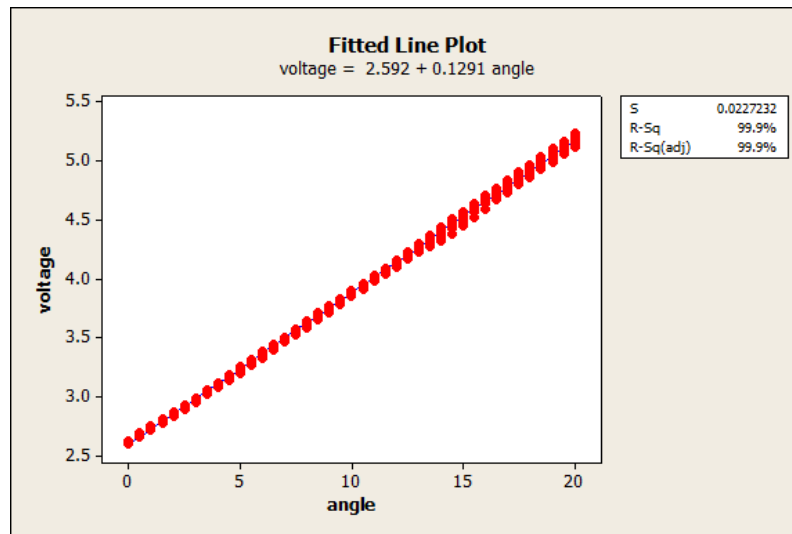


Figure 4.21. Result of linear regression on the selected points (polarized filters sensor).

#### 4.4.2 Data analysis

In order to calculate the separation distance  $d_s$  according to the Equation (4.1), the angular position data acquired by the sensors have been analyzed to obtain the tool speed law  $V_{t,x}(t)$  and the separation time  $t_s$ . Here only the analysis principles are described, using as example the signal acquired thanks to the laser triangulation sensor during a test at  $P_{\text{air}} = 0.1$  MPa; the whole procedure is analyzed in detail in Appendix E.

First of all, due to their irregularity, angular position signals (red in Fig. 4.22) have been smoothed by applying a local regression (this methodology is described in [66-69]); the best result (black in Fig. 4.22) is obtained with zero degree polynomial, which corresponds to calculate a moving average with a centered span equal to 10 % of data (this optimum value rises from the minimization of the residuals sum of squares).

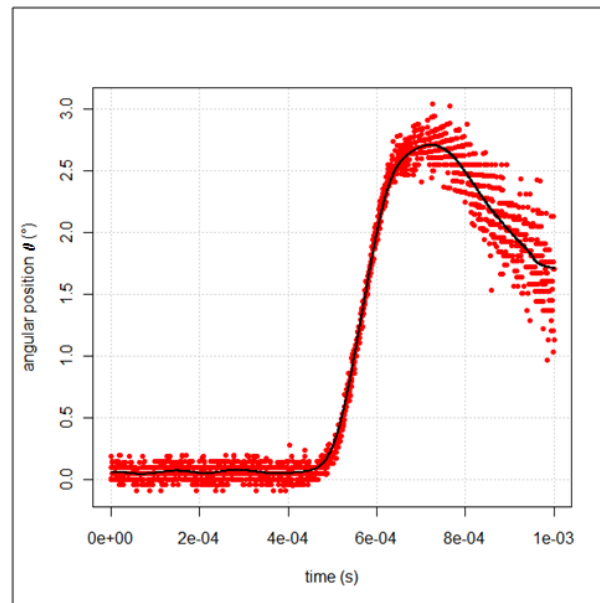


Figure 4.22. Original data (red) and moving average result (black) [tool holder motion law acquired by means of the laser triangulation sensor in a non-cutting test at  $P_{\text{air}} = 0.1$  MPa].

It should be noticed that scattered data on the right of Fig. 4.22 are at the end of the sensor working range, which has been centred to provide the best response where the angular position raising ramp takes place.

After smoothing, signal derivative  $V_i(t)$  has been numerically obtained by means of the finite differences method (see [71]) and finally it has been projected to calculate the horizontal component of the tool speed  $V_{t,x}$  (black in Fig. 4.22).

The separation time  $t_s$  is calculated as the difference between the time when the tool-workpiece separation ends (dot-dashed green in Fig. 4.23 and Fig. 4.24), which is the instant when the horizontal tool speed  $V_{t,x}$  becomes equal to the cutting speed  $V_c$  ( $= 100$  m/min in the considered example, dashed red in Fig. 4.23 and Fig. 4.24), and the time when the separation starts (dotted green in Fig. 4.23 and Fig. 4.24), whose identification is a critical issue which will be discussed in Section 4.4.3 .

Finally, in order to calculate the distance covered by the tool  $d_t$ , the tool speed law  $V_{t,x}(t)$  is numerically integrated along the separation time  $t_s$  (orange in Fig. 4.24).

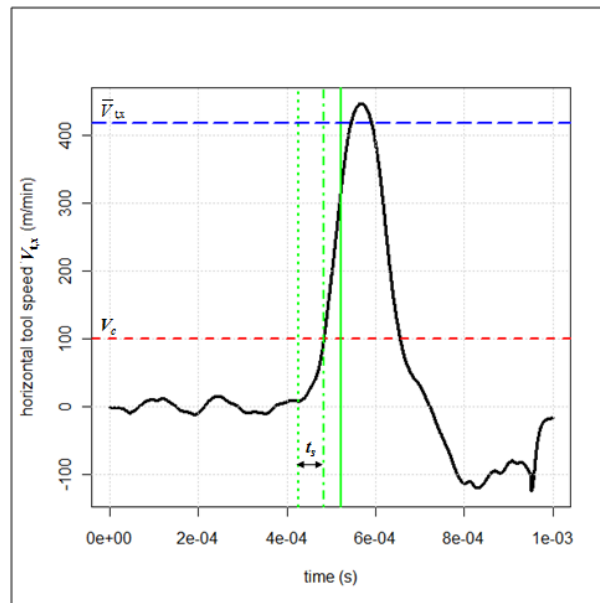


Figure 4.23. Horizontal tool speed (black), cutting speed (dashed red), tool-workpiece separation beginning (dotted green) and end (dot-dashed green), tool exit from the uncut chip thickness (solid green), expected horizontal tool speed (long-dashed blue) [tool holder motion law acquired by means of the laser triangulation sensor in a non-cutting test at  $P_{\text{air}} = 0.1$  MPa].

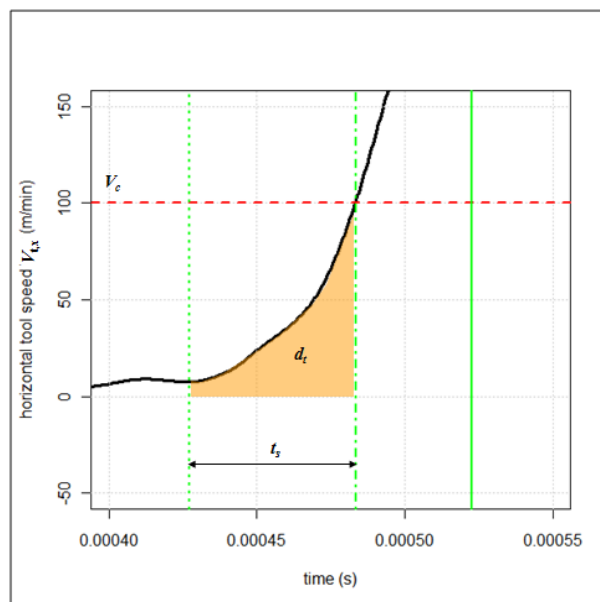


Figure 4.24. Horizontal tool speed (black), cutting speed (dashed red), tool-workpiece separation beginning (dotted green) and end (dot-dashed green), tool exit from the uncut chip thickness (solid green), distance covered by the tool (orange) [tool holder motion law acquired by means of the laser triangulation sensor in a non-cutting test at  $P_{\text{air}} = 0.1$  MPa].

As previously pointed out in Section 4.4.1, the cutting action can end also when the tool exits from the cutting area defined by the uncut chip thickness  $t_c$  (solid green in Fig. 4.23 and Fig. 4.24): here is proved that the necessary tool angular displacement is covered in a time that is higher than the separation time  $t_s$ .

As explained in Section 4.3, the expected horizontal tool speed  $\bar{V}_{t,x}$  can be calculated basing on  $V_{imp}$  acquisitions and on the tool holder motion physical model; it is now clear how this method allows to obtain only a reference value (long-dashed blue in Fig. 4.23) to be compared with the tested  $V_c$  while the direct acquisition of the angular position and the calculation of  $V_{t,x}(t)$  gives more information on the separation law, since it allows to enter in the impulse law avoiding to consider it as instantaneous.

### 4.4.3 Results

As mentioned before, the identification of the time when the tool-workpiece separation starts is very critical for defining the separation time  $t_s$ .

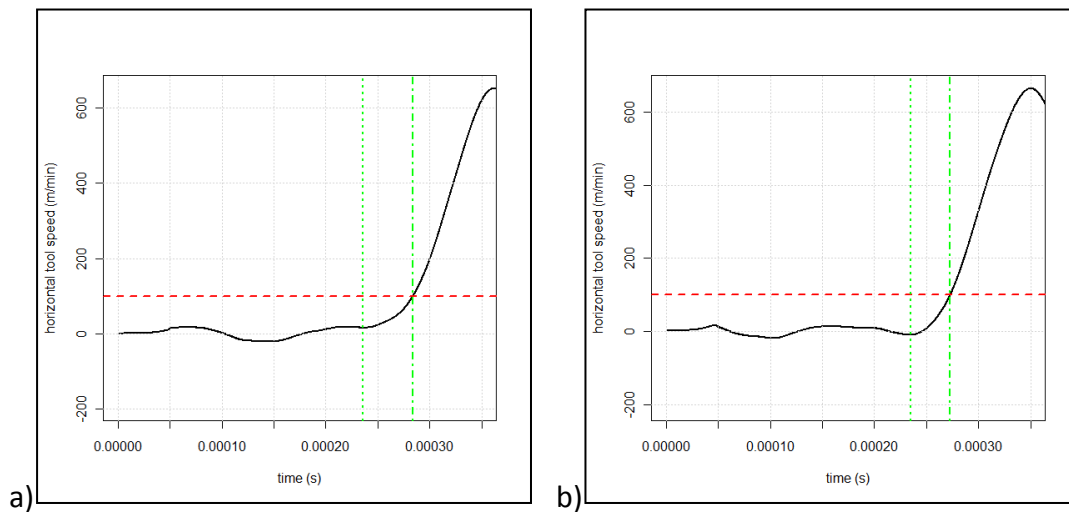


Figure 4.25. a) First and b) second type of tool holder behaviour [horizontal tool speed (black), cutting speed (dashed red), tool-workpiece separation beginning (dotted green) and end (dot-dashed green)].

Four test campaigns have been carried out with an air pressure inside the cylinder  $P_{air}$  of 0.2 MPa and 0.3 MPa and measuring the tool holder angular position by means of the laser triangulation sensor and the polarizing filters sensor. Analyzing data collected during these experiments, it clearly appears that the micro QSD behaviour may be classified in two categories (Fig. 4.25),

each one requiring a different criterion to identify the instant when the tool begins to separate from the workpiece.

As regarding the first type of behaviour (Fig. 4.25 a), it corresponds to a situation where the tool holder rotating part, which is initially still monotonically increases its speed after the striker impact; for this reason, the separation beginning can be identified as the instant when the tool speed (in the graph, its horizontal component  $V_{t,x}$ ) exceeds a threshold set equal to 5% of the cutting speed  $V_c$  (dotted green in Fig. 4.25 a).

In the other case (Fig. 4.25 b), the tool holder speed first increases, then decreases but does not become negative and finally begins to raise again; this could mean that the tool holder rotating part is initially pushed by the striker but separates from it to be hit again after a certain amount of time. This kind of behaviour requires that the separation beginning is identified as the instant when the horizontal tool speed  $V_{t,x}$  start increasing monotonically (dotted green in Fig. 4.25 b).

Tab 4.1, Tab 4.2 and Fig. 4.26, Fig. 4.27 summarizes the micro QSD performance in the test campaigns (fifteen replicates have been carried out with  $P_{\text{air}} = 0.2$  MPa and ten with  $P_{\text{air}} = 0.3$  MPa in order not to excessively stress the tool holder), while the acquired signals and their analysis are shown in Appendix F.

As it can be noticed in Fig. 4.26 and Fig. 4.27, in all campaigns the separation distance  $d_s$  has a high variability but lies in the same range (10-120  $\mu\text{m}$ ) regardless of the sensor with which the angular position is acquired. Taking into account a reference uncut chip thickness  $t_c = 100$   $\mu\text{m}$  (which can represent the upper limit for micromachining) it is clear how the separation distance is of the same magnitude order of  $t_c$ ; the influence of the separation distance on the chip microstructure should be further studied in order to better understand when an experiment can be considered valid and representing the chip formation process in its steady condition.

The reported results point out how is it possible to calculate the separation distance  $d_s$  and the separation distance  $t_s$  for each frozen cut test performed by means of the micro QSD; this way, experiments can be validated through an objective measurement. Moreover,  $d_s$  and  $t_s$  knowledge can be used to improve the quick-stop device performance.

Table 4.1. Micro QSD performance in campaigns with  $P_{\text{air}} = 0.2$  MPa.

run order	laser triangulation sensor		polarizing filters sensor	
	$t_s$ [ $\mu\text{s}$ ]	$d_s$ [ $\mu\text{m}$ ]	$t_s$ [ $\mu\text{s}$ ]	$d_s$ [ $\mu\text{m}$ ]
1	48	46.3	127.2	122.3
2	38	21.9	43.2	36.8
3	46	28.7	141.6	88.9
4	59.2	46.5	58.8	48.1
5	64.4	41.4	70.8	41.3
6	99.2	59.1	70.4	38
7	48.8	25.2	84	52
8	97.2	52.9	62.8	39.4
9	46.8	35.1	38	37.9
10	52.8	23.8	74	78.7
11	36	37.0	58	59.1
12	91.6	42.4	81.2	54.2
13	73.6	42	109.2	116.3
14	35.2	15.0	65.2	52.9
15	30	30	96.4	48.5

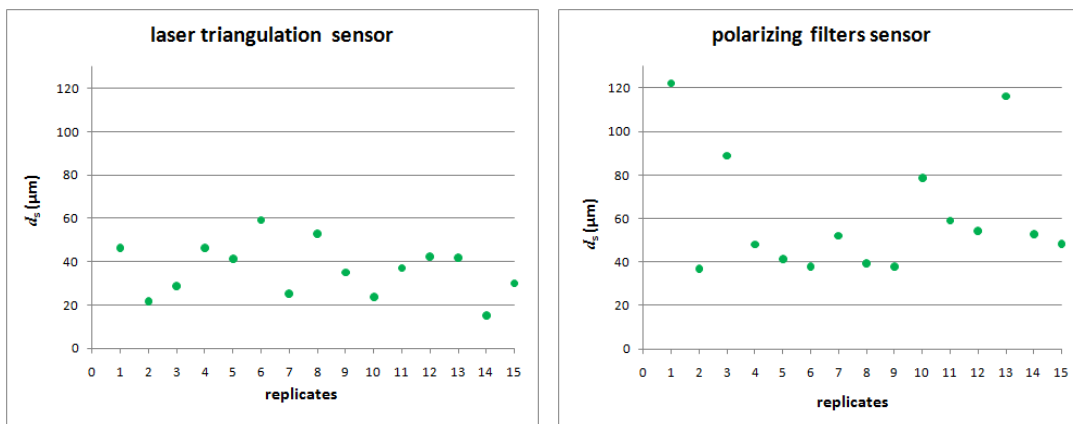
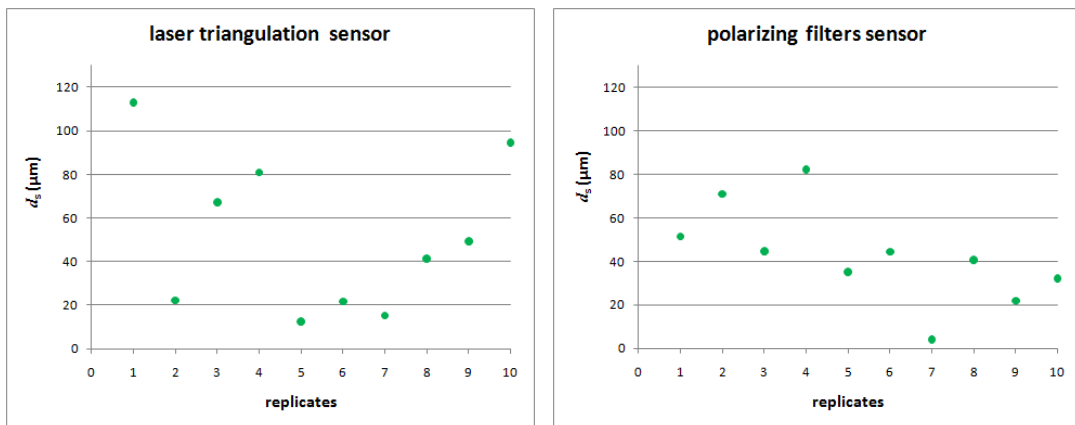
Figure 4.26. Micro QSD performance in campaigns with  $P_{\text{air}} = 0.2$  MPa.

Table 4.2. Micro QSD performance in campaigns with  $P_{\text{air}} = 0.3$  MPa.

run order	laser triangulation sensor		polarizing filters sensor	
	$t_s$ [ $\mu\text{s}$ ]	$d_s$ [ $\mu\text{m}$ ]	$t_s$ [ $\mu\text{s}$ ]	$d_s$ [ $\mu\text{m}$ ]
1	116.8	112.9	50.4	51.5
2	40.8	22.2	108	71.0
3	86.4	67.3	67.6	44.8
4	113.2	80.9	118.4	82.3
5	26.4	12.4	34	35.1
6	40.8	21.7	68.4	44.5
7	36	15.3	15.2	4.1
8	73.2	41.5	56.4	40.7
9	74.8	49.4	45.2	22
10	130	94.5	60	32.2

Figure 4.27. Micro QSD performance in campaigns with  $P_{\text{air}} = 0.3$  MPa.





## Chapter 5

### Preliminary tests

In order to test the device effectiveness, some preliminary quick stop tests have been carried out on C10 steel at different cutting conditions. Their results showed how these experiments can be used in future to validate some theoretical statements presented in literature.

#### 5.1 C10 steel

A C10 steel has been chosen to perform some preliminary quick stop experiments mainly because it has quite fine grains; it is important in fact that grains are smaller than uncut chip thickness when machining in the microscale (see Section 1.1). Moreover, this kind of steel has a good machinability and is easy to polish and etch to highlight grain borders.

The following Fig. 5.1 shows the longitudinal and cross sections of a steel specimen after polishing and etching by means of a Nital solution with 2% of  $\text{HNO}_3$  for 10-15 seconds.

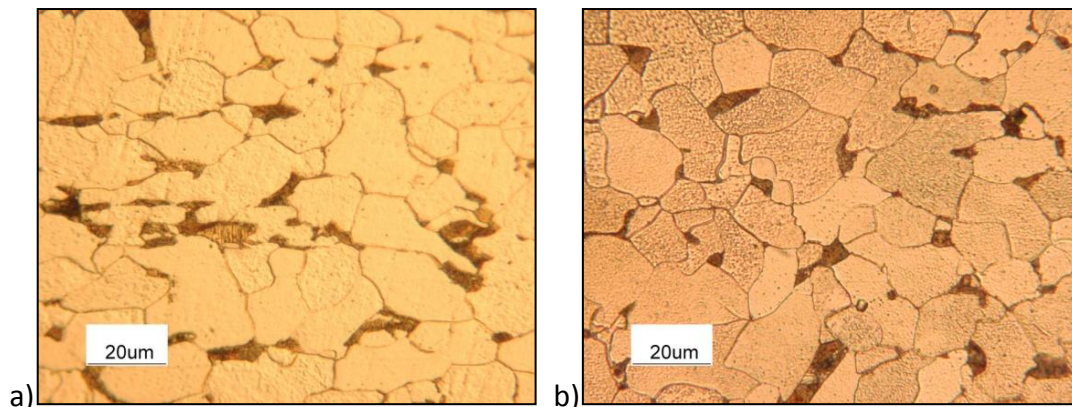


Figure 5.1. C10 microstructure: a) longitudinal and b) cross section.

It can be noticed that grains are more or less equiaxial in both sections and their greatest dimension is not bigger than 20-30  $\mu\text{m}$ ; therefore this material is suitable to be used in the experiments.

Vickers microhardness tests have been carried out on specimens sections according to ISO 6507-1 : 2005 standard [72] with a test force of 2942 N (corresponding to 300 g). The steel hardness resulted to be  $183 \pm 6.9 \text{ HV}_{0.3}$ .

## 5.2 Tool

The tool chosen for these experiments is a simple uncoated HSS left turning tool, made on request with cutting angles suitable for machining low carbon steel.

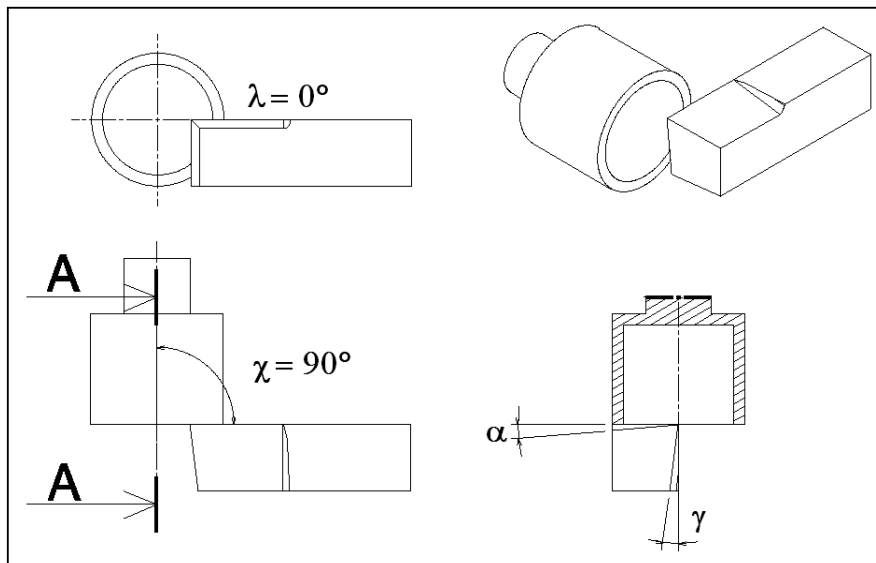


Figure 5.2. Turning tool model.

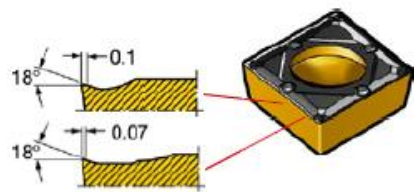
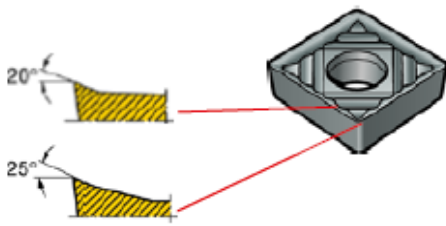
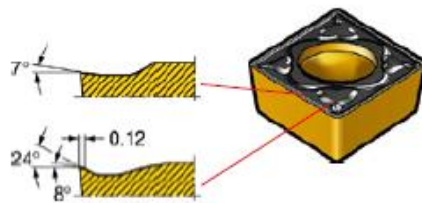

The following table summarizes the tool specifications.

Table 5.1. Tool specifications.

angle	value
$\alpha$ (clearance angle)	$9^\circ$
$\gamma$ (rake angle)	$9^\circ$
$\lambda$ (cutting edge inclination)	$0^\circ$
$\chi$ (entering angle)	$90^\circ$

When machining with low uncut chip thickness, the cutting edge radius should be as smaller as possible due to the “uncut chip thickness effect” and other size effects (see Chapter 1); for this reason, the suitable tool has been chosen among the ones listed in Tab. 5.2 thanks to some measurements made with both a contact and an optical instrument, respectively the Mitutoyo CONTRACER CV3100 profilometer [73] and the Alicona Infinite Focus [74].

Table 5.2. Analyzed tools (for 1-3 see [75-76]).

tool n°	tool name	image
1	Sandvik <u>DCMX 07 02 02 - WF 1125</u> (PVD coated hard metal)	
2	Sandvik <u>DCGX 07 02 02 – AL H10</u> (uncoated hard metal, for aluminum)	
3	Sandvik <u>DCMT 07 02 04 – KM H13A</u> (uncoated hard metal)	
4	custom HSS tool (uncoated)	

The measurement results (Tab. 5.3) point out how the cutting edge radius of the custom HSS tool (n°4 in Tab. 5.3) is similar to the radius of a turning insert

specific for aluminum (n°2 in Tab. 5.3 [75-76]) (which is not as flexible as the HSS tool since it does not allow to vary cutting angles as wanted).

Table 5.3. Angle measurement results.

tool n°	cutting edge radius	
	Mitutoyo profilometer	Alicona Infinte Focus
1	34 $\mu\text{m}$	38,3 $\mu\text{m}$
2	8 $\mu\text{m}$	10,6 $\mu\text{m}$
3	59 $\mu\text{m}$	56,6 $\mu\text{m}$
4	9 $\mu\text{m}$	---

Note that Alicona Infinite Focus failed in measuring the cutting edge radius on the HSS tool due to light reflection problems which caused a data loss in proximity of the edge.

### 5.3 Test results

A set of preliminary experiments has been performed with the following conditions:

- $f$  (feed) =  $t_c$  (uncut chip thickness) = 0.05 mm/rev;
- $a_p$  (depth of cut) = 0.5 mm;
- $V_c$  (cutting speed) = 50 ÷ 100 m/min.

It can be noticed that  $t_c$  has a quite high value for micro machining but it has been selected for the first experiments as it is easier to manage.

Fig. 5.3, Fig. 5.4 and Fig. 5.5 show the results of the three quick stop tests carried out for each different value of the cutting speed.

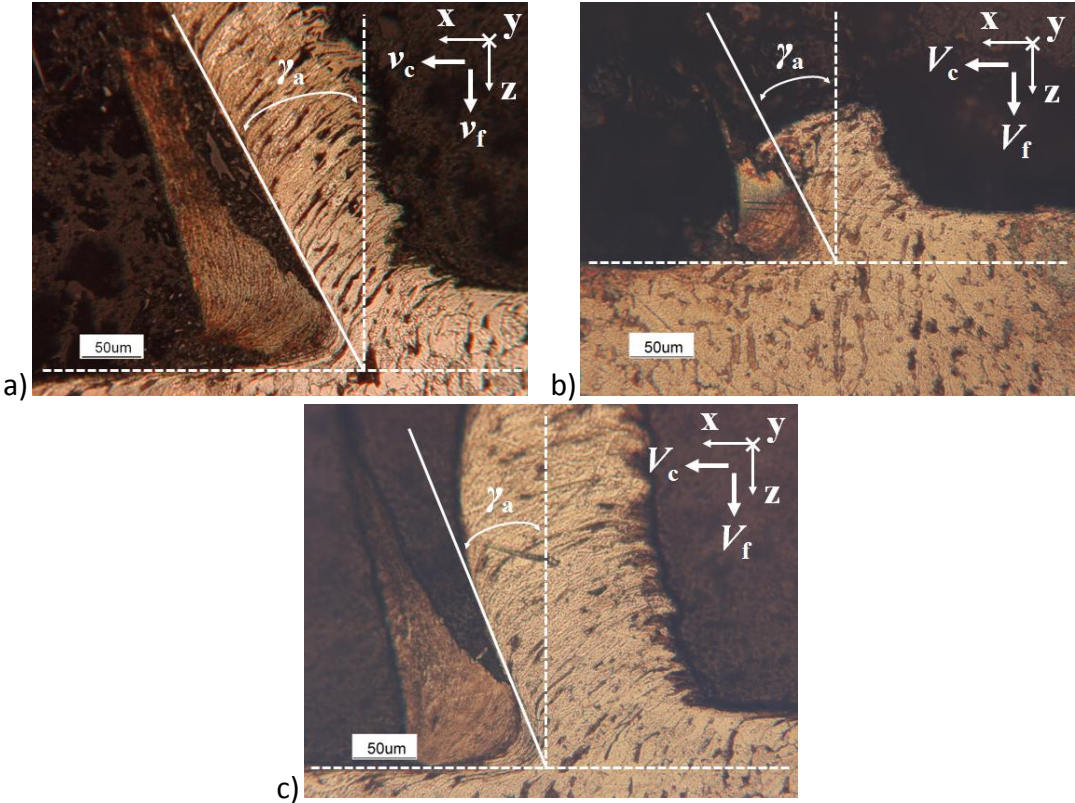
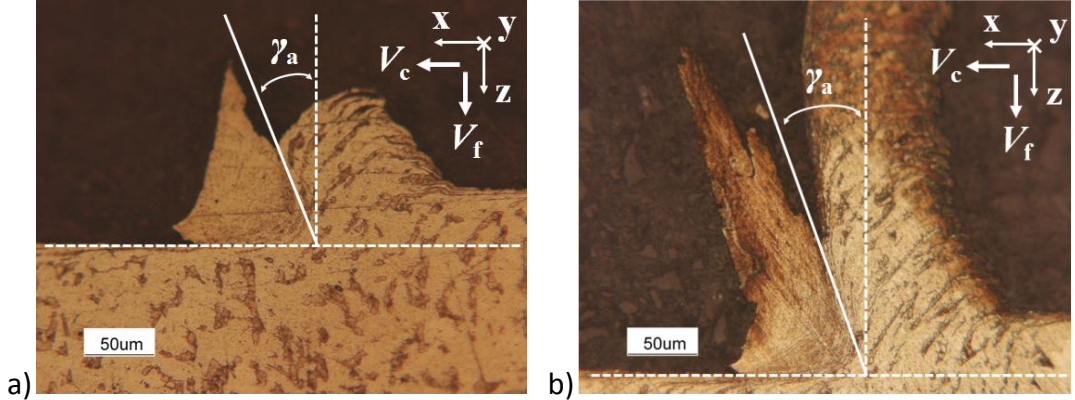
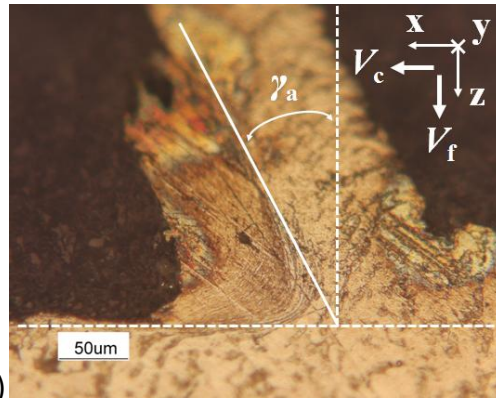


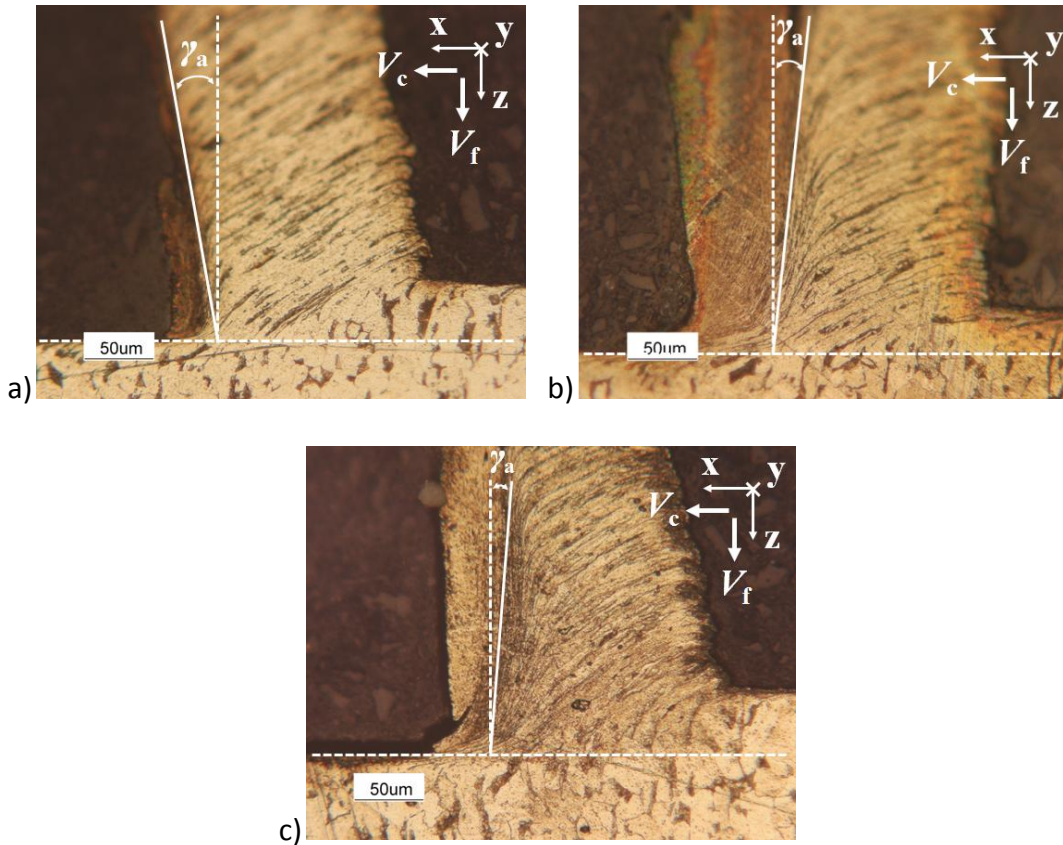
Figure 5.3. Quick stop tests results with  $V_c = 50 \text{ m/min}$ .







c)

Figure 5.4. Quick stop tests results with  $V_c = 75$  m/min.

a)

b)

c)

Figure 5.5. Quick stop tests results with  $V_c = 100$  m/min.

The chip micrographs depicted in Fig. 5.3, Fig. 5.4 and Fig. 5.5 show how built-up edge appears at all the tested  $V_c$  values even if its shape changes: at the lowest cutting speed  $V_c = 50$  m/min (Fig. 5.3) the apparent rake angle ( $\gamma_a$ ) seen

by the chip is definitely positive and comparable or even higher than the geometrical rake angle ( $\gamma$ ) of the tool;  $\gamma_a$  becomes slightly negative (Fig. 5.5) at the highest speed  $V_c = 100$  m/min and the workpiece is machined by a rake angle different from the geometrical one.

These are only preliminary observations which should be further studied but already point out that the QSD is a powerful instrument for studying the chip formation phenomena in the microscale and giving an empirical proof to analytical or numerical models.

As mentioned in Section 1.1, several studies claim that a stable built-up edge is present when machining in the microscale: it can be very interesting to experimentally prove this assumption by means of micrographs as Kountanya et al. did (see Fig. 1.12). The advantage of carrying out frozen cut experiments by means of the micro QSD is that it allows to provide each micrograph with the conditions under which it has been obtained, this way validating the obtained results.

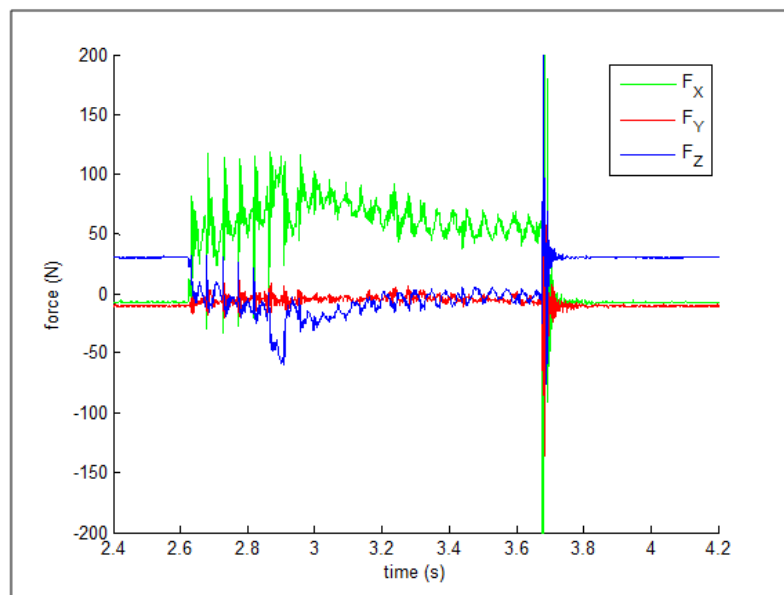


Figure 5.6. Example of cutting forces measurements during a quick stop tests with  $V_c = 50$  m/min.

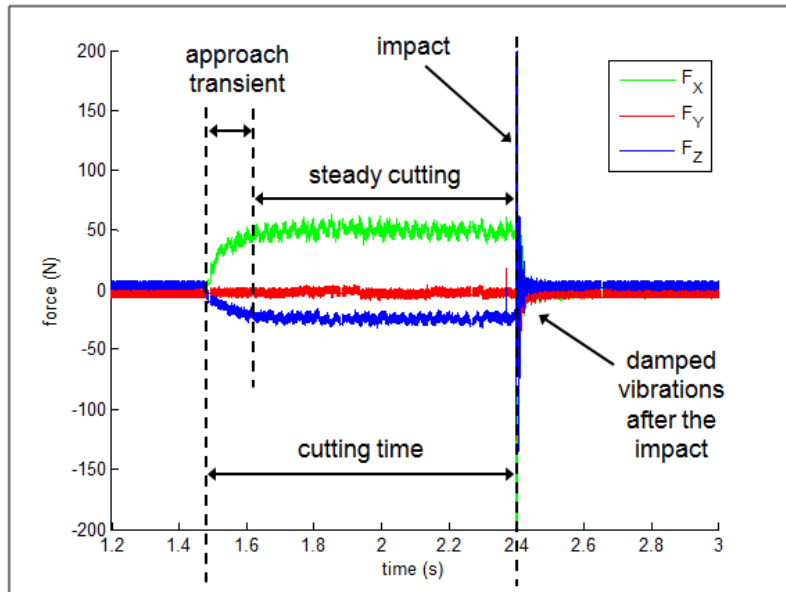


Figure 5.7. Example of cutting forces measurements during a quick stop tests with  $V_c = 75$  m/min.

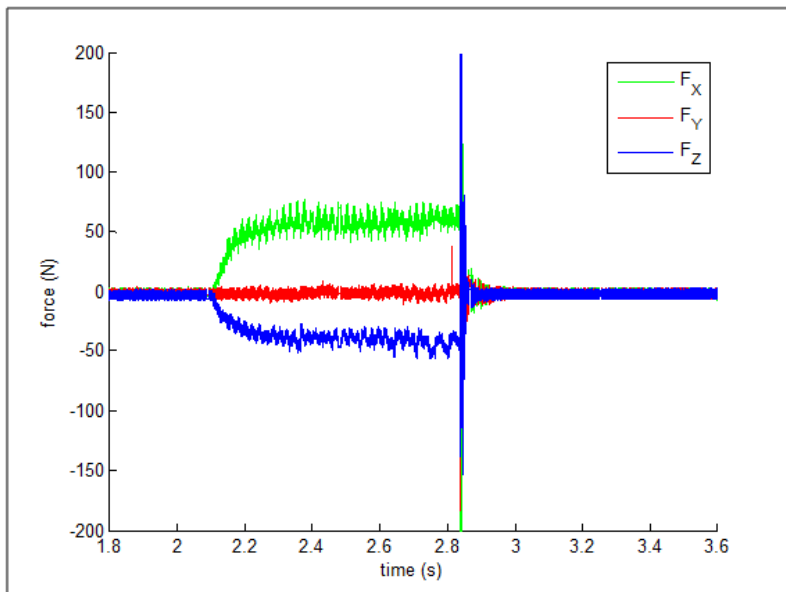


Figure 5.8. Example of cutting forces measurements during a quick stop tests with  $V_c = 100$  m/min.

Other information on chip formation can be obtained from the cutting forces measurement made during the quick stop tests, whose results are shown in the graphs of Fig. 5.6, Fig. 5.7 and Fig. 5.8 (note that even if the times on the



abscissa are different, the interval taken into account has the same length so it is possible to compare the tests duration).

The cutting force signals can be used for performing a diagnosis of the quick stop experiment: first of all, it is possible to point out that the test is really carried out in an orthogonal cutting condition if the  $F_y$  signal mean is close to zero (as it is in Fig. 5.6, Fig. 5.7 and Fig. 5.8). Also information about the stability of the cutting action can be drawn from the force graph; for example, large vibrations can be seen in Fig. 5.6 and this fact may be due to an unstable chip formation, which may also be the cause of the wavy form of the chip (picture a) in Fig. 5.3).

The relationship between cutting forces and phenomena connected with the chip formation has to be further studied, since only preliminary experiments have been performed, but the above outlined considerations show how the micro QSD can be an effective instrument also for this purpose and again can help in confirming the statements resulting from analytical or numerical modelling.



## Conclusions and future developments

In the present work a new quick-stop device (QSD) to carry out frozen cut experiments within the typical microscale cutting requirements has been designed. This device should overcome the drawbacks of the existing QSDs, have a good repeatability and fulfil safety rules; experimental results reported in this study demonstrate how all these objectives have been achieved.

*Ad hoc* sensors and analysis procedures have been designed in the present work in order to fully characterize the QSD in terms of performance. Experimental results show that the quick-stop device fits the design specifics and that each frozen cut test can be validated by means of online measurements.

Since the micro QSD has been characterized, it is possible to use it for improving the chip formation knowledge in the microscale. This can be done by carrying out experimental campaigns with the aim of studying the effect of several parameters, e.g. :

- tool material,
- tool geometry,
- tool coating,
- lubrication conditions,
- cutting parameters,

on some cutting process output, such as:

- cutting forces,
- roughness,
- built-up edge.

This way, the proposed device can be an invaluable support to confirm the statements resulting from analytical or numerical modelling; moreover, as concerning practical applications, quick-stop experiments can be exploited by industries for improving tools or process productivity.



## Appendix A

### Program for evaluating the expected striker speed at the impact $V_{imp}$ basing on the air pressure inside the cylinder $P_{air}$

The program shown in this Appendix has been built by means of Matlab® R2011b (Version 7.13) software to evaluate the expected striker speed at the impact  $V_{imp}$  basing on the air pressure inside the cylinder  $P_{air}$ . This program allows to correctly dimension the percussion system in order to achieve the desired performance.

The algorithm, which will be commented in detail, divides the piston stroke in several steps (Fig. A.1) and, for each one, calculates the air pressure inside the cylinder, the piston acceleration and its speed; the output of the last computation step is the expected striker speed at the impact  $V_{imp}$ .

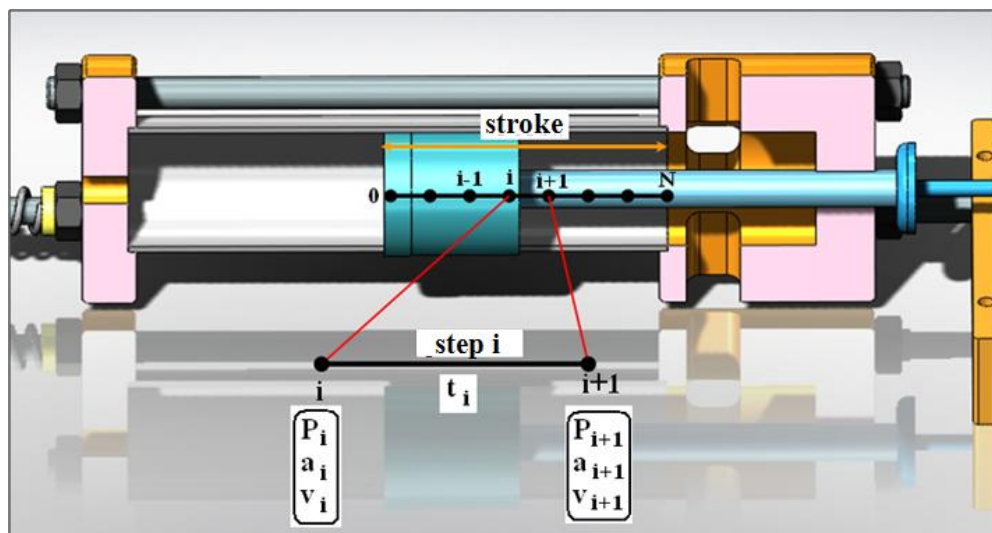


Figure A.1. Piston stroke discretization.

Both the situation in which the air pressure inside the cylinder  $P_{air}$  decreases when the piston volume increases (close air inlet valve case) and the situation in which  $P_{air}$  keeps constant due to an infinite cylinder volume (open air inlet valve case) are taken into account (see Section 3.2.2). Quantities referring to

the first situation have subscript 1 and quantities referring to the second situation have subscript 2.

It should be noticed that the program also allows to compare the  $V_{imp}$  measurement made by the electronic system described in Section 4.3.1 to the theoretical target values.

```
% % % % % % % % % % % % % % % % % % % % % % % % % % % % % % % % % %
```

Preliminary operations:

```
close all
clear all
clc
```

Piston stroke length:

```
L=90;      %[mm]
```

Piston diameter:

```
Dp=50;     %[mm]
```

Piston mass:

```
M=0.2263;  %[kg]
```

Initial length of cylinder back chamber:

```
X0=0.073;  %[m]
```

Piston area:

```
Ap=pi*(Dp*10^-3)^2/4;  %[m^2]
```

Initial volume of cylinder back chamber:

```
V0=Ap*X0+0.042*(pi*(0.042^2)/4);  %[m^3]
```

Initial pressure inside the back chamber:

```
P0=[0:0.1:10];  %[bar]
```

Temperature:

```
T=295;        %[K]
```

Perfect gas constant:

```
R=0.287;      %[kJ/kg°K]
```

**Calculation step definition:**

```

passo=0.05;      % [mm]
N=L/passo;
x=[0:passo:L];

```

**Springs stiffness:**

```

K=17.67;        % [N/mm]
K=K*1000;

```

**Cylinder mass:**

```

m_cil=6;        % [kg]

```

**Cycle for evaluating different pressures:**

```

for k=1:length(P0)

```

**Calculation of initial force, striker speed and acceleration, spring compression:**

```

    F1(1)=10^5*P0(k)*Ap^0.6;      % [N]
    F2(1)=10^5*P0(k)*Ap^0.6;
    a1(1)=F1(1)/M;
    a2(1)=F2(1)/M;
    v1(1)=0;
    v2(1)=0;
    m=P0(k)*10^5*V0/(R*10^3*T);
    vp1(1)=M/m_cil*v1(1);
    vp2(1)=M/m_cil*v2(1);
    DeltaL1(1)=sqrt(m_cil/K)*vp1(1);      % [m]
    DeltaL2(1)=sqrt(m_cil/K)*vp2(1);
    DeltaDL1(1)=DeltaL1(1);
    DeltaDL2(1)=DeltaL2(1);
    v_eff1(1)=v1(1);
    v_eff2(1)=v2(1);

```

**Cycle for calculation of initial force, striker speed and acceleration, spring compression in each step:**

```

    for i=1:N
        t1(i)=(-v1(i)+sqrt(v1(i)^2+4*a1(i)*passo*10^-3))/(2*a1(i));
        t2(i)=(-v2(i)+sqrt(v2(i)^2+4*a2(i)*passo*10^-3))/(2*a2(i));
        Vi=V0+i*passo*10^-3*Ap;
        Pi1=m*R*10^3*T/Vi;
        Pi2=P0(k);
        F1(i+1)=Pi1*Ap^0.6;
        F2(i+1)=Pi2*Ap^0.6*10^5;
    end

```

```

a1(i+1)=F1(i+1)/M;
a2(i+1)=F2(i+1)/M;
v1(i+1)=passo*10^-3/t1(i);
v2(i+1)=passo*10^-3/t2(i);
DeltaDL1(i+1)=0;
DeltaDL2(i+1)=0;
v_eff1(i+1)=v1(i+1)-DeltaDL1(i+1)/t1(i);
v_eff2(i+1)=v2(i+1)-DeltaDL2(i+1)/t2(i);
end

```

**Striker speed at the impact:**

```

V_eff1(k)=max(v_eff1);
V_eff2(k)=max(v_eff2);
end

```

**Uploading and arranging of the measurement results of striker speed at the impact:**

```

[nome path]=uigetfile('*.txt','scegli il file da aprire');
cd(path);
dati=load(nome);

[r c]=size(nome);
pressione=dati(:,1)/10;
velocita=dati(:,2);

```

**Target striker speed at the impact:**

```
target=18.4*ones(length(P0));
```

**Results graphical representation (Fig. A.2):**

```

P0=P0/10;    %[MPa]

figure(1)
plot(pressione,velocita, '.');
hold all;
box on;
plot(P0,V_eff1,'k--', 'LineWidth', 1.5);
plot(P0,V_eff2,'k:', 'LineWidth', 1.5);
plot(P0,target, 'r', 'LineWidth', 1.5);
xlabel('P_{air} (MPa)');
ylabel('V_{imp} (m/s)');
legend('test result', 'theoretical - variable
P_{air}', 'theoretical - constant P_{air}');

```



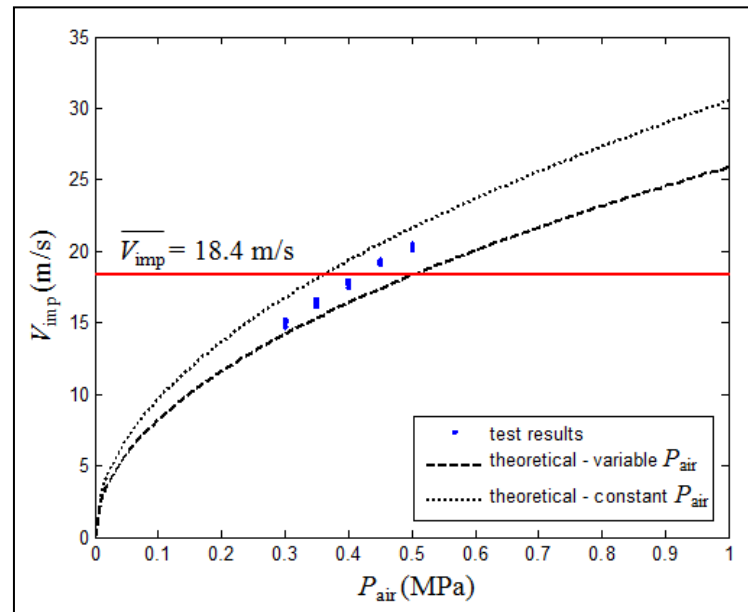


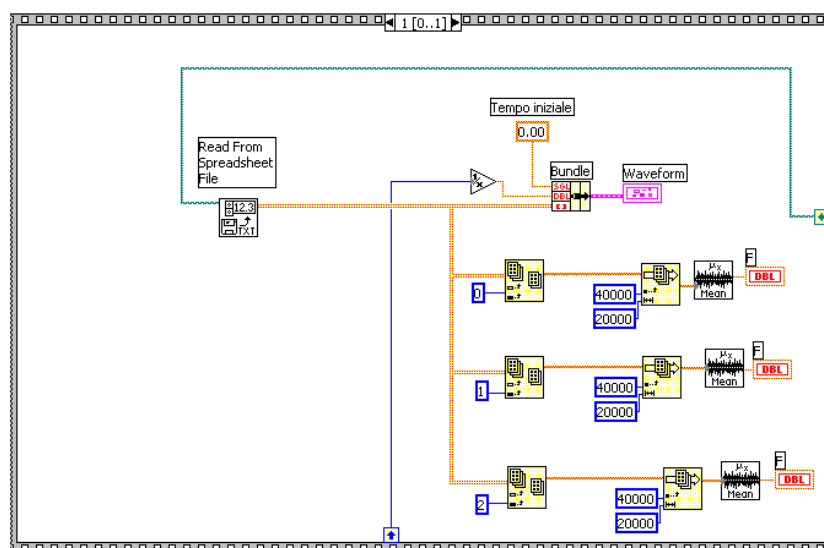
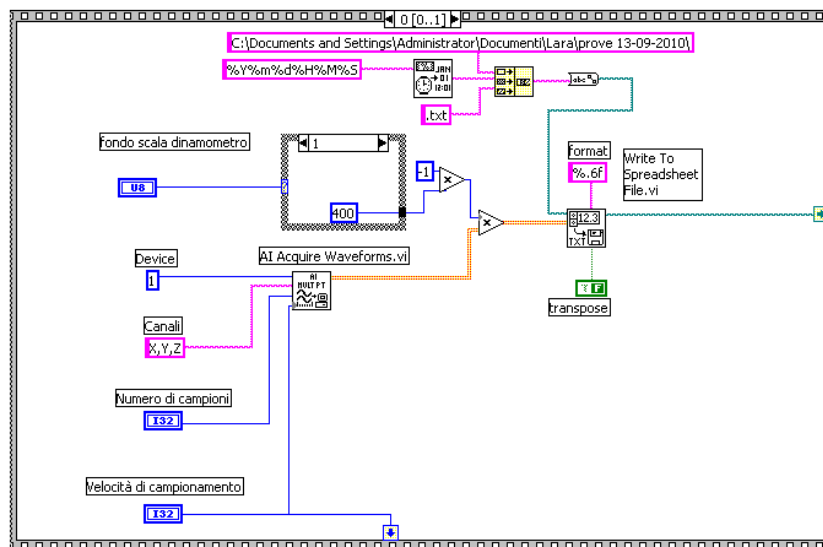
Figure A.2. Results of  $V_{imp}$  measurement (blue) and expected striker speed at the impact  $V_{imp}$ .



## Appendix B

### Program for acquiring cutting forces

The following screenshots show the details of the LabVIEW® 2010 program developed for acquiring the cutting force signals while performing quick-stop experiments.





## Appendix C

### Program for managing quick-stop experiments

The following screenshots show the details of the LabVIEW® 2010 program developed for managing quick-stop experiments via the electronic system built for this purpose (see Section 3.2.3), whose circuit schematics is represented at the end of this Appendix in Fig. C.2.

The program, whose graphical interface is shown in Fig. C.1, is made up by the loops depicted below together with a brief description.

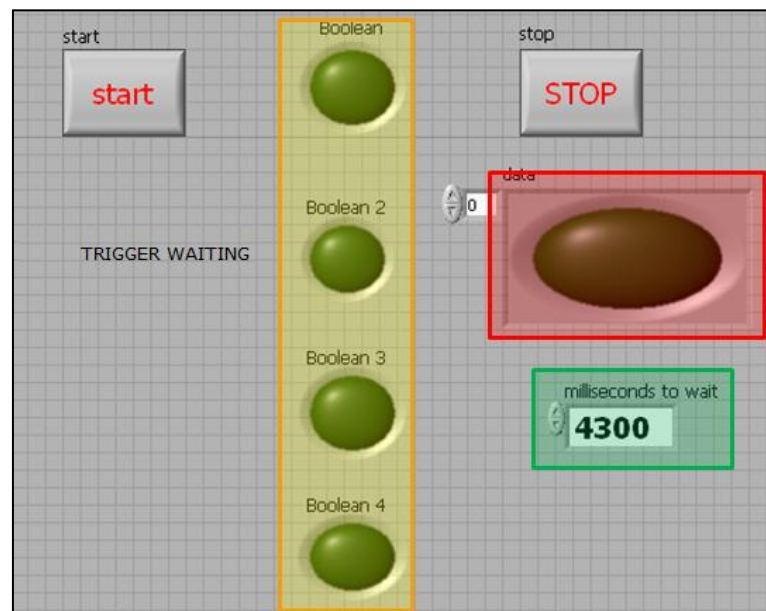
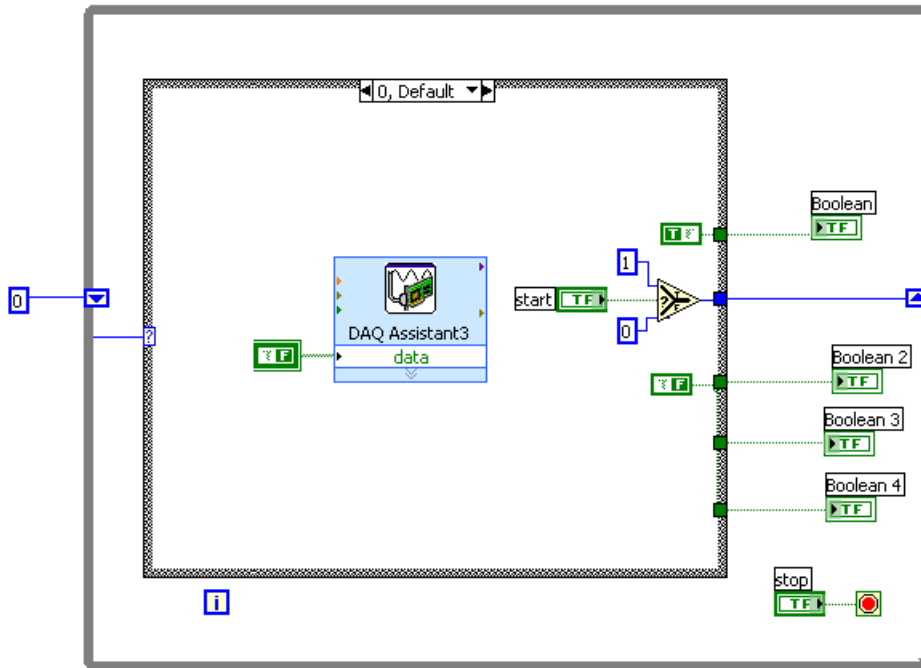


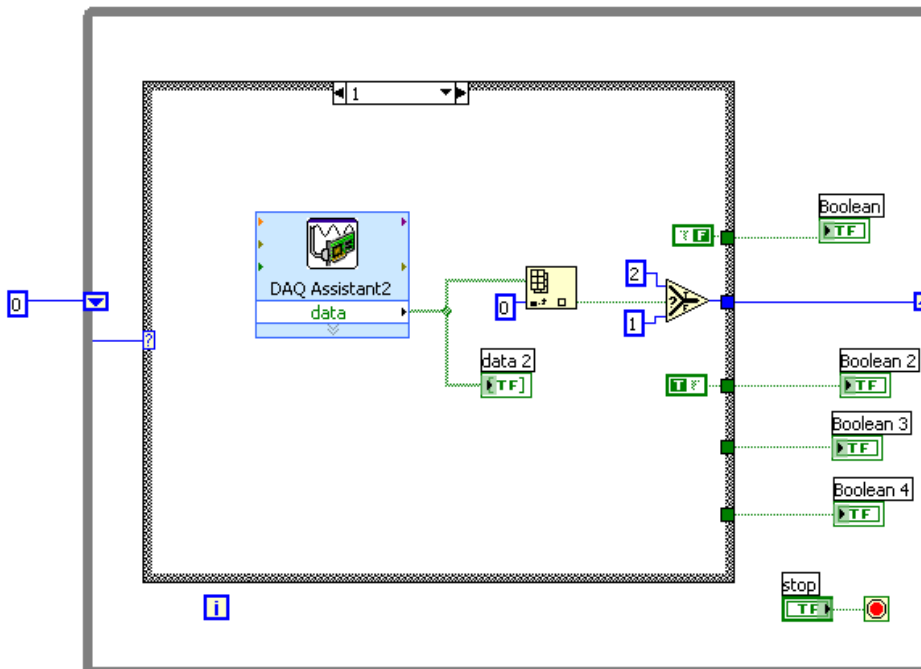
Figure C.1. Program graphical interface.

In the interface the green indicators show the different test phases, the red indicator (highlighted in red in Fig. C.1) reports the tool-workpiece contact and the counter (highlighted in green in Fig. C.1) is used to set the required duration of the orthogonal cutting operation.

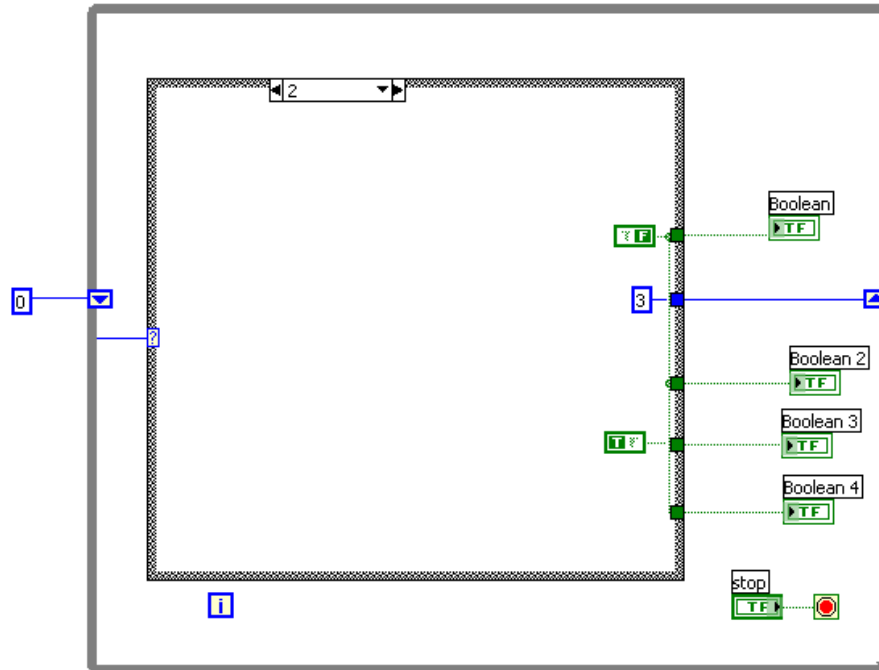
Loop 0 → Waiting for the operator start.



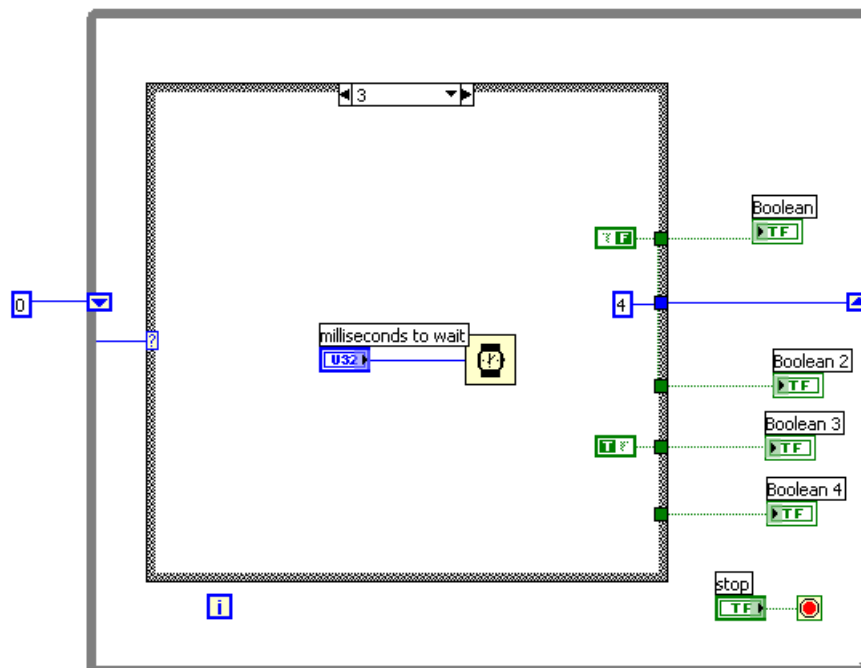
Loop 1 → Waiting for trigger signal (tool-workpiece contact beginning).



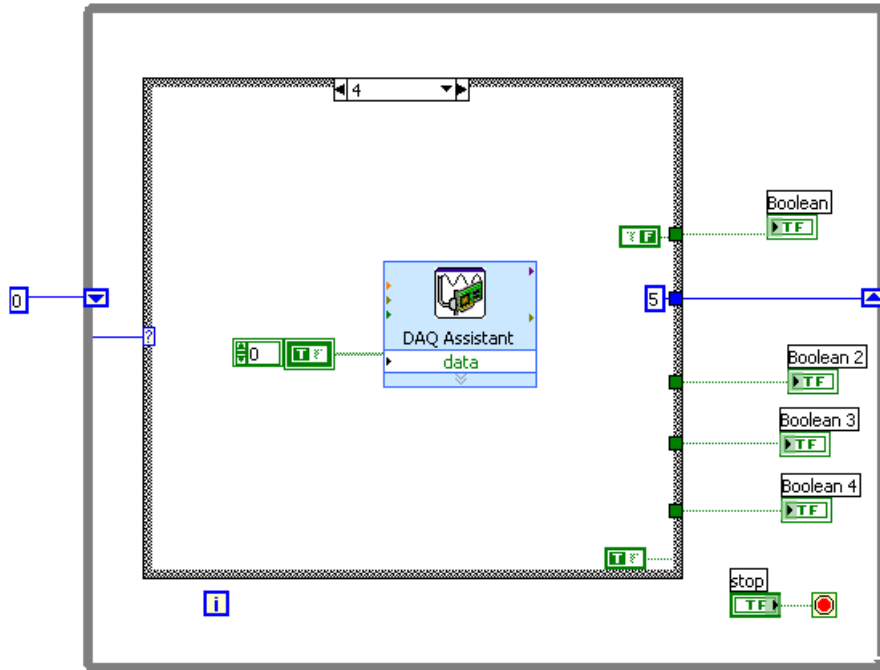
Loop 2 → Light indicators setting.



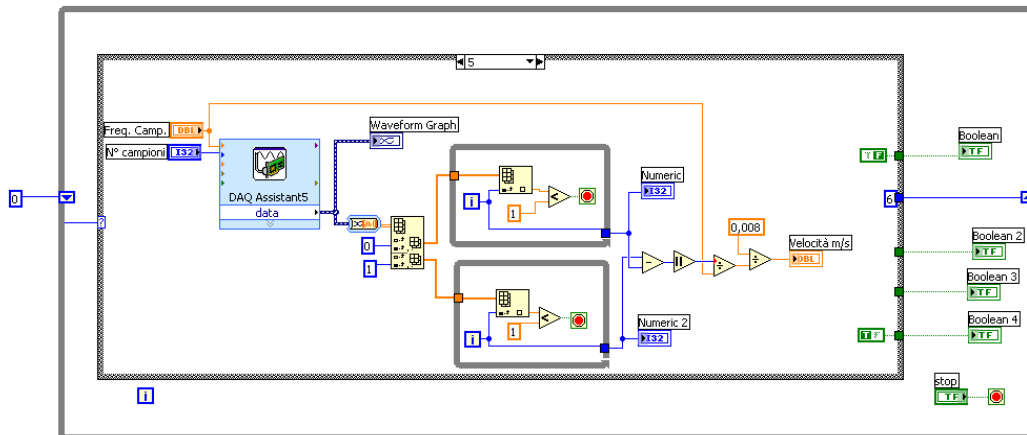
Loop 3 → Waiting for turning operation.



Loop 4 → Solenoid activation.

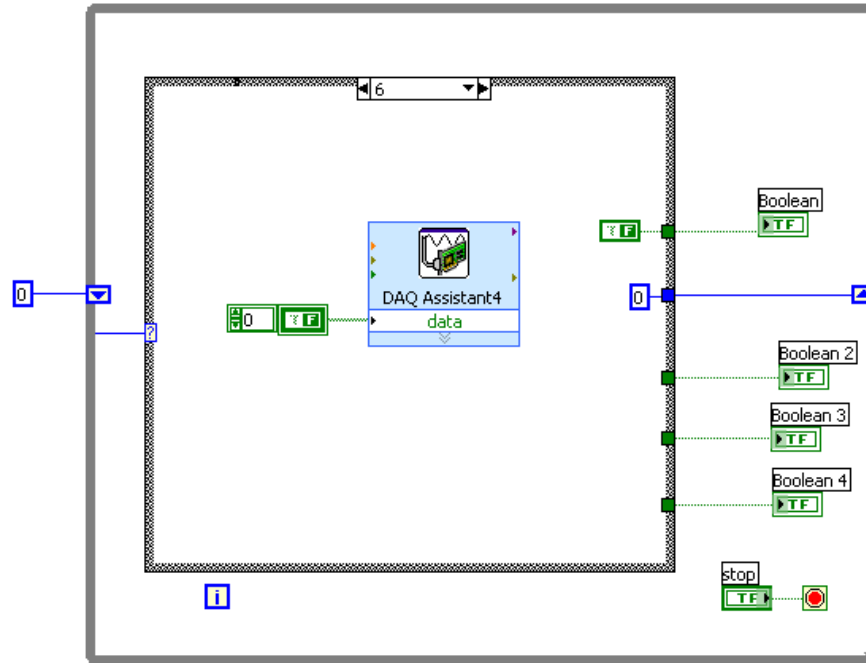


Loop 5 → Striker impact speed measurement.





Loop 6 → Program end and indicators reset.



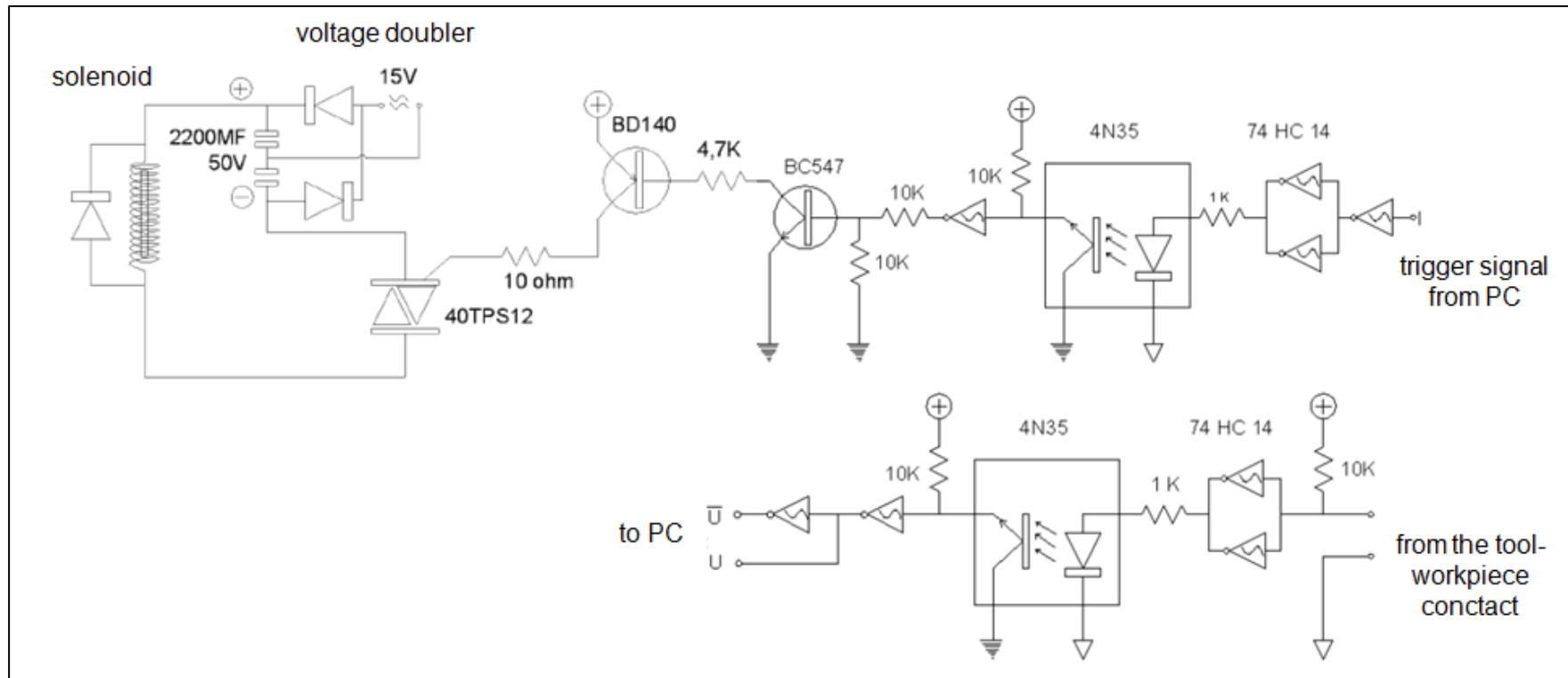


Figure C.2. Electronic circuit schematics.

## Appendix D

### Electronic circuit schematics of angular position sensors

The following pictures depicts the electronic circuit schematics of the two angular position sensors designed in the present study and whose operation is described in Section 4.4.1.

Fig. D.1 refers to the amplifier circuit for the two receiving diodes of the laser triangulation sensor while Fig. D.2 shows the amplifier circuit for the receiving diode of the polarizing filters sensor.

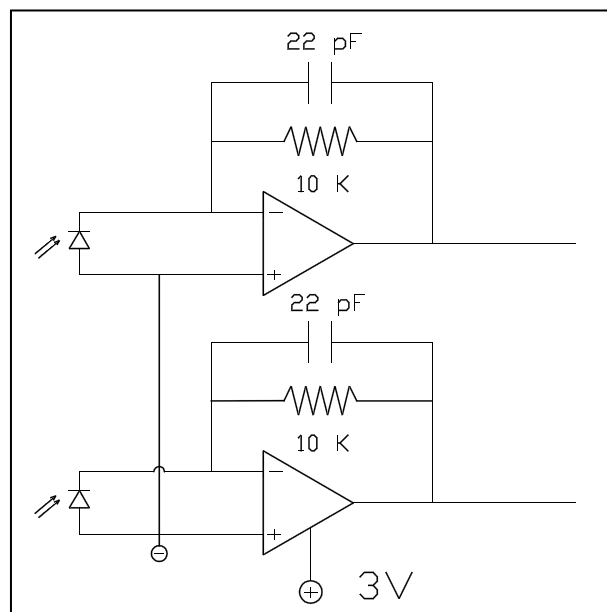


Figure D.1. Schematics of the amplifier circuit of the laser triangulation sensor.

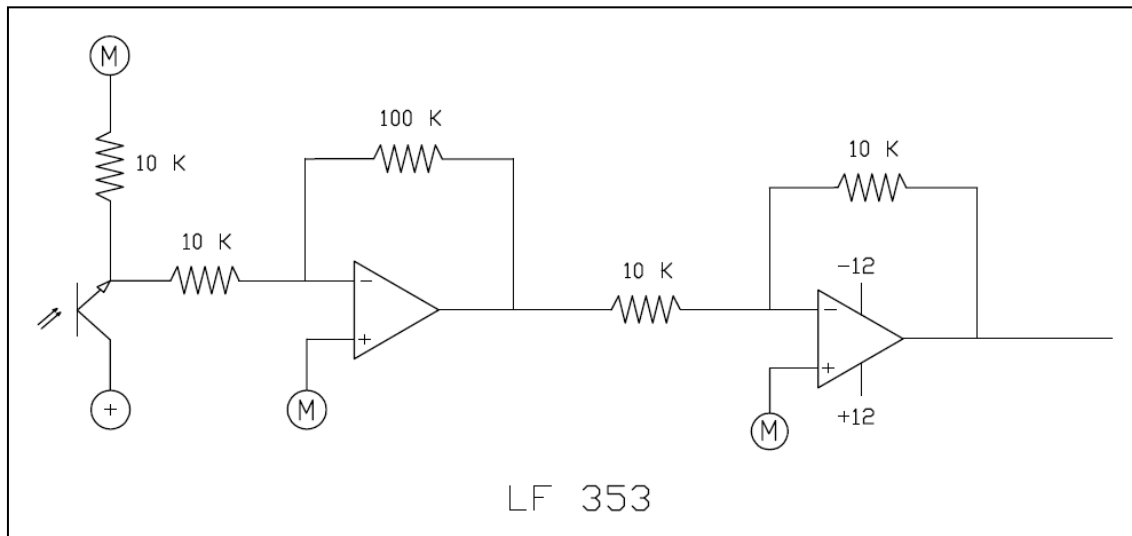


Figure D.2. Schematics of the amplifier circuit of the polarizing filters sensor.

## Appendix E

### Program for analyzing signals acquired by angular position sensors

The following program has been built by means of R<sup>®</sup> 2.8.1 software in order to analyze the signal acquired by both the angular position sensors built within the present study.

The program, which will be commented in detail, performs the following operations:

- it smooths the signal irregularity (by means of the local regression method, using the “locfit” package [70]);
- it numerically derives the angular position signal in order to obtain the angular speed (by means of the finite differences method [71]);
- it transforms the angular speed to the peripheral one;
- it projects the speed value on the horizontal direction;
- it identifies the time when the tool-workpiece separation starts and ends;
- it calculates the distance covered by the tool  $d_t$  by numerically integrating the speed signal between the above limits (this interval corresponds to the separation time  $t_s$ );
- it calculates the separation distance  $d_s$ .

```
% % % % % % % % % % % % % % % % % % % % % % % % % % % % % % % % % % %
```

Preliminary operations:

```
graphics.off()
rm(list=ls())
library(locfit)
library(caTools)
```

Data uploading and arranging:

```
dati <- read.table('prova_1_dati.txt',header=F,sep="")

x <- dati[,1]      %[s]
y <- dati[,2]      %[°]

n <- length(x)
h <- x[2]-x[1]
```

Reference cutting speed:

```
v_cut <- 100    %[m/min]
v_cut_sec <- v_cut/60    %[m/s]
soglia <- v_cut*0.05
```

Measured striker impact speed in the considered test:

```
v_t_x <- 417    %[m/min]
```

Angular displacement the tool needs to exit from the cutting area:

```
ang_s <- 0.52    %[°]
```

Polynomial degree for calculating moving average:

```
grado <- 0
```

Optimal span length:

```
alfa_ott_cv <- 0.1
```

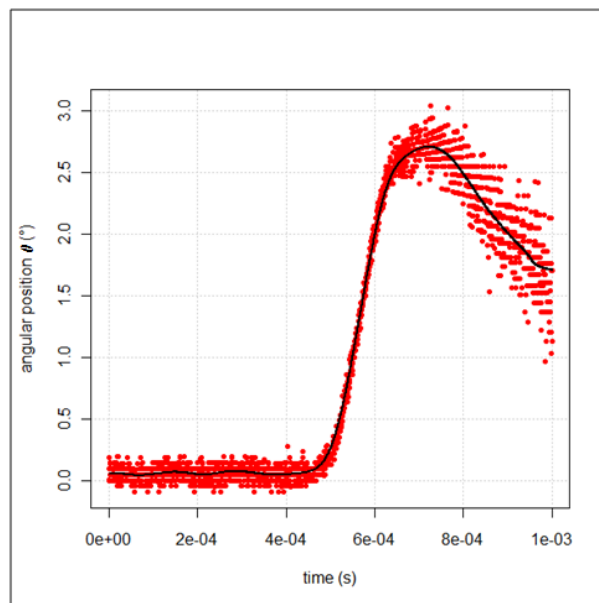


Figure E.1. Original data (red) and moving average result (black).

Smoothing of the angular position signal (Fig. E.1):

```
windows()
plot(x,y, xlab='time (s)', ylab='angular position o (°)', lwd=1,
col='red', pch=20, grid())
```

```

y_fit <- locfit.raw(x, y, alpha=alfa_ott_cv, deg=grado,
ev=dat())
y_smooth <- predict(y_fit)
lines(x, y_smooth, lwd=2, col='black')

```

Identification of the instant when tool exits from the cutting area:

```

separazione_ang <- 0
for (f in 1:n)
{
  if (y_smooth[f] > ang_s)
  {
    separazione_ang <- f
    break
  }
}

```

Derivation of the smooth angular position signal:

```

v <- rep(0,n)
for (k in 1:n)
{
  if (k < 4)
    v[k] <- (-147*y_smooth[k]+360*y_smooth[k+1]-
450*y_smooth[k+2]+400*y_smooth[k+3]-
225*y_smooth[k+4]+72*y_smooth[k+5]-10*y_smooth[k+6]) / (60*h)
  else
  {
    if (k > n-3)
      v[k] <- (147*y_smooth[k]-360*y_smooth[k-
1]+450*y_smooth[k-2]-400*y_smooth[k-3]+225*y_smooth[k-4]-
72*y_smooth[k-5]+10*y_smooth[k-6]) / (60*h)
    else
      v[k] <- (-y_smooth[k-3]+9*y_smooth[k-2]-
45*y_smooth[k-1]+45*y_smooth[k+1]-
9*y_smooth[k+2]+y_smooth[k+3]) / (60*h)
  }
}

```

Geometrical data about tool holder:

```

r <- 0.0237    %[m]
beta <- 0.483  %[°]

```

Calculation of the horizontal component of peripheral speed:

```

omega <- v*2*pi/360
v_x <- omega*r*cos(beta)*60

```

Identification of the instant when tool-workpiece separation starts and finishes:

```
separazione <- 1
origine <- 1

for (ii in 1:n)
{
  if (v_x[ii] > v_cut)
  {
    separazione <- ii
    break
  }
}

for (iii in 1:separazione)
{
  if (v_x[iii+1]-v_x[iii] < 0)
    origine <- iii+1
}

```

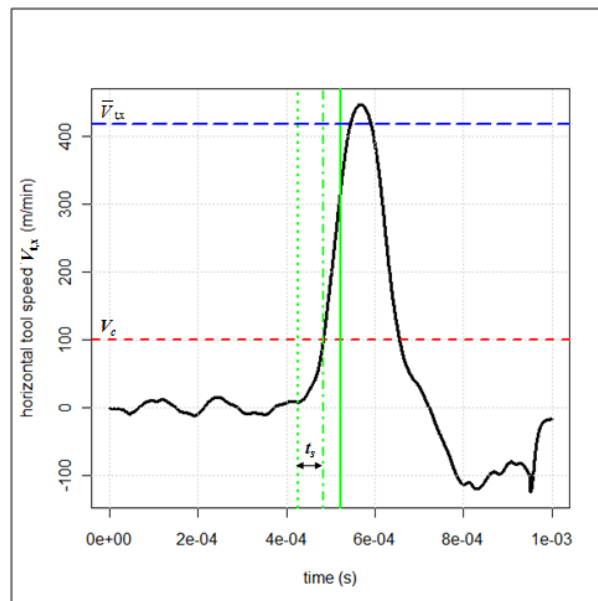


Figure E.2. Horizontal tool speed (black), cutting speed (dashed red), tool-workpiece separation beginning (dotted green) and end (dot-dashed green), tool exit from the uncut chip thickness (solid green), expected horizontal tool speed (long-dashed blue).



**Results graphical representation (Fig. E.2):**

```
windows()
plot(x,v_x, xlab='time (s)', ylab='horizontal tool speed Vt,x
(m/min)', type='l', lwd=3, col='black')
lines(grid())
abline(h=v_cut, lty=2, lwd=2, col='red')
abline(h=v_t_x, lwd=2, lty=5, col='blue')
abline(v=x[separazione_ang], lwd=2, col='green')
abline(v=x[separazione], lty=4, lwd=2, col='green')
abline(v=x[origine], lty=3, lwd=2, col='green')
```

**Calculation of the separation time:**

```
t_s <- x[separazione]-x[origine]    %[s]
```

**Integration of the horizontal speed signal (calculation of the distance covered by the tool):**

```
x_int <- x[origine:separazione]-x[origine]
v_int <- v_x[origine:separazione]/60
```

```
d_t <- trapz(x_int, v_int)    %[m]
```

**Calculation of the distance covered by the workpiece:**

```
d_w <- v_cut_sec*t_s    %[m]
```

**Calculation of the separation distance:**

```
d_s <- (d_w-d_t)    %[m]
```

**Results visualization:**

```
t_s*(10^6)    %[\u00b5s]
d_s*(10^6)    %[\u00b5m]
```



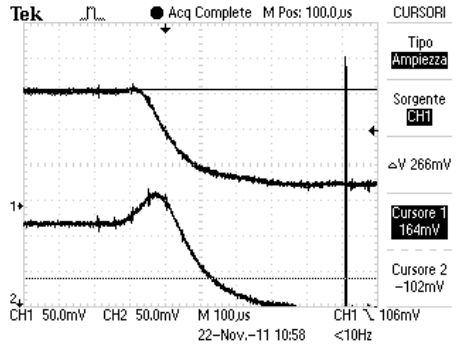
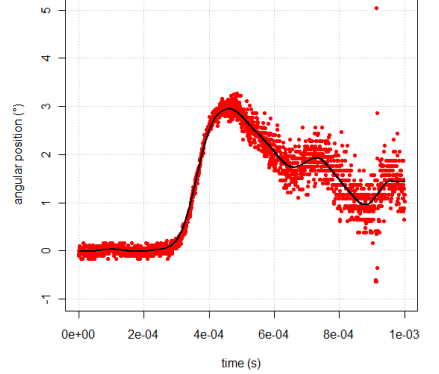
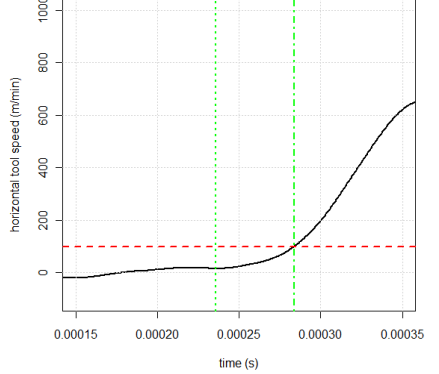
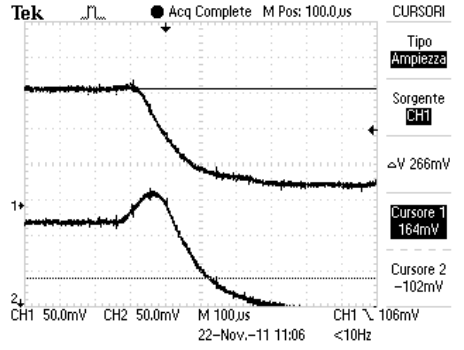
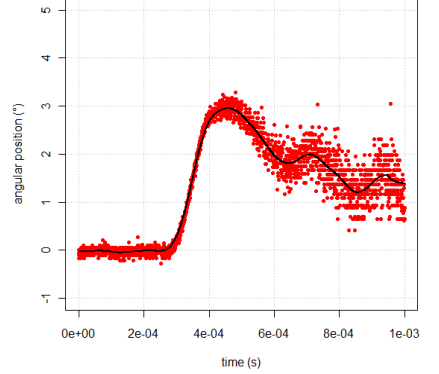
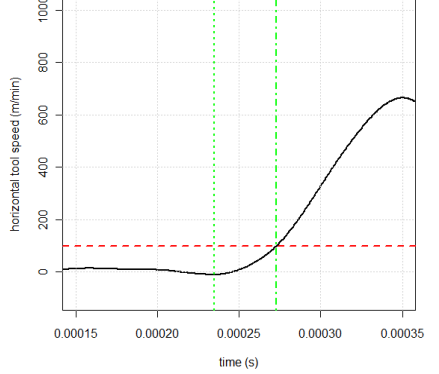
## Appendix F

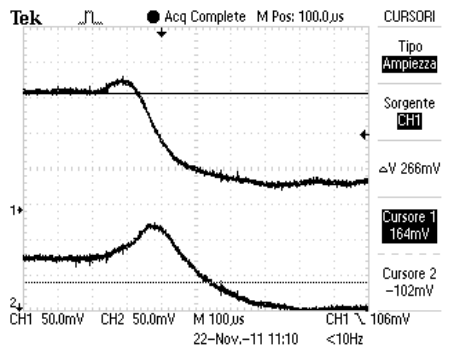
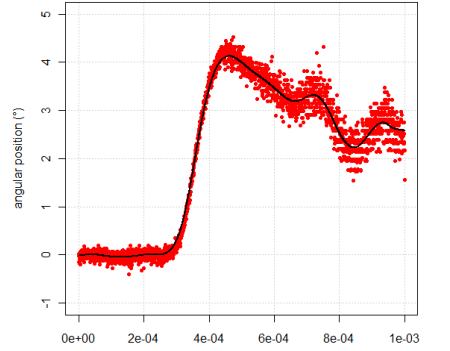
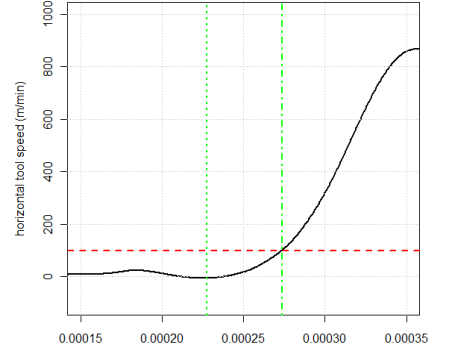
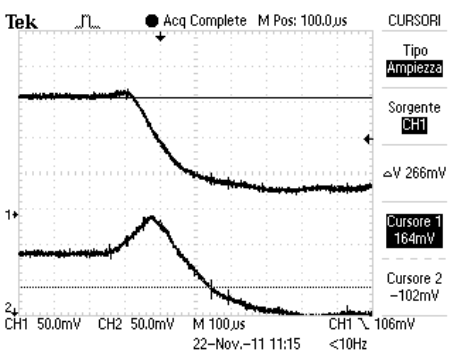
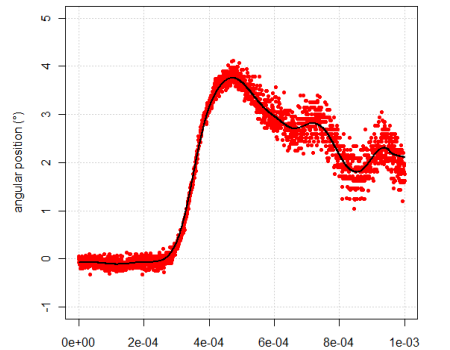
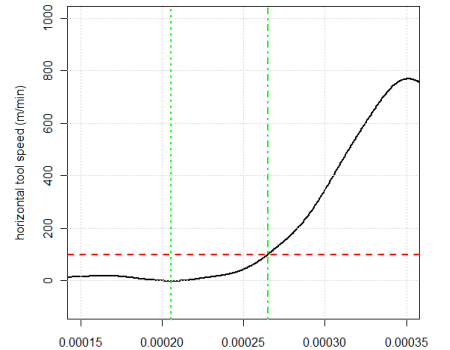
### Results of performance measurement campaigns

Here all the signals acquired during the four performance measurement campaigns (described in Section 4.4.3) are shown together with the results of their analysis.

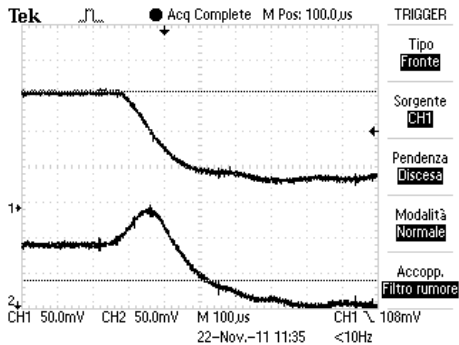
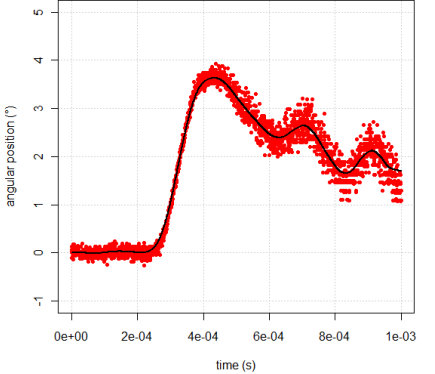
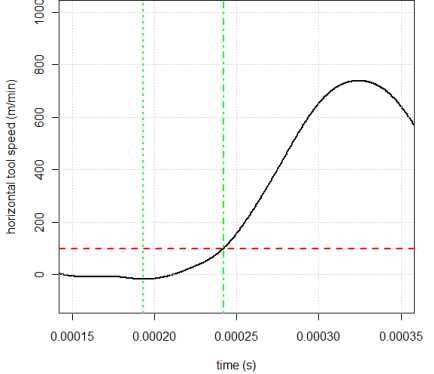
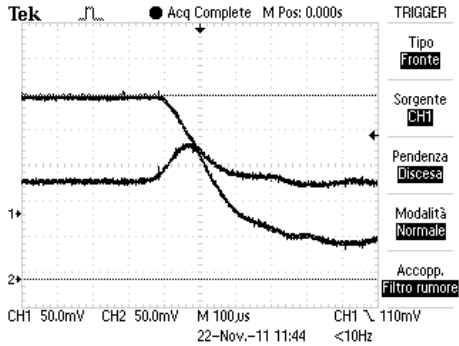
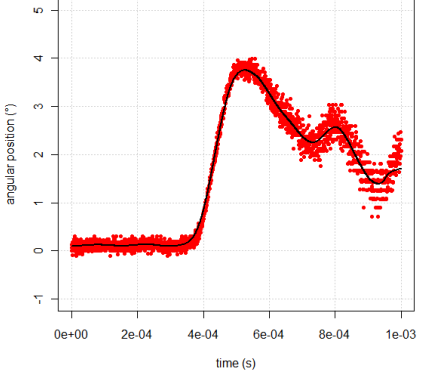
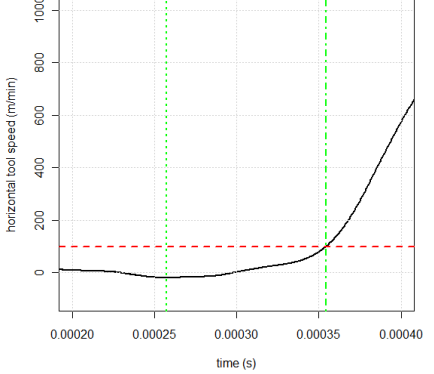
For sake of clarity, the graphs of the horizontal tool speed  $V_{t,x}$  have been zoomed in the region of interest, always considering the same time interval (even if the times on the abscissa are different) so it is possible to compare the duration of the tool-workpiece separation.

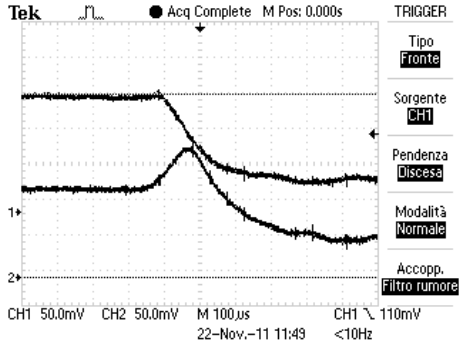
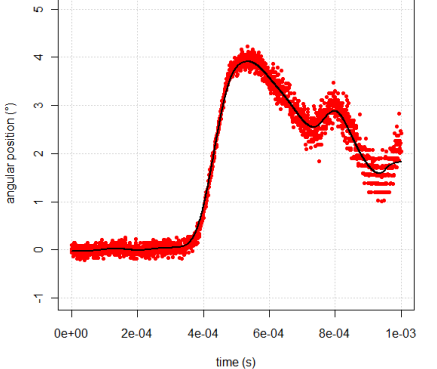
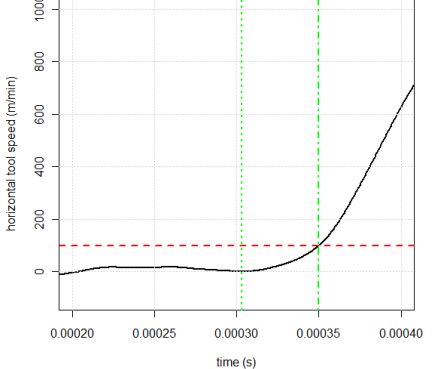
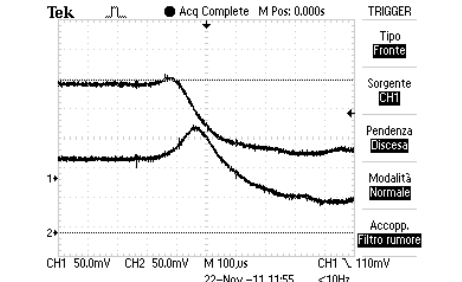
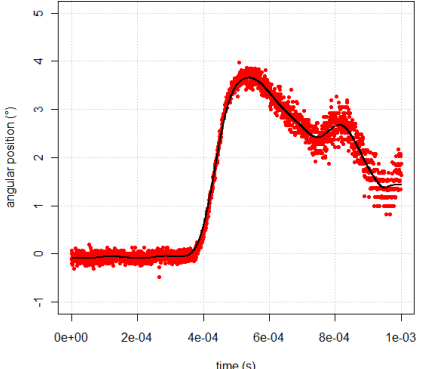
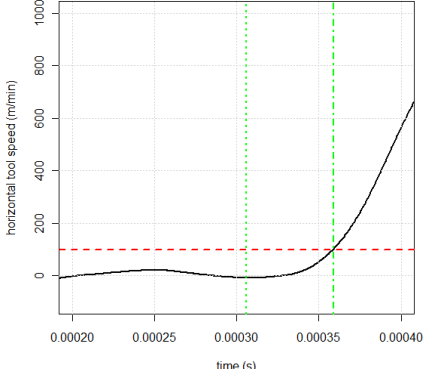
Table F.1. Acquisitions made by the laser triangulation sensor during the campaign with  $P_{\text{air}} = 0.2 \text{ MPa}$  and their analysis.

run order	oscilloscope acquisition	angular position	horizontal tool speed $V_{t,x}$ (detail)
1	 <p>Tek <span style="float:right">● Acq Complete M Pos: 100.0<math>\mu</math>s CURSORI</span></p> <p>Tipo <b>Ampiezza</b></p> <p>Sorgente <b>CH1</b></p> <p><math>\Delta V</math> 266mV</p> <p>Cursor 1 <b>164mV</b></p> <p>Cursor 2 <b>-102mV</b></p> <p>CH1 50.0mV CH2 50.0mV M 100<math>\mu</math>s CH1 106mV</p> <p>22-Nov.-11 10:58 &lt;10Hz</p>	 <p>angular position (°)</p> <p>time (s)</p>	 <p>horizontal tool speed (m/min)</p> <p>time (s)</p>
2	 <p>Tek <span style="float:right">● Acq Complete M Pos: 100.0<math>\mu</math>s CURSORI</span></p> <p>Tipo <b>Ampiezza</b></p> <p>Sorgente <b>CH1</b></p> <p><math>\Delta V</math> 266mV</p> <p>Cursor 1 <b>164mV</b></p> <p>Cursor 2 <b>-102mV</b></p> <p>CH1 50.0mV CH2 50.0mV M 100<math>\mu</math>s CH1 106mV</p> <p>22-Nov.-11 11:06 &lt;10Hz</p>	 <p>angular position (°)</p> <p>time (s)</p>	 <p>horizontal tool speed (m/min)</p> <p>time (s)</p>

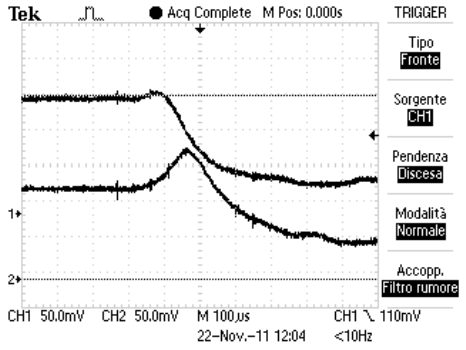
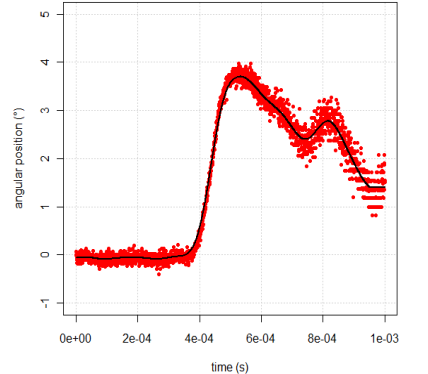
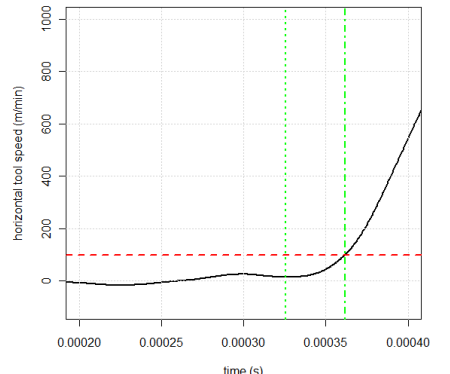
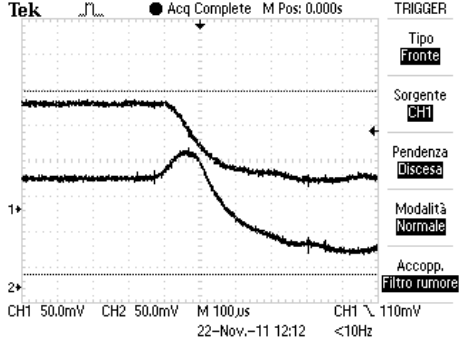
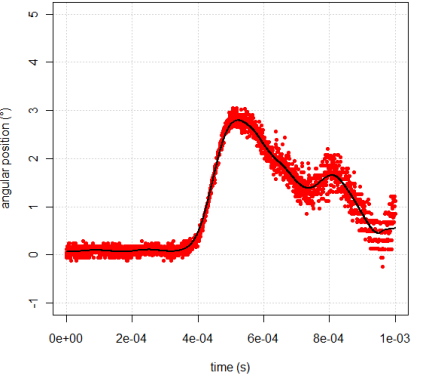
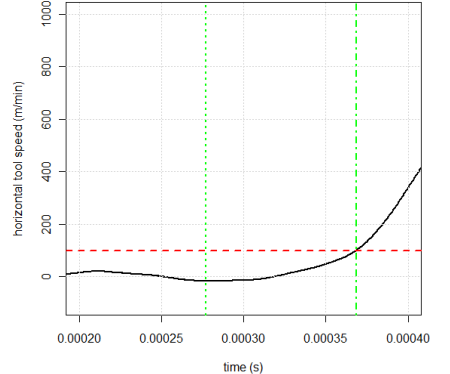
run order	oscilloscope acquisition	angular position	horizontal tool speed $V_{t,x}$ (detail)
3	 <p>Tek Acq Complete M Pos: 100.0us CURSORI      Tipo Ampiezza      Sorgente CH1  <math>\Delta V</math> 266mV      Cursore 1 164mV      Cursore 2 -102mV      CH1 50.0mV CH2 50.0mV M 100.0us CH1 106mV      22-Nov.-11 11:10 &lt;10Hz</p>	 <p>angular position (°)      time (s)</p>	 <p>horizontal tool speed (m/min)      time (s)</p>
4	 <p>Tek Acq Complete M Pos: 100.0us CURSORI      Tipo Ampiezza      Sorgente CH1  <math>\Delta V</math> 266mV      Cursore 1 164mV      Cursore 2 -102mV      CH1 50.0mV CH2 50.0mV M 100.0us CH1 106mV      22-Nov.-11 11:15 &lt;10Hz</p>	 <p>angular position (°)      time (s)</p>	 <p>horizontal tool speed (m/min)      time (s)</p>

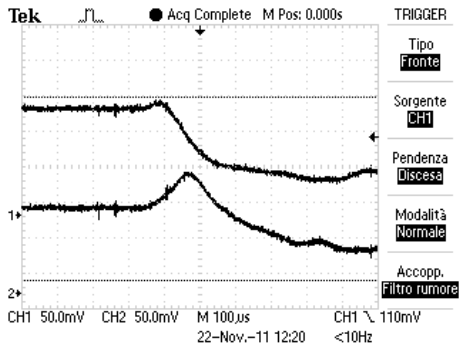
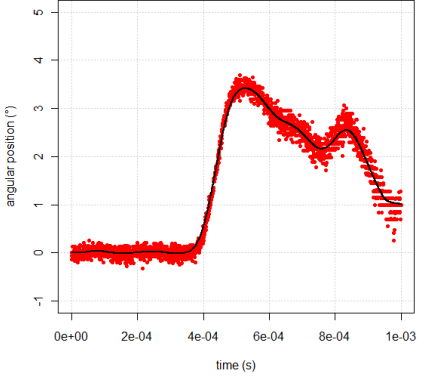
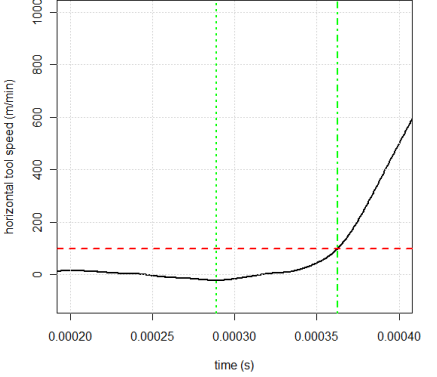
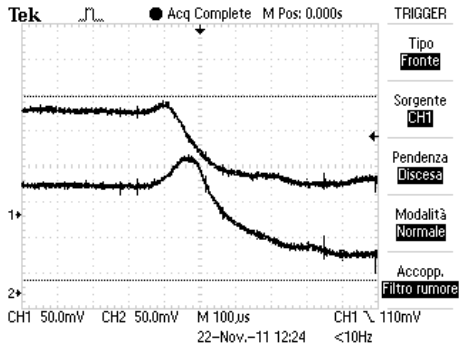
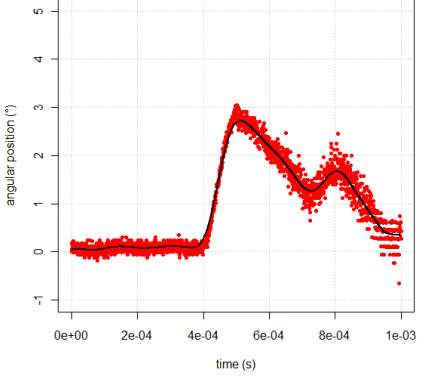
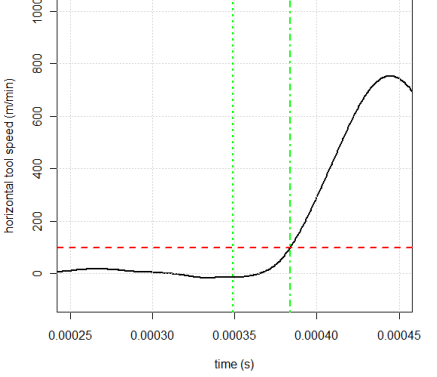
run order	oscilloscope acquisition	angular position	horizontal tool speed $V_{t,x}$ (detail)
5			
6			

run order	oscilloscope acquisition	angular position	horizontal tool speed $V_{t,x}$ (detail)
7	 <p>Tek <math>\mu</math>s Acq Complete M Pos: 100.0 <math>\mu</math>s TRIGGER</p> <p>Tipo Fronte</p> <p>Sorgente CH1</p> <p>Pendenza Discesa</p> <p>Modalità Normale</p> <p>Accopp. Filtro rumore</p> <p>CH1 50.0mV CH2 50.0mV M 100. <math>\mu</math>s CH1 108mV</p> <p>22-Nov.-11 11:35 &lt;10Hz</p>	 <p>angular position (°)</p> <p>time (s)</p>	 <p>horizontal tool speed (m/min)</p> <p>time (s)</p>
8	 <p>Tek <math>\mu</math>s Acq Complete M Pos: 0.000s TRIGGER</p> <p>Tipo Fronte</p> <p>Sorgente CH1</p> <p>Pendenza Discesa</p> <p>Modalità Normale</p> <p>Accopp. Filtro rumore</p> <p>CH1 50.0mV CH2 50.0mV M 100. <math>\mu</math>s CH1 110mV</p> <p>22-Nov.-11 11:44 &lt;10Hz</p>	 <p>angular position (°)</p> <p>time (s)</p>	 <p>horizontal tool speed (m/min)</p> <p>time (s)</p>

run order	oscilloscope acquisition	angular position	horizontal tool speed $V_{t,x}$ (detail)
9	 <p>Tek <math>\mu</math>L Acq Complete M Pos: 0.000s TRIGGER</p> <p>Tipo Fronte</p> <p>Sorgente CH1</p> <p>Pendenza Discesa</p> <p>Modalità Normale</p> <p>Accopp. Filtro rumore</p> <p>CH1 50.0mV CH2 50.0mV M 100.0us CH3 110mV</p> <p>22-Nov.-11 11:43 &lt;10Hz</p>	 <p>angular position (°)</p> <p>time (s)</p>	 <p>horizontal tool speed (m/min)</p> <p>time (s)</p>
10	 <p>Tek <math>\mu</math>L Acq Complete M Pos: 0.000s TRIGGER</p> <p>Tipo Fronte</p> <p>Sorgente CH1</p> <p>Pendenza Discesa</p> <p>Modalità Normale</p> <p>Accopp. Filtro rumore</p> <p>CH1 50.0mV CH2 50.0mV M 100.0us CH3 110mV</p> <p>22-Nov.-11 11:55 &lt;10Hz</p>	 <p>angular position (°)</p> <p>time (s)</p>	 <p>horizontal tool speed (m/min)</p> <p>time (s)</p>



run order	oscilloscope acquisition	angular position	horizontal tool speed $V_{t,x}$ (detail)
11	 <p>Tek Acq Complete M Pos: 0.000s</p> <p>TRIGGER</p> <p>Tipo Fronte</p> <p>Sorgente CH1</p> <p>Pendenza Discesa</p> <p>Modalità Normale</p> <p>Accopp. Filtro rumore</p> <p>CH1 50.0mV CH2 50.0mV M 100.µs CH1 110mV</p> <p>22-Nov.-11 12:04 &lt;10Hz</p>	 <p>angular position (°)</p> <p>time (s)</p>	 <p>horizontal tool speed (m/min)</p> <p>time (s)</p>
12	 <p>Tek Acq Complete M Pos: 0.000s</p> <p>TRIGGER</p> <p>Tipo Fronte</p> <p>Sorgente CH1</p> <p>Pendenza Discesa</p> <p>Modalità Normale</p> <p>Accopp. Filtro rumore</p> <p>CH1 50.0mV CH2 50.0mV M 100.µs CH1 110mV</p> <p>22-Nov.-11 12:12 &lt;10Hz</p>	 <p>angular position (°)</p> <p>time (s)</p>	 <p>horizontal tool speed (m/min)</p> <p>time (s)</p>

run order	oscilloscope acquisition	angular position	horizontal tool speed $V_{t,x}$ (detail)
13	 <p>Tek <span style="float:right">● Acq Complete M Pos: 0.000s</span> TRIGGER</p> <p>Tipo <b>Fronte</b></p> <p>Sorgente <b>CH1</b></p> <p>Pendenza <b>Discesa</b></p> <p>Modalità <b>Normale</b></p> <p>Accopp. <b>Filtro rumore</b></p> <p>CH1 50.0mV CH2 50.0mV M 100.μs CH3 110mV</p> <p>22-Nov.-11 12:20 &lt;10Hz</p>	 <p>angular position (°)</p> <p>time (s)</p>	 <p>horizontal tool speed (m/min)</p> <p>time (s)</p>
14	 <p>Tek <span style="float:right">● Acq Complete M Pos: 0.000s</span> TRIGGER</p> <p>Tipo <b>Fronte</b></p> <p>Sorgente <b>CH1</b></p> <p>Pendenza <b>Discesa</b></p> <p>Modalità <b>Normale</b></p> <p>Accopp. <b>Filtro rumore</b></p> <p>CH1 50.0mV CH2 50.0mV M 100.μs CH3 110mV</p> <p>22-Nov.-11 12:24 &lt;10Hz</p>	 <p>angular position (°)</p> <p>time (s)</p>	 <p>horizontal tool speed (m/min)</p> <p>time (s)</p>

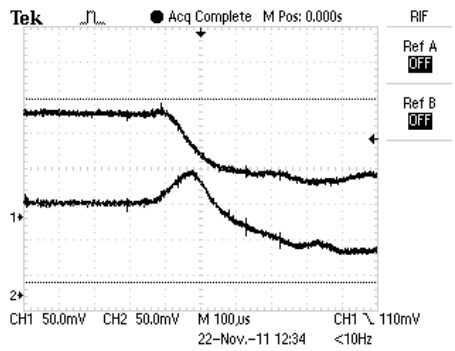
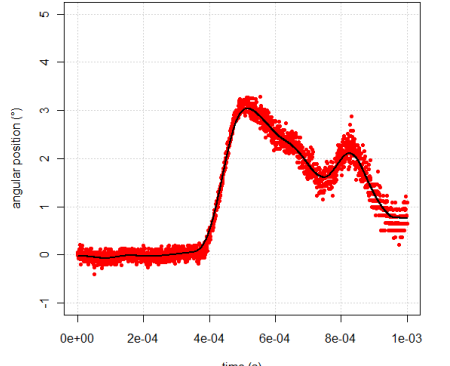
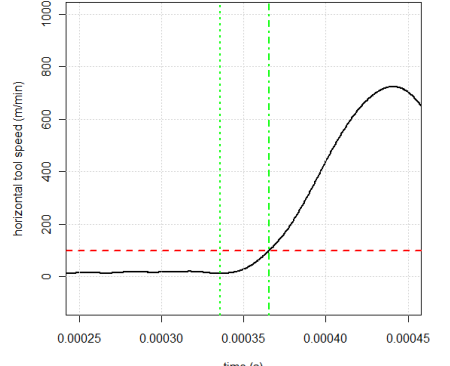
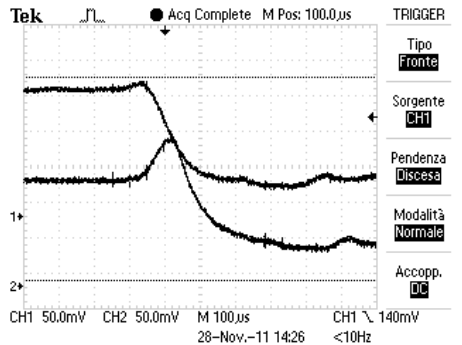
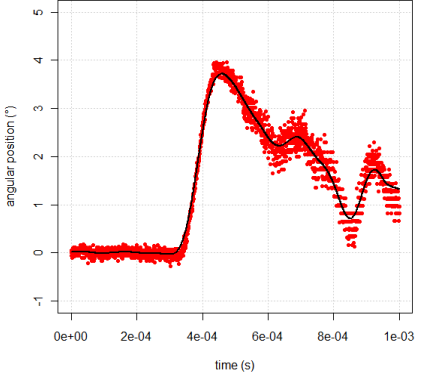
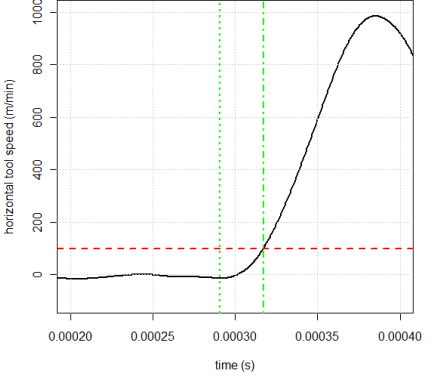
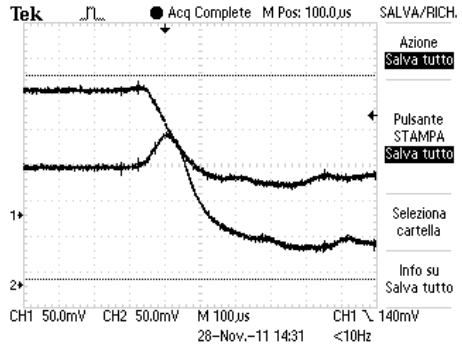
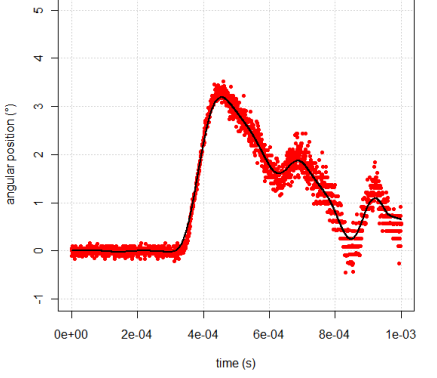
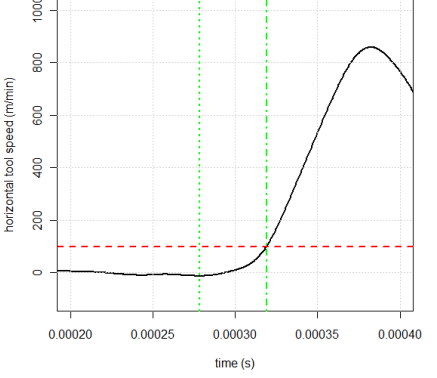
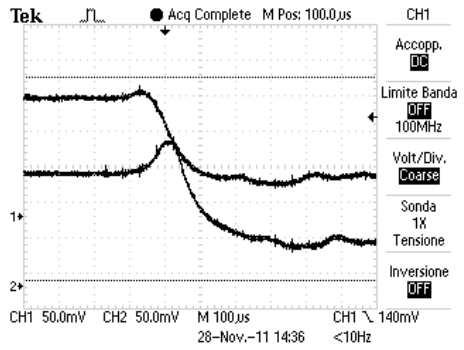
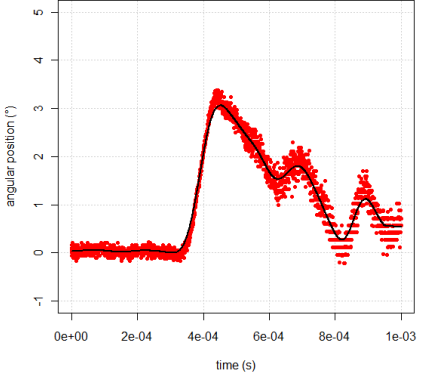
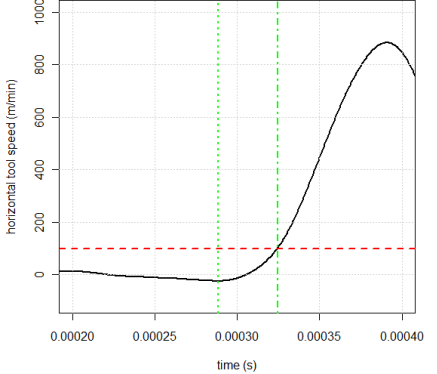
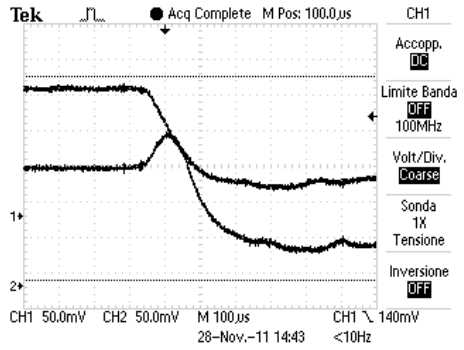
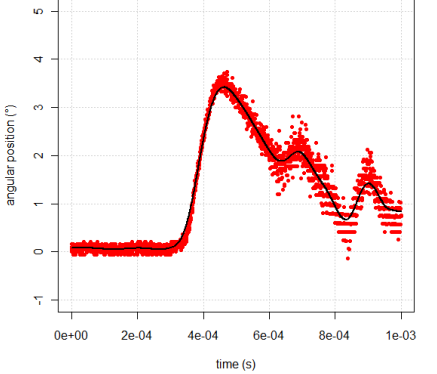
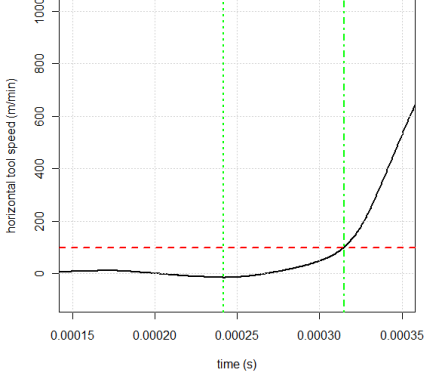
run order	oscilloscope acquisition	angular position	horizontal tool speed $V_{t,x}$ (detail)
15	 <p>Tek <span style="float: right;">● Acq Complete M Pos: 0.000s</span></p> <p>RIF Ref A OFF Ref B OFF</p> <p>1→ 2→</p> <p>CH1 50.0mV CH2 50.0mV M 100us CH1 110mV 22-Nov.-11 12:34 &lt;10Hz</p>	 <p>angular position (°)</p> <p>time (s)</p>	 <p>horizontal tool speed (m/min)</p> <p>time (s)</p>

Table F.2. Acquisitions made by the laser triangulation sensor during the campaign with  $P_{air} = 0.3\text{MPa}$  and their analysis.

run order	oscilloscope acquisition	angular position	horizontal tool speed $V_{t,x}$ (detail)
1	<p>Tek Acq Complete M Pos: 100.0<math>\mu</math>s TRIGGER          Tipo Fronte          Sorgente CH1          Pendenza Discesa          Modalità Normale          Accopp. DC          CH1 50.0mV CH2 50.0mV M 100.0<math>\mu</math>s CH1 140mV          28-Nov.-11 14:01 &lt;10Hz</p>	<p>angular position (°)          time (s)</p>	<p>horizontal tool speed (m/min)          time (s)</p>
2	<p>Tek Acq Complete M Pos: 100.0<math>\mu</math>s TRIGGER          Tipo Fronte          Sorgente CH1          Pendenza Discesa          Modalità Normale          Accopp. DC          CH1 50.0mV CH2 50.0mV M 100.0<math>\mu</math>s CH1 140mV          28-Nov.-11 14:07 &lt;10Hz</p>	<p>angular position (°)          time (s)</p>	<p>horizontal tool speed (m/min)          time (s)</p>

run order	oscilloscope acquisition	angular position	horizontal tool speed $V_{t,x}$ (detail)
3			
4			

run order	oscilloscope acquisition	angular position	horizontal tool speed $V_{t,x}$ (detail)
5	 <p>Tek <span style="float: right;">● Acq Complete M Pos: 100.0us</span> TRIGGER</p> <p>Tipo <b>Fronte</b></p> <p>Sorgente <b>CH1</b></p> <p>Pendenza <b>Discesa</b></p> <p>Modalità <b>Normale</b></p> <p>Accopp. <b>DC</b></p> <p>CH1 50.0mV CH2 50.0mV M 100.us CH3 140mV 28-Nov.-11 14:26 &lt;10Hz</p>	 <p>angular position (°)</p> <p>time (s)</p>	 <p>horizontal tool speed (m/min)</p> <p>time (s)</p>
6	 <p>Tek <span style="float: right;">● Acq Complete M Pos: 100.0us</span> SALVA/RICH.</p> <p>Azione <b>Salva tutto</b></p> <p>Pulsante <b>STAMPA</b></p> <p><b>Salva tutto</b></p> <p>Selezione cartella</p> <p>Info su Salva tutto</p> <p>CH1 50.0mV CH2 50.0mV M 100.us CH3 140mV 28-Nov.-11 14:31 &lt;10Hz</p>	 <p>angular position (°)</p> <p>time (s)</p>	 <p>horizontal tool speed (m/min)</p> <p>time (s)</p>

run order	oscilloscope acquisition	angular position	horizontal tool speed $V_{t,x}$ (detail)
7			
8			

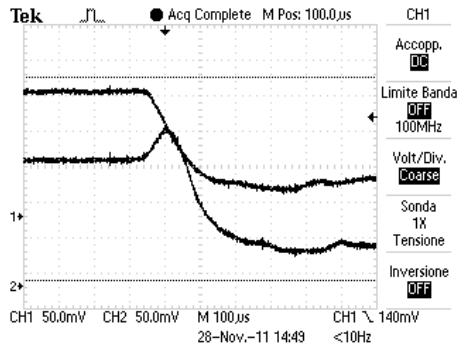
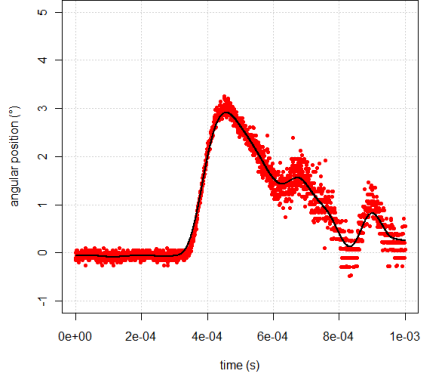
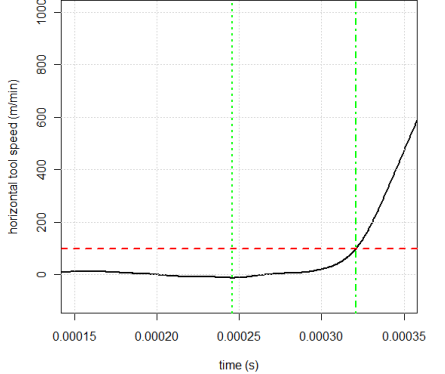
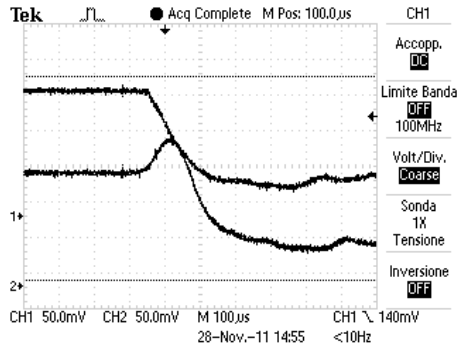
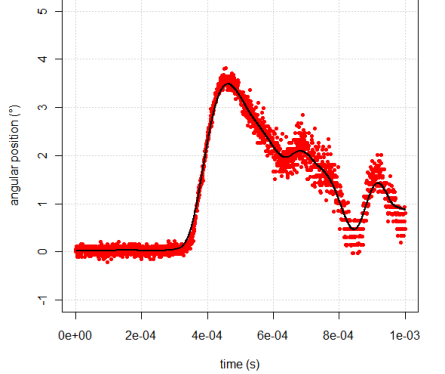
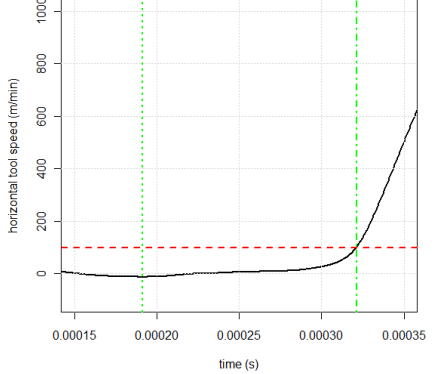
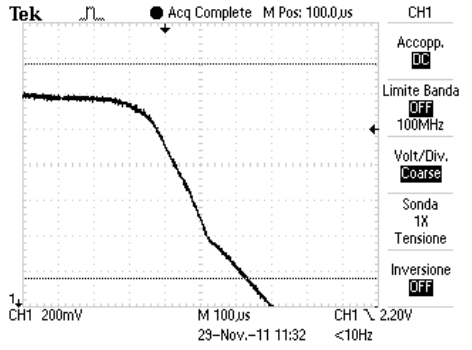
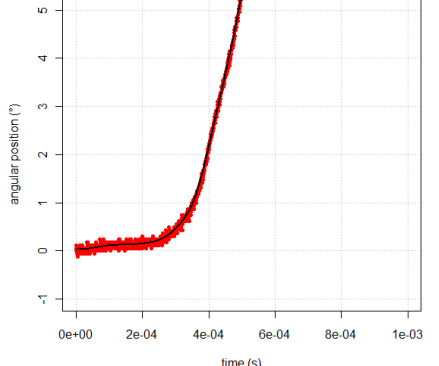
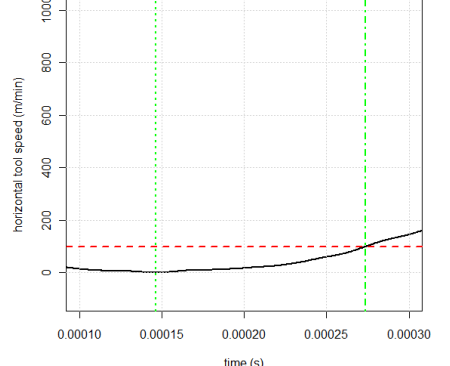
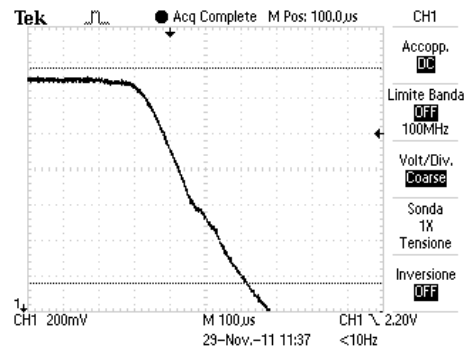
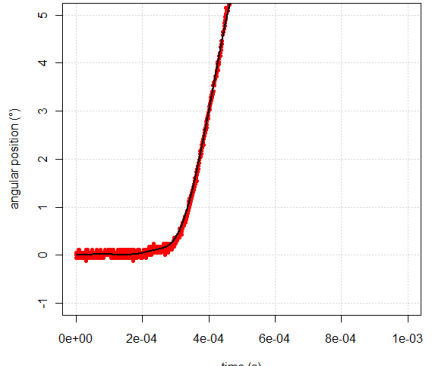
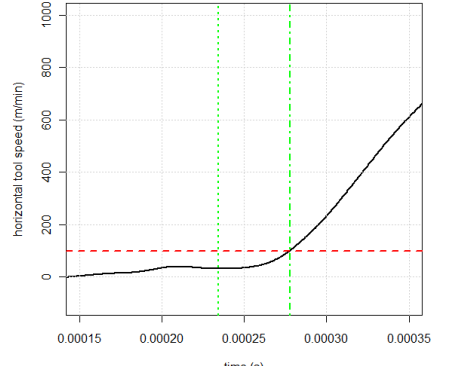
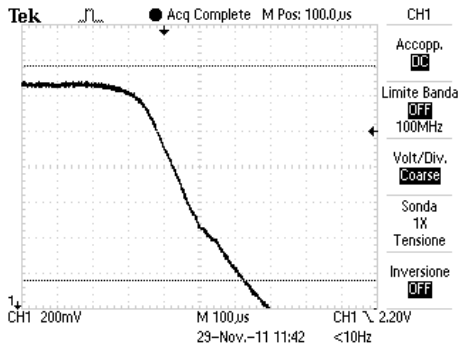
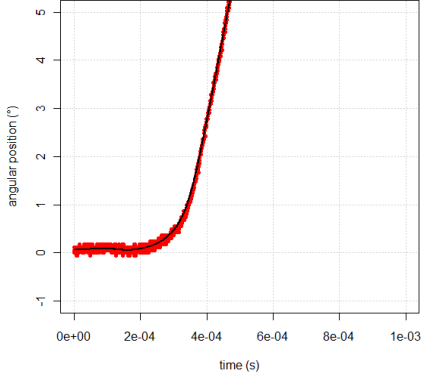
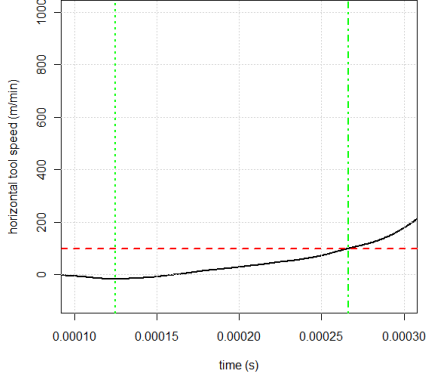
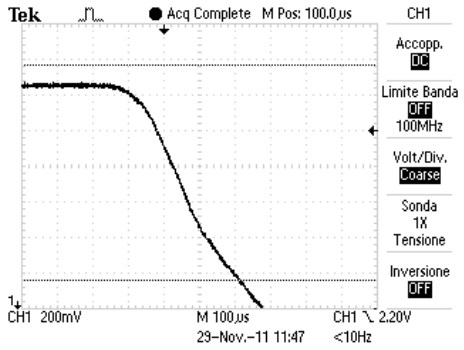
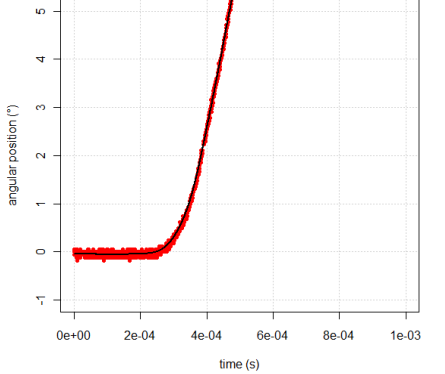
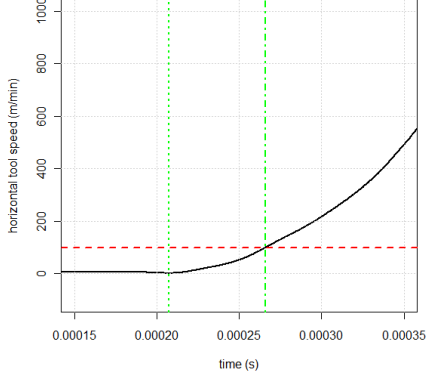
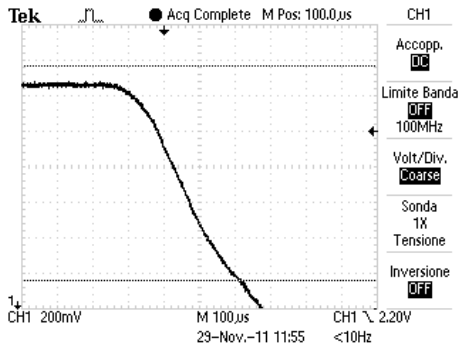
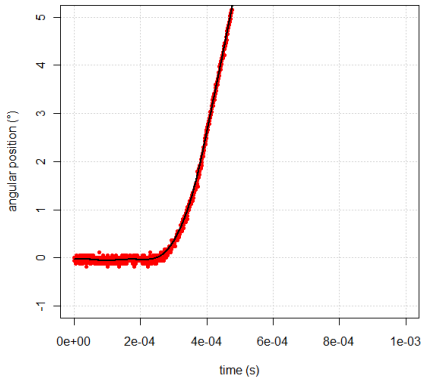
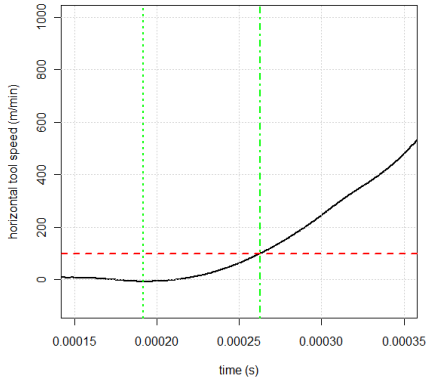
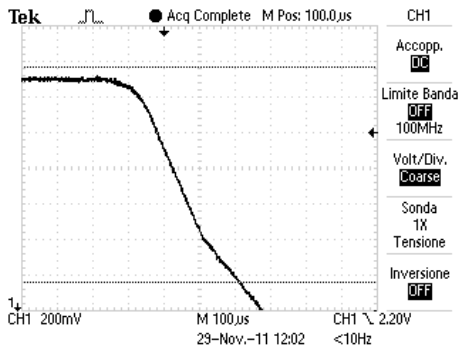
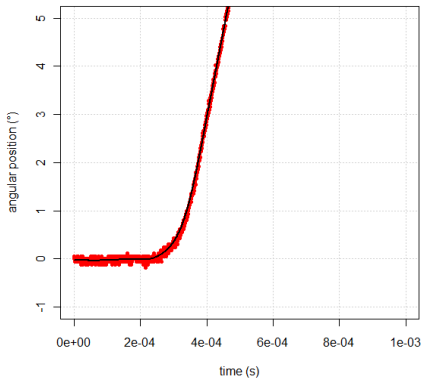
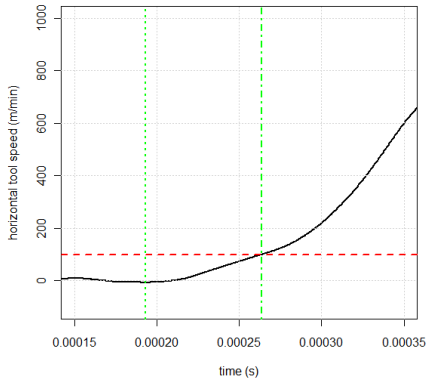
run order	oscilloscope acquisition	angular position	horizontal tool speed $V_{t,x}$ (detail)
9	 <p>Tek <span style="float:right">● Acq Complete M Pos: 100.0<math>\mu</math>s</span></p> <p>CH1 Accopp. <b>DC</b> Limite Banda <b>OFF</b> 100MHz Volt/Div. <b>Coarse</b> Sonda 1X Tensione Inversione <b>OFF</b></p> <p>CH1 50.0mV CH2 50.0mV M 100<math>\mu</math>s CH1 140mV 28-Nov.-11 14:43 &lt;10Hz</p>	 <p>angular position (°)</p> <p>time (s)</p>	 <p>horizontal tool speed (m/min)</p> <p>time (s)</p>
10	 <p>Tek <span style="float:right">● Acq Complete M Pos: 100.0<math>\mu</math>s</span></p> <p>CH1 Accopp. <b>DC</b> Limite Banda <b>OFF</b> 100MHz Volt/Div. <b>Coarse</b> Sonda 1X Tensione Inversione <b>OFF</b></p> <p>CH1 50.0mV CH2 50.0mV M 100<math>\mu</math>s CH1 140mV 28-Nov.-11 14:55 &lt;10Hz</p>	 <p>angular position (°)</p> <p>time (s)</p>	 <p>horizontal tool speed (m/min)</p> <p>time (s)</p>

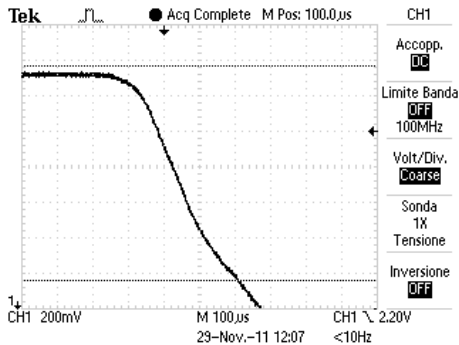
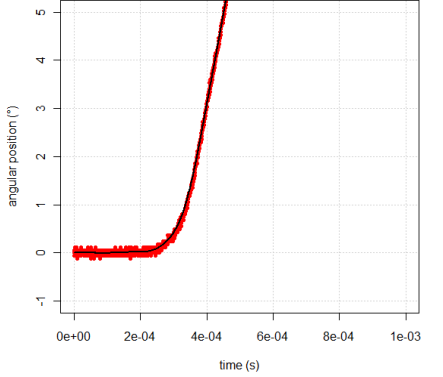
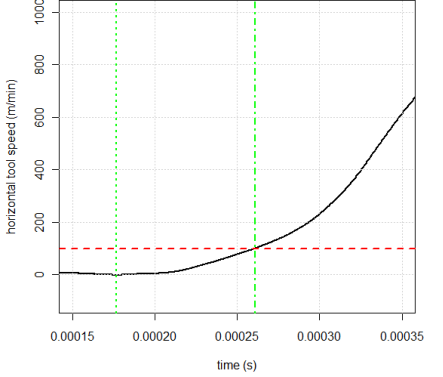
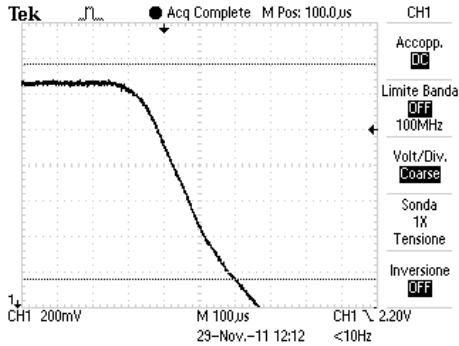
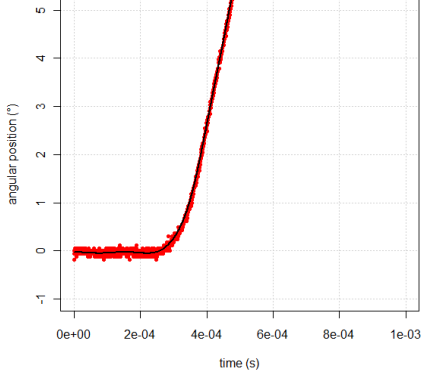
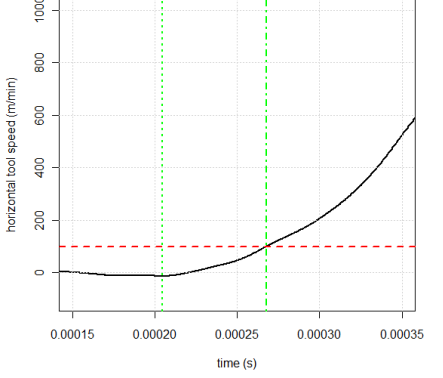


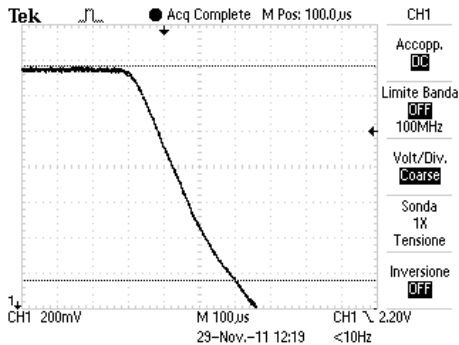
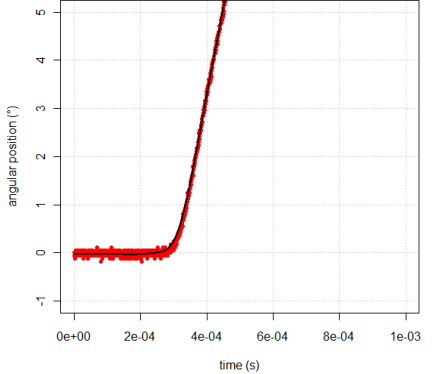
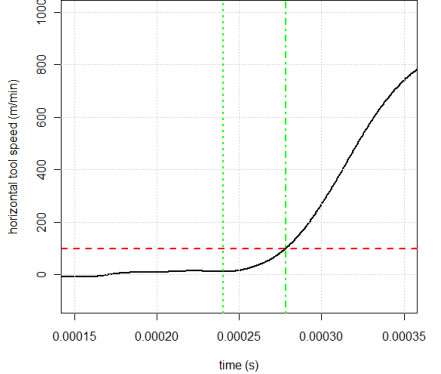
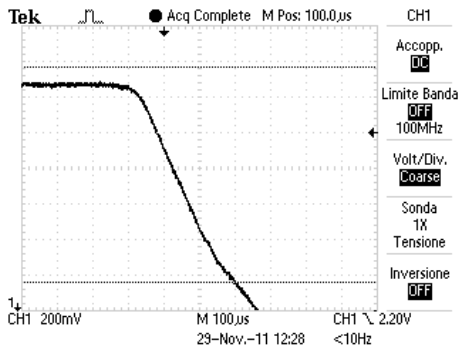
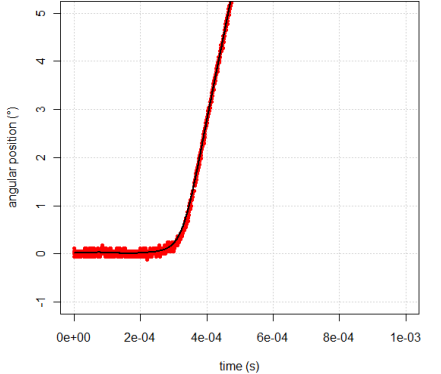
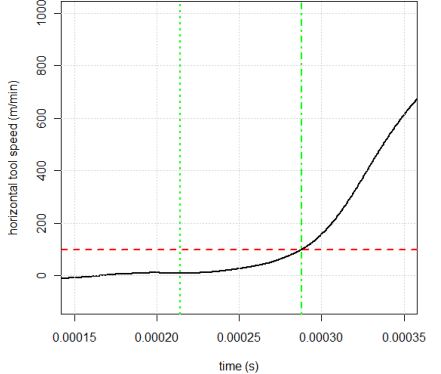
Table F.3. Acquisitions made by the sensor based on polarizing filters during the campaign with  $P_{\text{air}} = 0.2 \text{ MPa}$  and their analysis.

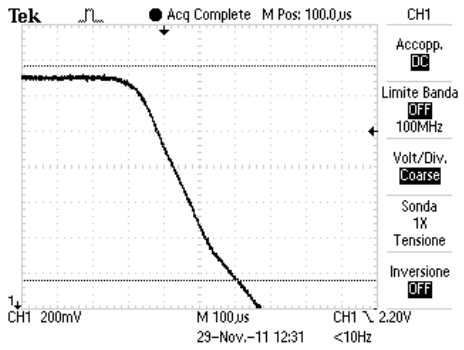
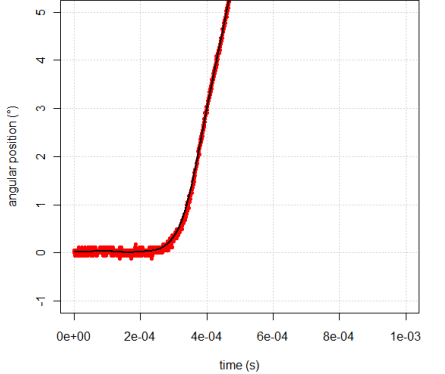
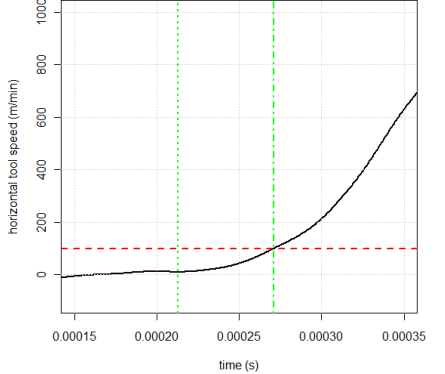
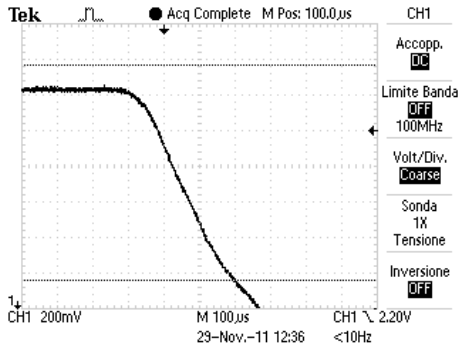
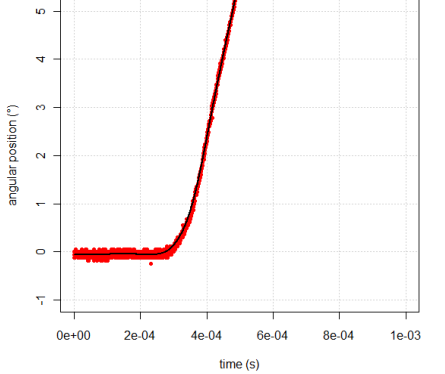
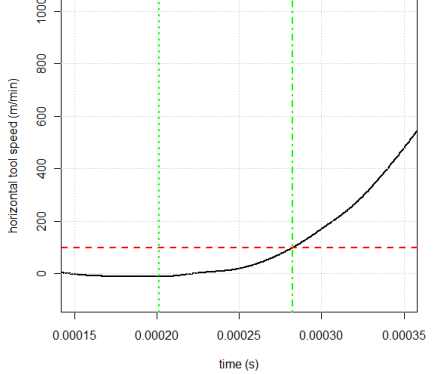
run order	oscilloscope acquisition	angular position	horizontal tool speed $V_{t,x}$ (detail)
1			
2			

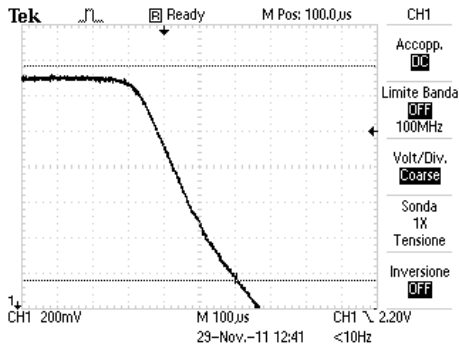
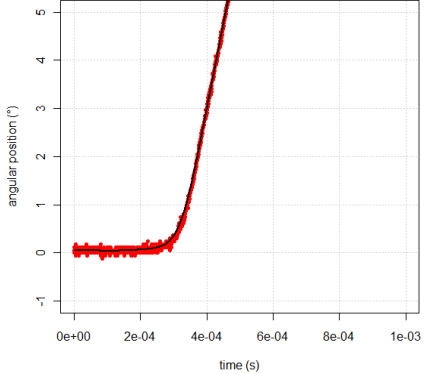
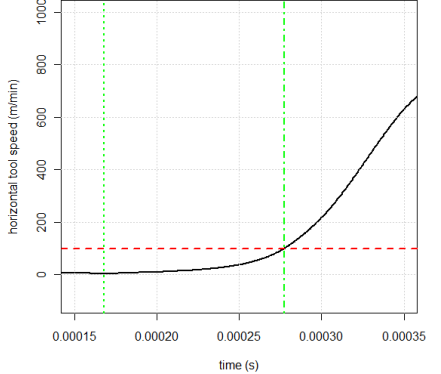
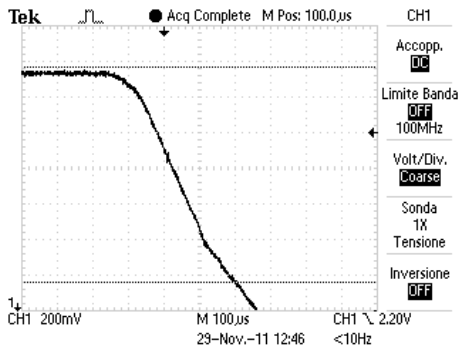
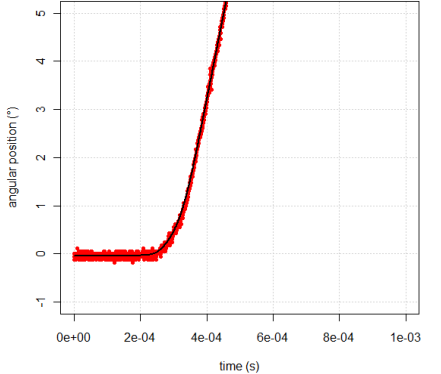
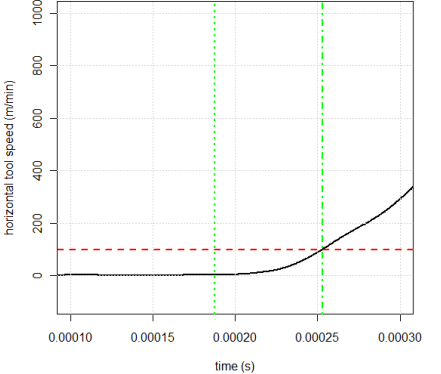
run order	oscilloscope acquisition	angular position	horizontal tool speed $V_{t,x}$ (detail)
3	 <p>Tek <span style="float:right">● Acq Complete M Pos: 100.0us</span> CH1    Accopp. <b>DC</b>    Limite Banda <b>OFF</b> 100MHz    Volt/Div. <b>Coarse</b>    Sonda 1X Tensione    Inversione <b>OFF</b>    1 CH1 200mV M 100us CH1 2.20V &lt;10Hz    23-Nov.-11 11:42</p>	 <p>angular position (°)    time (s)</p>	 <p>horizontal tool speed (m/min)    time (s)</p>
4	 <p>Tek <span style="float:right">● Acq Complete M Pos: 100.0us</span> CH1    Accopp. <b>DC</b>    Limite Banda <b>OFF</b> 100MHz    Volt/Div. <b>Coarse</b>    Sonda 1X Tensione    Inversione <b>OFF</b>    1 CH1 200mV M 100us CH1 2.20V &lt;10Hz    29-Nov.-11 11:47</p>	 <p>angular position (°)    time (s)</p>	 <p>horizontal tool speed (m/min)    time (s)</p>

run order	oscilloscope acquisition	angular position	horizontal tool speed $V_{t,x}$ (detail)
5	 <p>Tek <span style="float: right;">● Acq Complete M Pos: 100.0us</span></p> <p>CH1</p> <p>Accopp. <b>DC</b></p> <p>Limite Banda <b>OFF</b> 100MHz</p> <p>Volt/Div. <b>Coarse</b></p> <p>Sonda 1X Tensione</p> <p>Inversione <b>OFF</b></p> <p>1 CH1 200mV M 100us CH1 2.20V &lt;10Hz</p> <p>23-Nov.-11 11:55</p>	 <p>angular position (°)</p> <p>time (s)</p>	 <p>horizontal tool speed (m/min)</p> <p>time (s)</p>
6	 <p>Tek <span style="float: right;">● Acq Complete M Pos: 100.0us</span></p> <p>CH1</p> <p>Accopp. <b>DC</b></p> <p>Limite Banda <b>OFF</b> 100MHz</p> <p>Volt/Div. <b>Coarse</b></p> <p>Sonda 1X Tensione</p> <p>Inversione <b>OFF</b></p> <p>1 CH1 200mV M 100us CH1 2.20V &lt;10Hz</p> <p>29-Nov.-11 12:02</p>	 <p>angular position (°)</p> <p>time (s)</p>	 <p>horizontal tool speed (m/min)</p> <p>time (s)</p>

run order	oscilloscope acquisition	angular position	horizontal tool speed $V_{t,x}$ (detail)
7	 <p>Tek <span style="float: right;">● Acq Complete M Pos: 100.0us</span></p> <p>CH1</p> <p>Accopp. <b>DC</b></p> <p>Limite Banda <b>OFF</b> 100MHz</p> <p>Volt/Div. <b>Coarse</b></p> <p>Sonda 1X Tensione</p> <p>Inversione <b>OFF</b></p> <p>1 CH1 200mV M 100us CH1 2.20V &lt;10Hz</p> <p>23-Nov.-11 12:07</p>	 <p>angular position (°)</p> <p>time (s)</p>	 <p>horizontal tool speed (m/min)</p> <p>time (s)</p>
8	 <p>Tek <span style="float: right;">● Acq Complete M Pos: 100.0us</span></p> <p>CH1</p> <p>Accopp. <b>DC</b></p> <p>Limite Banda <b>OFF</b> 100MHz</p> <p>Volt/Div. <b>Coarse</b></p> <p>Sonda 1X Tensione</p> <p>Inversione <b>OFF</b></p> <p>1 CH1 200mV M 100us CH1 2.20V &lt;10Hz</p> <p>29-Nov.-11 12:12</p>	 <p>angular position (°)</p> <p>time (s)</p>	 <p>horizontal tool speed (m/min)</p> <p>time (s)</p>

run order	oscilloscope acquisition	angular position	horizontal tool speed $V_{t,x}$ (detail)
9	 <p>Tek Acq Complete M Pos: 100.0<math>\mu</math>s CH1          Accopp. DC          Limite Banda OFF 100MHz          Volt/Div. Coarse          Sonda 1X Tensione          Inversione OFF          CH1 200mV M 100<math>\mu</math>s CH1 2.20V &lt;10Hz          23-Nov.-11 12:13</p>		
10	 <p>Tek Acq Complete M Pos: 100.0<math>\mu</math>s CH1          Accopp. DC          Limite Banda OFF 100MHz          Volt/Div. Coarse          Sonda 1X Tensione          Inversione OFF          CH1 200mV M 100<math>\mu</math>s CH1 2.20V &lt;10Hz          23-Nov.-11 12:28</p>		

run order	oscilloscope acquisition	angular position	horizontal tool speed $V_{t,x}$ (detail)
11			
12			

run order	oscilloscope acquisition	angular position	horizontal tool speed $V_{t,x}$ (detail)
13	 <p>Tek Ready M Pos: 100.0<math>\mu</math>s CH1  Accopp. DC  Limite Banda OFF 100MHz  Volt/Div. Coarse  Sonda 1X Tensione  Inversione OFF  CH1 200mV M 100<math>\mu</math>s CH1 2.20V &lt;10Hz  23-Nov.-11 12:41</p>	 <p>angular position (°)  time (s)</p>	 <p>horizontal tool speed (m/min)  time (s)</p>
14	 <p>Tek Acq Complete M Pos: 100.0<math>\mu</math>s CH1  Accopp. DC  Limite Banda OFF 100MHz  Volt/Div. Coarse  Sonda 1X Tensione  Inversione OFF  CH1 200mV M 100<math>\mu</math>s CH1 2.20V &lt;10Hz  29-Nov.-11 12:46</p>	 <p>angular position (°)  time (s)</p>	 <p>horizontal tool speed (m/min)  time (s)</p>

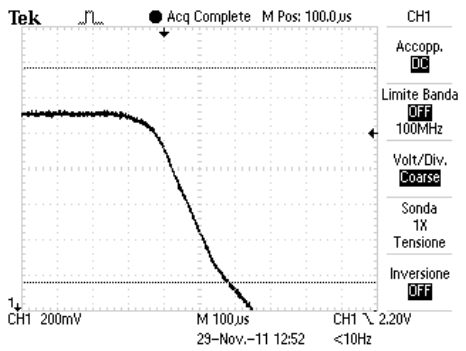
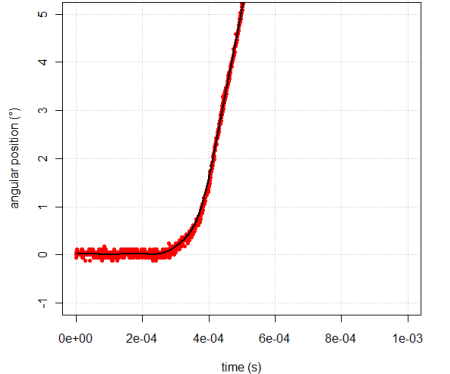
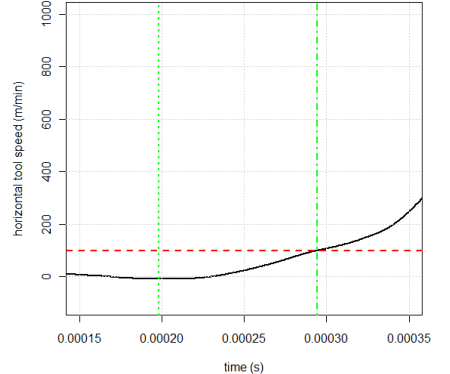
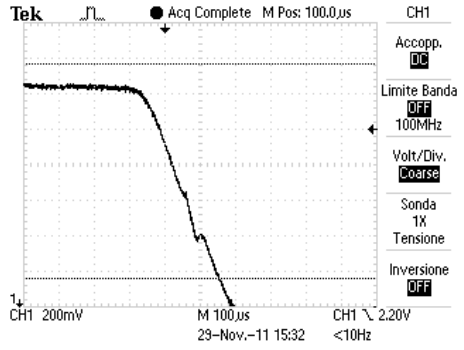
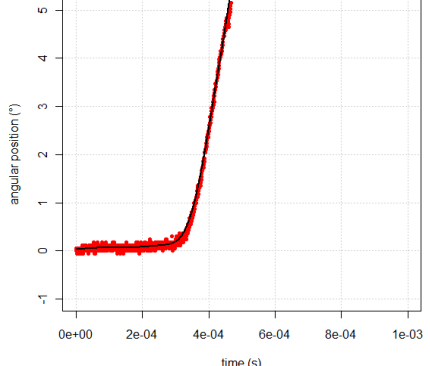
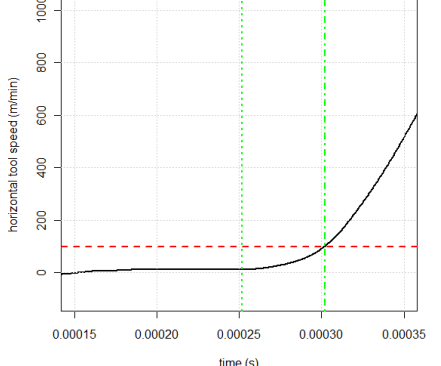
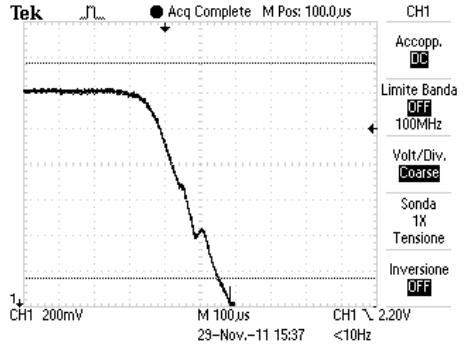
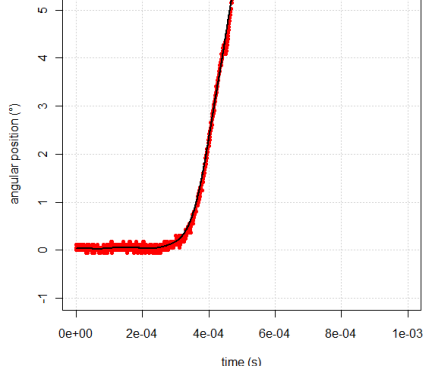
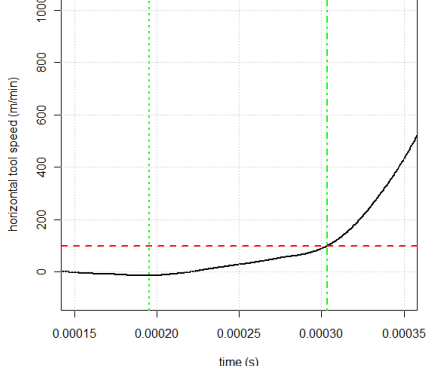
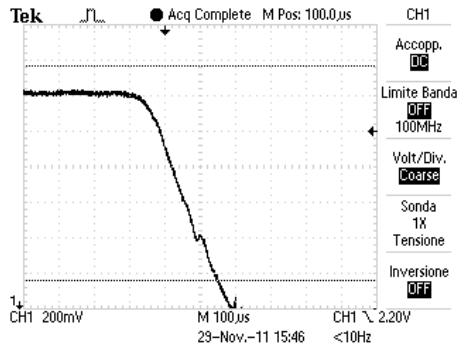
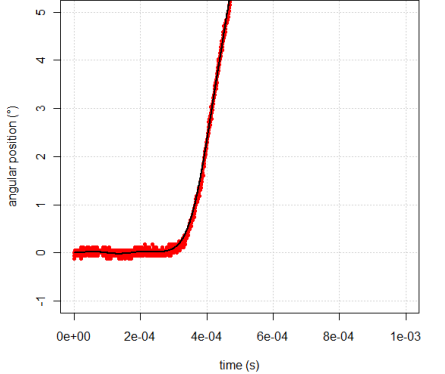
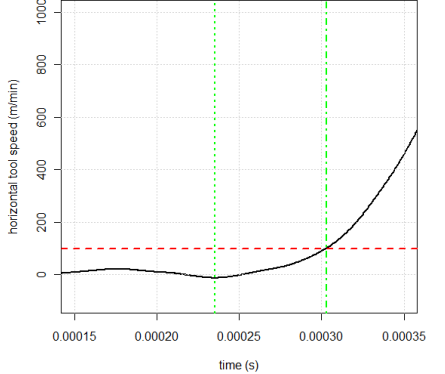
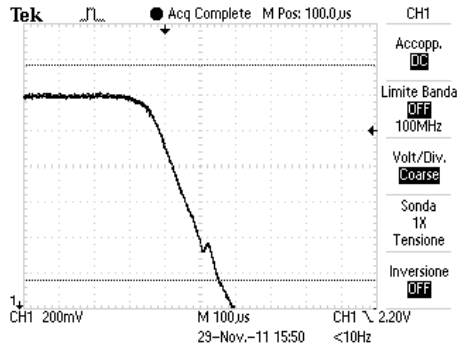
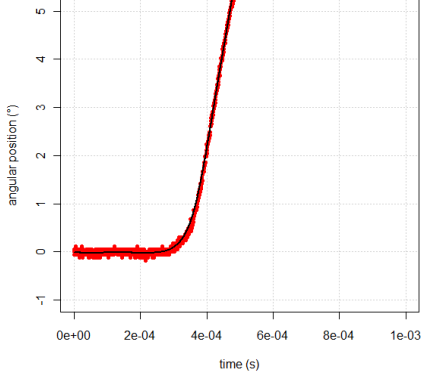
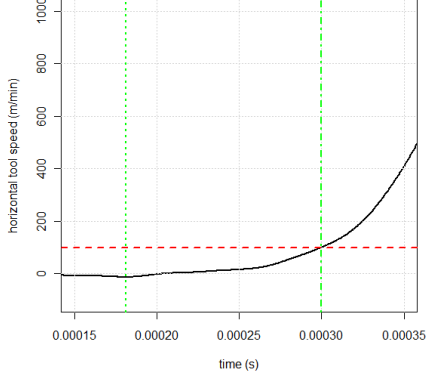
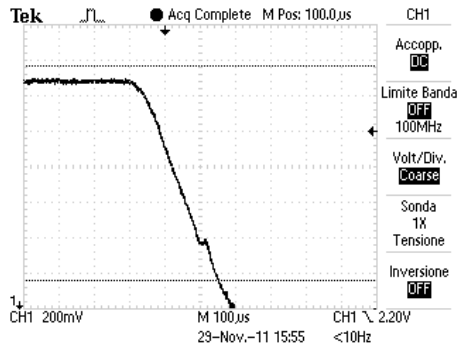
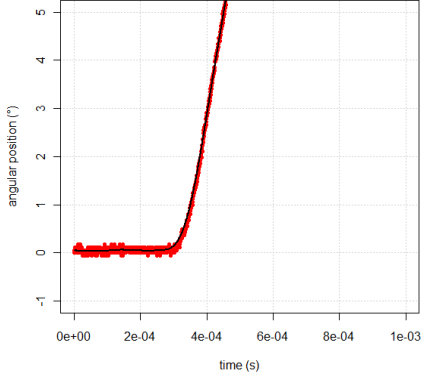
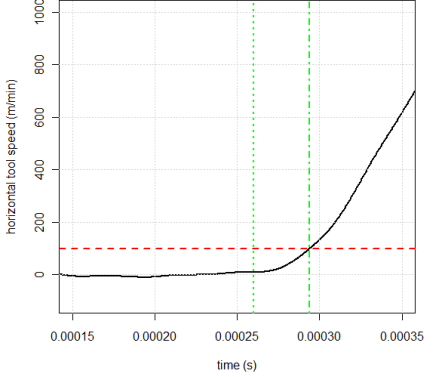
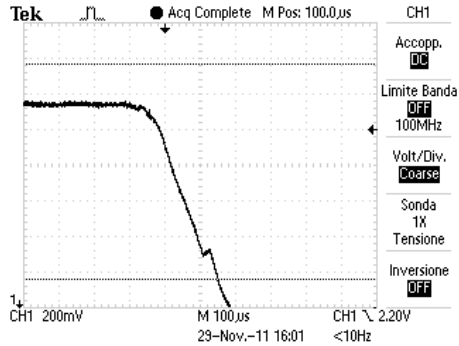
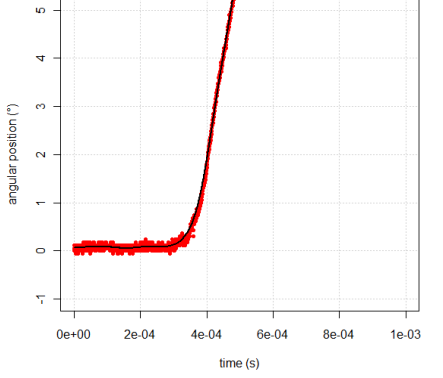
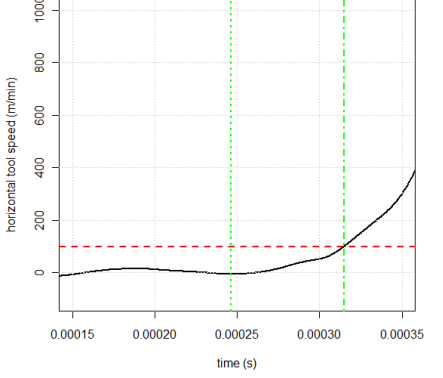
run order	oscilloscope acquisition	angular position	horizontal tool speed $V_{t,x}$ (detail)
15			

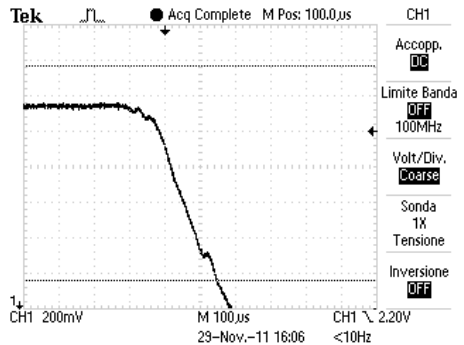
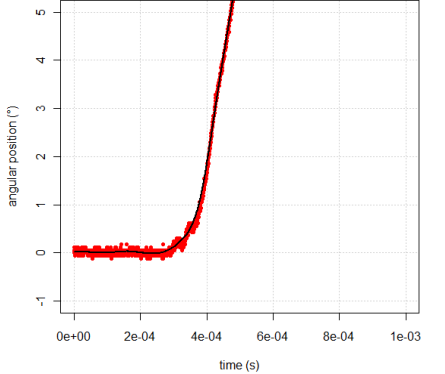
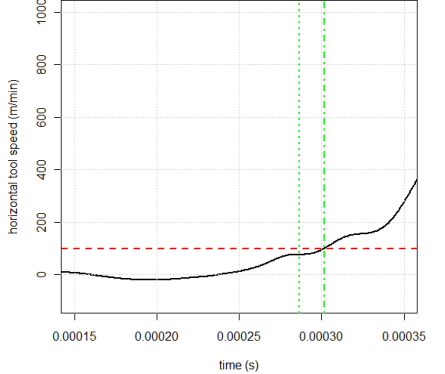
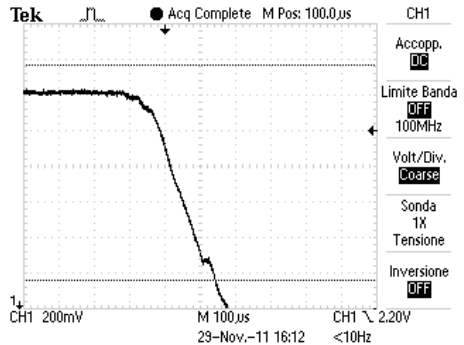
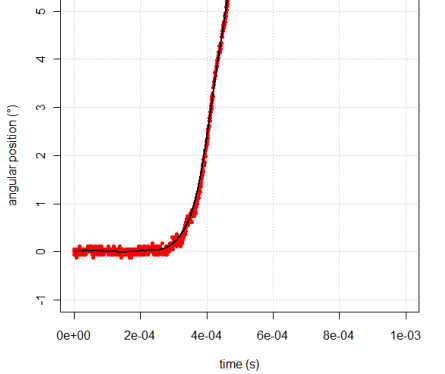
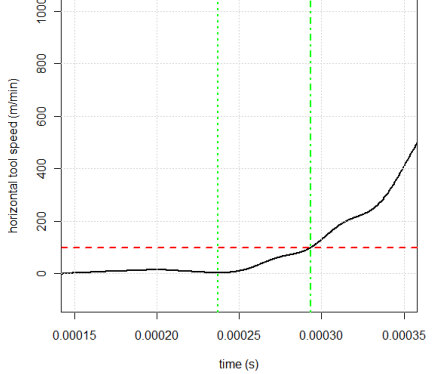


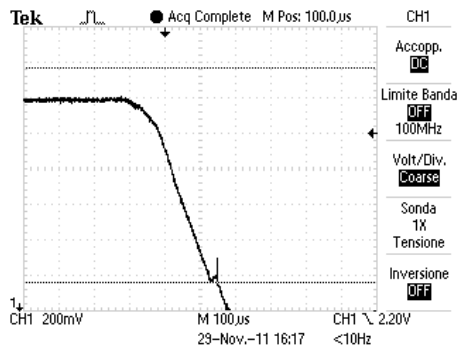
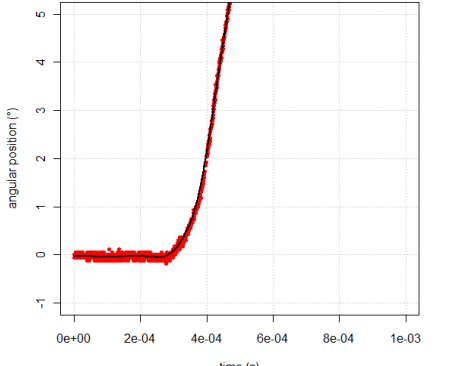
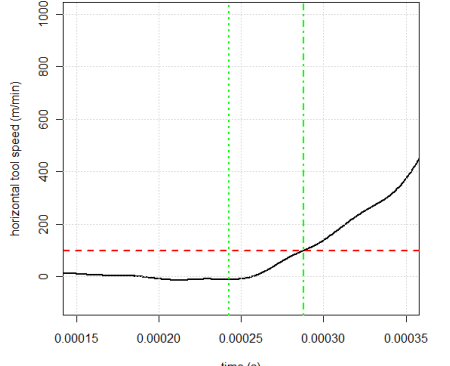
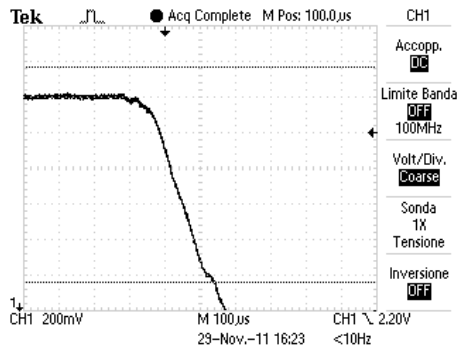
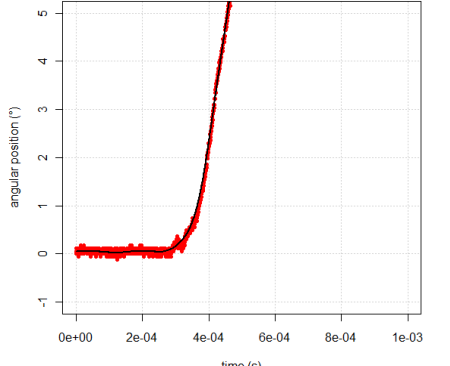
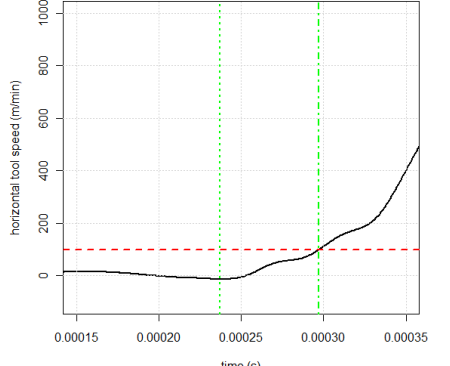
Table F.4. Acquisitions made by the sensor based on polarizing filters during the campaign with  $P_{\text{air}} = 0.3 \text{ MPa}$  and their analysis.

run order	oscilloscope acquisition	angular position	horizontal tool speed $V_{t,x}$ (detail)
1			
2			

run order	oscilloscope acquisition	angular position	horizontal tool speed $V_{t,x}$ (detail)
3			
4			

run order	oscilloscope acquisition	angular position	horizontal tool speed $V_{t,x}$ (detail)
5			
6			

run order	oscilloscope acquisition	angular position	horizontal tool speed $V_{t,x}$ (detail)
7			
8			

run order	oscilloscope acquisition	angular position	horizontal tool speed $V_{t,x}$ (detail)
9	 <p>Tek <span style="float:right">● Acq Complete M Pos: 100.0<math>\mu</math>s</span> CH1  Accopp. <b>DC</b>  Limite Banda <b>OFF</b> 100MHz  Volt/Div. <b>Coarse</b>  Sonda 1X Tensione  Inversione <b>OFF</b>  1<math>\downarrow</math> CH1 200mV M 100<math>\mu</math>s CH1 2.20V  29-Nov.-11 16:17 &lt;10Hz</p>		
10	 <p>Tek <span style="float:right">● Acq Complete M Pos: 100.0<math>\mu</math>s</span> CH1  Accopp. <b>DC</b>  Limite Banda <b>OFF</b> 100MHz  Volt/Div. <b>Coarse</b>  Sonda 1X Tensione  Inversione <b>OFF</b>  1<math>\downarrow</math> CH1 200mV M 100<math>\mu</math>s CH1 2.20V  29-Nov.-11 16:23 &lt;10Hz</p>		



## References

- [1] Masuzawa T. , 2000. State of the art of micromachining, *CIRP Annals - Manufacturing Technology*, vol. 49, pp. 473-488.
- [2] Byrne G. , Dornfeld D. , Denkena B. , 2003. Advancing cutting technology, *CIRP Annals - Manufacturing Technology*, vol. 52, pp. 483-507.
- [3] Liu X., DeVor R.E. , Kapoor S.G. , Ehmann K.F. , 2004. The mechanics of machining at the microscale: assessment of the current state of the science, *Transaction of the ASME - Journal of Manufacturing Science and Engineering*, vol.126, pp. 666-678.
- [4] Dornfeld D. , Min S. , Takeuchi Y. , 2006. Recent Advances in Mechanical Micromachining, *CIRP Annals - Manufacturing Technology*, vol. 55, pp. 745-768.
- [5] Weule H. , Huntrup V. , Tritschle, H. , 2001. Micro-cutting of steel to meet new requirements in miniaturization, *CIRP Annals - Manufacturing Technology*, vol. 49, pp. 61-64.
- [6] Kang I.S. , Kim J.S. , Kim J.H. , Kang M.C. , Seo Y.W. , 2007. A mechanistic model of cutting force in the micro end milling process, *Journal of Materials Processing Technology*, vol. 187-188, pp. 250-255.
- [7] Lucca D.A. , Rhorer R.L. , Komanduri R., 1991. Energy dissipation in the ultraprecision machining of copper, *CIRP Annals - Manufacturing Technology*, vol. 40, pp. 69-72.
- [8] Lucca D.A. , Seo, Y. W. , 1993. Effect of tool edge geometry on energy dissipation in ultraprecision machining, *CIRP Annals - Manufacturing Technology*, vol. 42, pp. 83-86.
- [9] Bissacco G. , Hansen H.N. , Slunsky J. , 2008. Modelling the cutting edge radius size effect for force prediction in micro milling, *CIRP Annals - Manufacturing Technology*, vol. 57, pp. 113-116.
- [10] Lee H.U. , Cho D.W. , Ehmann K.F. , 2008. A mechanistic model of cutting forces in micro-end-milling with cutting-condition-independent cutting force coefficients, *Journal of Manufacturing Science and Engineering - Transaction of the ASME*, vol. 130.
- [11] Dhanorker A. , Özel T. , 2006. An experimental and modeling study on meso/micro end milling process. *ASME International Conference on Manufacturing Science and Engineering 2006*.

- [12] Dhanorker A. , Özel T. , 2008. Meso/micro scale milling for micro-manufacturing', *International Journal of Mechatronics and Manufacturing Systems*, vol. 1, pp. 23-42.
- [13] Ikawa N. , Shimada S. , Tanaka H. , Ohmori G. , 1991. An atomistic analysis of nanometric chip removal as affected by tool-work interaction in diamond turning," *CIRP Annals - Manufacturing Technology*, vol. 40, pp. 551-554.
- [14] Ikawa N. , Donaldson R.R. , Komanduri R. , Koenig W. , Aachen T.H. , McKeown P.A. , Moriwaki T. , Stowers I.F. , 1991. Ultraprecision metal cutting, the past, the present, and the future, *CIRP Annals - Manufacturing Technology*, vol. 40, pp. 587-594.
- [15] Kim C. J. , Bono M. , Ni J., 2002. Experimental analysis of chip formation in micro-milling, *Transaction of NAMRI/SME*, vol. 30, pp. 247-254.
- [16] Kim C.J. , Mayor J.R. , Ni J. , 2004. A static model of chip formation in microscale milling, *Journal of Manufacturing Science and Engineering - Transaction of the ASME*, vol. 126, pp. 710-718.
- [17] Jackson M.J. in Davim J.P. , 2008. *Machining - Fundamentals and recent advances*, Springer.
- [18] Vogler M.P. , DeVor R.E. , Kapoor S.G. , 2003. Microstructure-level force prediction model for micro-milling of multi-phase materials, *Journal of Manufacturing Science and Engineering*, vol. 125, pp. 202-209.
- [19] Vogler M.P. , DeVor R.E. , Kapoor S.G., 2004. On the modeling and analysis of machining performance in micro-endmilling - Part I: surface generation, *Journal of Manufacturing Science and Engineering*, vol. 126, pp. 684-693.
- [20] Lawson B.L. , Kota N. , Ozdoganlar O.B. , 2008. Effects of crystallographic anisotropy on orthogonal micromachining of single-crystal aluminum, *Journal of Manufacturing Science and Engineering*, vol. 130.
- [21] Waldorf D. J. , DeVor R. E. , Kapoor S. G. , 1998. Slip-line field for ploughing during orthogonal cutting, *Transaction of the ASME - Journal of Manufacturing Science and Engineering*, vol. 120, pp. 693-698.
- [22] Waldorf D. J. , DeVor R. E. , Kapoor S. G. , 1999. An evaluation of ploughing models for orthogonal machining, *Transaction of the ASME - Journal of Manufacturing Science and Engineering*, vol. 121, pp. 550-558.
- [23] Kountanya R. K. , Endres W. J. , 2001. A high-magnification experimental study of orthogonal cutting with edge-honed tools, *Proceedings of the ASME Manufacturing Engineering Division of 2001 ASME International Mechanical Engineering Congress and Exposition*, vol. 12, pp. 157-164.



- [24] Annoni M. , Semeraro Q. , 2010. Factors affecting the force variability in micro-end-milling, *4M Conference 2010*.
- [25] Kececioglu, D. , 1958. Shear-strain rate in metal cutting and its effects on shear flow stress, *Transaction of the ASME*, vol. 80, pp. 158-168.
- [26] Hsu T.C. , 1966. A study of the normal and shear stresses on a cutting tool, *Transaction of the ASME - Journal of Engineering for Industry*, vol. 88, pp. 51-64.
- [27] Hastings W.F. , 1967. A new quick-stop device and grid technique for metal cutting research, *Annals of the CIRP*, vol. 15, pp. 109-116.
- [28] Ponshe G.R. , 1967. A new explanation of the phenomenon of chip curling during machining, *Transaction of the ASME - Journal of Engineering for Industry*, vol. 89, pp. 376-379.
- [29] Giusti F. , 1969. Esame comparativo delle apparecchiature per il taglio bruscamente interrotto, *Macchine*, vol. 5, pp. 369-376.
- [30] Ellis J. , Kirk R. , Barrow G. , 1969. The development of a quick-stop device for metal cutting research, *International Journal of Machine Tool Design & Research*, vol. 9, pp. 321-339.
- [31] Williams J.E. , Smart E.F. , Milner D.R. , 1970. The metallurgy of machining, Part I: basic considerations and the cutting of pure metals, *Metallurgia*, vol. 81, pp. 3-10.
- [32] Stevenson M.G. , Oxley P.L.B. , 1970. An experimental investigation of the influence of speed and scale on the strain-rate in a zone of intense plastic deformation, *Proceedings of the Institution of Mechanical Engineers*, vol. 184, pp. 561-576.
- [33] Philip P.K. , 1971. Study of the performance characteristics of an explosive quick-stop device for freezing cutting action, *International Journal of Machine Tool Design & Research*, vol. 11, pp. 133-144.
- [34] Brown R.H. , Komanduri R. , 1973. An investigation of the performance of a quick-stop device for metal cutting studies, *Proceedings of the 13th International Machine Tool Design & Research Conference*, pp 225-231.
- [35] Komanduri R. , Brown R.H. , 1981. On the mechanics of chip segmentation in machining, *Transaction of the ASME - Journal of Engineering for Industry*, vol. 103, pp. 33-51.
- [36] Gladman C.A. , Bramall F.J. , 1967. Contributed discussion to [32].
- [37] Vorm T. , 1976. Development of a quick-stop device and an analysis of the frozen-chip technique, *International Journal of Machine Tool Design & Research*, vol. 16, pp. 241-250.

- [38] Brown R.H. , 1976. A double shear-pin quick-stop device for very rapid disengagement of a cutting tool, *International Journal of Machine Tool Design & Research*, vol. 16, pp. 115-121.
- [39] Black J.T. , James C.R. , 1981. The hammer QSD - quick stop device for high speed machining and rubbing, *Transaction of the ASME - Journal of Engineering for Industry*, vol. 103, pp. 13-21.
- [40] Griffiths B.J. , 1986. The development of a quick-stop device for use in metal cutting hole manufacturing process, *International Journal of Machine Tool Design & Research*, vol. 26, pp. 191-203.
- [41] Giusti F. , von Turkovich B.F. , Tantussi G. , Romoli V. , Fantozzi C. , 1989. A 1000 metri al minuto, *Meccanica oggi*, vol. 1, pp. 60-64.
- [42] Yeo S.H. , Lui W.W. , Phung V. , 1992. A quick-stop device for orthogonal machining, *Journal of Materials Processing Technology*, vol. 29, pp. 41-46.
- [43] Lin J.T. , Bhattacharyya D. , Ferguson W.G. , 1998. Chip formation in the machining of SiC-particle-reinforced aluminium-matrix composites, *Composites Science and Technology*, vol. 58, pp. 285-291.
- [44] Joshi S.S. , Ramakrishnan N. , Ramakrishnan P. , 2001. Micro-structural analysis of chip formation during orthogonal machining of Al/SiCp composites. *Transaction of the ASME - Journal of Manufacturing Science and Engineering*, vol. 123, pp. 315-321.
- [45] Chern G.L. , 2006. Development of a new and simple quick stop device for the study on chip formation, *International Journal of Machine Tools & Manufacture*, vol. 45, pp. 853-859.
- [46] Wu C.L. , Wang K.S. , Tsai L.C. , 2006. A new electromagnetic quick stop device for metal cutting studies, *International Journal of Advanced Manufacturing Technology*, vol. 29, pp. 853-859.
- [47] Subbiah S. , Melkote S.N. , 2007. Evidence of ductile tearing ahead of the cutting tool and modeling the energy consumed in material separation in micro-cutting, *Transaction of the ASME - Journal of Manufacturing Science and Engineering*, vol. 129, pp. 321-331.
- [48] Subbiah S. , Melkote S.N. , 2008. Effect of finite edge radius on ductile fracture ahead of the cutting tool edge in micro-cutting of Al2024-T3, *Materials Science and Engineering A*, vol. 474, 283-300.
- [49] Ghadbeigi H. , Bradbury S.R. , Pinna C., Yates J. R., 2008. Determination of micro-scale plastic strain caused by orthogonal cutting. *International Journal of Machine Tools & Manufacture*, vol. 48, pp. 228-235.

- [50] Zeb M. , Veldhuis S. Irfan M. , 2009. Material response of Ramax-2 during high-speed machining using quick-stop device, *Experimental techniques*, vol. 33, pp. 18-23.
- [51] Datasheet of Kern EVO machining centre  
([http://www.kern-microtechnic.com/upload/media/kern\\_evo\\_e.pdf](http://www.kern-microtechnic.com/upload/media/kern_evo_e.pdf))
- [52] Verein Deutscher Ingenieure / Deutsche Gesellschaft für Qualität VDI/DGQ 3441, Statistical testing of the operational and positional accuracy of machine tools - Basis, 1982
- [53] Datasheet of Blum-Novotest laser presetting system  
([http://www.blum-novotest.de/uploads/media/Nano\\_NT\\_EN\\_01.pdf](http://www.blum-novotest.de/uploads/media/Nano_NT_EN_01.pdf))
- [54] Datasheet of Kistler load cell  
([http://www.kistler.com/mediaaccess/9257BA\\_BP\\_\\_000-150e-06.03.pdf](http://www.kistler.com/mediaaccess/9257BA_BP__000-150e-06.03.pdf))
- [55] Datasheet of Kistler control unit  
([http://www.ni.com/pdf/products/us/4daqsc202-204\\_ETC\\_212-213.pdf](http://www.ni.com/pdf/products/us/4daqsc202-204_ETC_212-213.pdf))
- [56] Datasheet of Kistler PC embedded data acquisition system  
([http://www.ni.com/pdf/products/us/4daqsc212\\_216.pdf](http://www.ni.com/pdf/products/us/4daqsc212_216.pdf))
- [57] Datasheet of Kistler USB data acquisition system  
(<http://sine.ni.com/ds/app/doc/p/id/ds-9/lang/en>)
- [58] Datasheet of Tektronix oscilloscope  
([http://www.tek.com/sites/tek.com/files/media/media/resources/3GW\\_25644\\_1.pdf](http://www.tek.com/sites/tek.com/files/media/media/resources/3GW_25644_1.pdf))
- [59] Annoni M. , Fontanili L. , Grossi E. , Rebaioli L. , Semeraro Q. , 2011. Design and characterization of a micro Quick-Stop Device, *10<sup>th</sup> AITeM Conference*.
- [60] Annoni M. , Fontanili L. , Grossi E. , Rebaioli L. , Semeraro Q. , 2011. A new micro quick-stop device for orthogonal microcutting, *4M Conference 2011*.
- [61] Annoni M. , Rebaioli L. , Semeraro Q. , 2011. Performance validation of a micro quick-stop device, Submitted for *NAMRC40 Conference*.
- [62] Fontanili L. , 2010. Sviluppo di un micro quick-stop device, Master thesis, Politecnico di Milano.
- [63] Datasheet of solenoid  
([http://www.aerco.co.uk/images/sub\\_sub\\_categories/series43.pdf](http://www.aerco.co.uk/images/sub_sub_categories/series43.pdf))
- [64] Goldsmith W. , 2002. Impact: the theory and physical behaviour of colliding solid, Dover Edition.
- [65] Datasheet of Phantom v5.1 high speed camera  
([http://www.visionresearch.com/uploads/docs/Discontinued/V5/DS\\_v51.pdf](http://www.visionresearch.com/uploads/docs/Discontinued/V5/DS_v51.pdf))

- [66] Cleveland W.S. , 1979. Robust locally weighted regression and smoothing scatterplots, *Journal of the American Statistical Association*, vol. 74, pp. 829-836.
- [67] Cleveland W.S. , Devlin J.S. , 1988. Locally weighted regression: an approach to regression analysis by local fitting, *Journal of the American Statistical Association*, vol. 83, pp. 596-610.
- [68] Cleveland W.S. , Loader C. , 1996. Smoothing by local regression: principles and methods, AT&T Bell Laboratories (<http://cm.bell-labs.com/cm/ms/departments/sia/doc/smoothing.springer.pdf>)
- [69] Loader C. , 1999. Local regression and likelihood, Springer.
- [70] "Locfit" package help  
(<http://cran.r-project.org/web/packages/locfit/locfit.pdf>)
- [71] Fornberg B. , 1988. Generation of finite differences formulas on arbitrarily spaced grids, *Mathematics of computation*, vol. 51, pp. 699-706.
- [72] International Organization for Standardization ISO 6507-1, Metallic materials - Vickers hardness test - Part 1: Test method, 2005
- [73] Datasheet of Mitutoyo profilometer  
[http://www.mitutoyo.com.sg/documents/CV-3100\\_4100.pdf](http://www.mitutoyo.com.sg/documents/CV-3100_4100.pdf)
- [74] Datasheet of Alicona Infinite Focus  
<http://www.alicon.com/home/products/InfiniteFocus/InfiniteFocus-Standard.en.php>
- [75] SANDVIK COROMANT Technical guide  
([http://www2.coromant.sandvik.com/coromant/downloads/tech\\_guide/ENG/MTG\\_A.PDF](http://www2.coromant.sandvik.com/coromant/downloads/tech_guide/ENG/MTG_A.PDF))
- [76] SANDVIK COROMANT Turning tools Catalogue  
([http://www2.coromant.sandvik.com/coromant/downloads/catalogue/ENG/TUR\\_A.pdf](http://www2.coromant.sandvik.com/coromant/downloads/catalogue/ENG/TUR_A.pdf))

(all website links have been last visited on January 30th, 2011)